The Dissertation Committee for Justin Thomas Blair certifies that this is the approved version of the following dissertation:

Investigating the Origin of Strangeness Enhancement Using Jet-Like $h - \phi$ Angular Correlations in p-Pb Collisions with ALICE

Committee:

Christina Markert, Supervisor

Irene Gamba

Sonia Paban

Peter Onyisi

Investigating the Origin of Strangeness Enhancement Using Jet-Like $h-\phi$ Angular Correlations in p-Pb Collisions with ALICE

by

Justin Thomas Blair

Dissertation

Presented to the Faculty of the Graduate School of

The University of Texas at Austin

in Partial Fulfillment

of the Requirements

for the degree of

Doctor of Philosophy

The University of Texas at Austin

May, 2023

To Emily.

Acknowledgments

There are a number of people I must thank, without whom I would not have been able to complete this dissertation. To the entire Relativistic Heavy-Ion group at UT, all of whom were vital for my studies, for their expertise and guidance through this long process. To my advisor, Prof. Christina Markert, who was there to help guide me through my research and through the intricacies of working within a large, international collaboration. To Dr. Deepa Thomas, who was somehow an always willing and cheerful recipient for any questions I had, from coding problems and theory calculations to life and career advice. To my co-students and co-researchers Alex, Erin, Prahbat, and Ryan, whose camaraderie helped make even the difficult days fun. To Lanny, whose extensive knowledge was integral in helping me put all the different aspects of our field into a coherent picture. To Prof. Jerry Hoffman, who I'm happy I was able to know, even briefly, and who helped welcome me into the group.

To my family, especially my parents, who have been endlessly supportive and have always encouraged me to pursue my passions. To Emily, whose support during the long journey represented by this dissertation was incalculable and invaluable. Without the strong support from my friends and family, reaching this endpoint would not have been possible.

Investigating the Origin of Strangeness Enhancement Using Jet-Like $h-\phi$ Angular Correlations in p-Pb Collisions with ALICE

Publication No. _____

Justin Thomas Blair, Ph.D.

The University of Texas at Austin, 2023

Supervisor: Christina Markert

The strong nuclear force that is responsible for binding together protons and neutrons within atomic nuclei - and responsible for forming the nucleons themselves - can be explained by a quantum field theory known as Quantum Chromodynamics (QCD). At extreme temperatures and pressures, QCD predicts the formation of a new state of nuclear matter called the Quark Gluon Plasma (QGP). The behavior of QCD interactions under these extreme conditions can be studied in the laboratory by colliding together ultra-relativistic heavy-ions, where the energy density is expected to reach well above the critical transition temperature for QGP formation. Heavy-ion collisions have been studied for decades at multiple different particle accelerator facilities, including the Large Hadron Collider (LHC). At the LHC, the primary experiment focused on studying these heavy-ion collisions is known as A Large Ion Collider Experiment (ALICE). ALICE is designed to study high multiplicity heavy-ion collisions, as well as proton-proton and proton-ion collisions that can be used as baseline measurements.

Among the expected signatures of QGP formation is an increase in the production

of strange quarks within the medium, a phenomenon known as strangeness enhancement. Strangeness enhancement can be studied by measuring the production ratio of strange particles to non-strange particles. While first predicted, and later observed, to be present in heavy-ion collisions, more recent measurements have observed an onset of strangeness enhancement occurring in smaller systems, such as p-Pb collisions. The enhancement seen in heavy-ion collisions can be fairly well described using a statistical hadron production model, where the temperature is high enough that the strange quark is in full equilibrium with the two other light flavor quarks. However, the microscopic behavior underlying this enhancement in smaller systems is still not completely understood. Further differentiation of strange particle production is needed to pinpoint the partonic interactions, particularly in the soft-scattering sector, responsible for strangeness enhancement.

In this analysis, angular correlations between a high momentum hadron and a $\phi(1020)$ meson (comprised of a strange quark-antiquark pair) are measured within p-Pb collisions with ALICE at the LHC. With the high momentum trigger hadron acting as a proxy for a high energy jet of particles, and the $\phi(1020)$ meson acting as a strangeness probe, these correlations can be used to separate out the production of $\phi(1020)$ mesons within jets (closely aligned to the direction of the trigger) from production in the non-jet underlying event (uncorrelated with the direction of the trigger). These differential yield measurements are a way to separate out hard-scattering production (more jet-like) from soft-scattering production (more medium-like). The $\phi(1020)$ correlations can be directly compared with inclusive dihadron correlations to calculate the strange to non-strange production ratio (i.e ϕ/h).

With this technique, strangeness production within jets and the underlying events are measured as a function of multiplicity and are compared between a lower and

higher momentum region. These different production regimes show a clear ordering, with ϕ/h production in the underlying event significantly higher than in jets for all multiplicities. The evolution of the per-trigger yields within the near-side (jet) and away-side (modified jet) as a function of multiplicity are studied separately, and differences in behavior suggest a change to the away-side production at lower momentum. This technique for measuring yield ratios is then discussed as a way to further constrain the origin of strangeness enhancement in small systems.

Contents

List of Tables

List of Figures

Chapter One: Introduction

This first chapter will give a brief historical and theoretical introduction to the field of relativistic heavy-ion physics, including useful coordinate variables and observables. It will also discuss the experimental signatures of a novel state of nuclear matter created within heavy-ion collisions, known as the Quark-Gluon Plasma. Chapter two will then discuss the technical details of the ALICE detector, including details on the relevant subsystems. After the introduction to the necessary physics and equipment is complete, chapter three will give the exact measurement foundation and procedure for this thesis' central analysis, followed by a chapter expanding on the analysis' technical details. Following the analysis details is a chapter discussing the possible sources of uncertainty, as well as additional studies on potential systematic biases of the measurement procedure. Finally, the last chapters will present the central results and discussion, followed by a brief summary.

1.1 A Brief History of Quarks

In the mid-20th Century, experiments around the world were producing a veritable zoo of new particles. Among the first discovered was the pion. Theoretically proposed as a force mediator for the strong nuclear force between nucleons, the pion was first seen experimentally in 1947[1]. Using a cloud chamber to photograph the ionization paths of high energy cosmic rays interacting with gas ions, this new particle with a mass in-between that of the proton and the electron was dubbed a meson.

Shortly after the discovery of the pion came something strange: the neutral kaon.

Manifesting itself in the cloud chamber as a decay seemingly appearing in the middle of the detector due to its neutral charge, this new meson didn't seem to fit in to the same framework as the pion. The Kaon became the first of the V-particles, named due to the characteristic shape of their two decay tracks within cloud chambers. These V-particles exhibited new and unusual properties [2]. Some seemed to have longer lifetimes than expected [3]. Some seemed to be forbidden from decaying through certain decay channels [4]. As the experiments progressed, the number of newly discovered unstable particles exploded. In order to explain this new menagerie, new fundamental properties of matter were needed to put these discoveries in order.

One such property, nicknamed "strangeness", was observed to be conserved through strong interactions [5], [6]. This conservation leads to particles that contain a "unit" of strangeness, such as the kaon, having longer lifetimes than unstable non-strange particles of similar mass. Theoretical physicists Murray Gell-Mann and Yuval Ne'eman separately proposed a new formulation for grouping these particles together, dubbed "the Eightfold Way" [7].

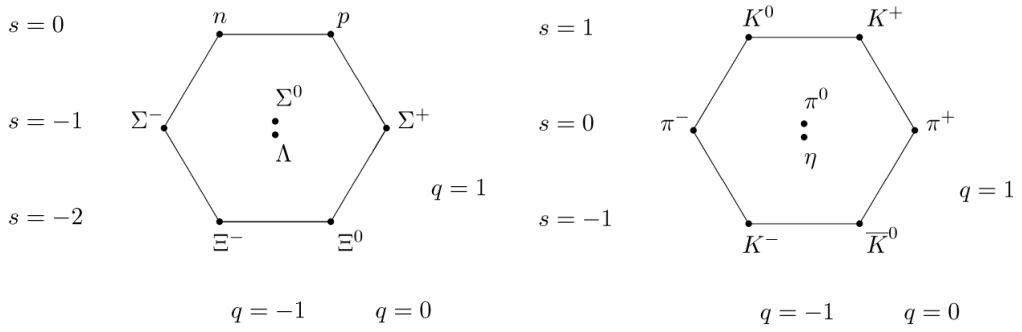

Figure 1.1: An example of the octet configuration put forth in the "Eightfold Way" for spin $\frac{1}{2}$ baryons (left) and spin 0 mesons (right), showing the symmetry between the two types of hadron. Note that here the parameters are strangeness s and electric charge q, rather than the originally used hypercharge Y and isospin T_3, though the effect is the same [8], [9].

The "Eightfold Way" described the newly discovered particles with the group representation of a new SU(3) symmetry. This resulted in the heavier particles, named baryons, forming octet and decuplet states, and the lighter particles, named mesons, forming an octet and a singlet state (see fig. 1.1). This formulation relied on a new conserved quantity named hypercharge, which was formulated as the baryon number (1 for baryons, -1 for anti-baryons, and 0 for mesons) plus the strangeness of the particle. The hypercharge was seen as a fundamental property of matter, and its conservation helped explain what experimentalists were seeing at the time.

At this point, the newly discovered mesons and baryons (together known as hadrons) were starting to fall into ordered sets governed by a new underlying symmetry. This symmetry was expanded upon to match experimental data until, in 1963, Gell-Mann and George Zweig proposed a physical underpinning of this symmetry: quarks[10], [11]. If hadrons were not fundamental particles, but instead composite particles made up of a set of more fundamental particles called quarks, then perhaps the properties of these quarks could explain the symmetries that seemed to be present in the mesons and baryons. Since the baryons had half-integer spin, these new quarks would need to be fermions, with half-integer spin as well. However, the Fermi-Dirac statistics governing fermions would not allow quarks within a hadron to occupy the same state, which conflicted with some of the observed baryon properties. This dilemma was solved when a new integral charge, named color charge, was proposed as a property carried only by the quarks[12], [13].

The new color charge could take on three different values: red, green, and blue (or anti-red, anti-green, and anti-blue for the antiquarks). This triplet of color charge would then give rise to the exact symmetry structure of the discovered mesons and baryons, with mesons being comprised of a quark-antiquark pair, and baryons (an-

tibaryons) being composed of three quarks (antiquarks), each with a different color charge. The physics of three new color charges interacting gave rise to a set of 8 vector fields, analogous to the electromagnetic field for electric charges, that govern the strong nuclear interaction and bind hadrons together. These fields would eventually be seen as representations of gluons, the force mediators of the strong force.

The first experimental hint that the quark picture was correct came from deep inelastic electron-proton scattering experiments performed at the Stanford Linear Accelerator Center (SLAC). Much like the scattering experiments from nearly 70 years prior that had shown that the atom was comprised of a small, dense nucleus at its center, SLAC used high energy electrons to probe the very heart of the proton[14]. The differential cross section for inelastic lepton-proton scatterings involving a virtual photon can be written in terms of **structure functions** that are dependent on the four-momentum transfer of the interaction. These structure functions are a result of the (at the time unknown) matrix elements for the fundamental interactions between photons and the constituents of the proton [15].

Theoretical calculations based on the existence of point-like particles within the proton predicted that the structure function of the proton that dominated at small angles would be independent of the momentum transfer, Q, at sufficiently large values of Q. Instead, this structure function could be written in terms of a single scale variable known as the **Bjorken-x**:

$$x = \frac{Q^2}{2M\nu} \tag{1.1}$$

where Q is the momentum transfer, M is the mass of the proton, and ν is the energy lost by the electron in the collision[16], [17]. One consequence of this scaling rule was that if the quark model was correct, the scattering cross-section should

remain flat as a function of Q^2, the momentum transfer.[1] Looking at the electrons that had been scattered along small angles, SLAC found that the scattering from the proton as a function of Q^2 was wildly different from elastic scattering behavior, with only a mild dependence on Q^2. (see fig. 1.2). This measured scattering behavior was consistent with theories based on the proton having an internal structure made of point-like particles. Quarks had finally been discovered.

1.2 The Standard Model

In the present day, science's best tool to understand the microscopic world at a fundamental level is the Standard Model. The Standard Model is a theoretical framework that describes the universe as a set of quantum fields, extending everywhere throughout space-time. It is these fields, and excitations of these fields, that create the collection of particles (and their interactions) that make up the macroscopic universe we're familiar with. Excitations of these fundamental fields give rise to the 12 fundamental fermions that make up all matter[2] , as well as four force-mediating bosons and the Higgs particle.

The Standard Model gives a single quantum field theory framework for describing the electromagnetic force, the weak nuclear force, and the strong nuclear force all together. It also gives a mechanism for the fundamental masses of the fermions through the symmetry breaking of the Higgs field, as well as the massive weak force

[1]While initially the cross-section was argued to be flat with respect to Q^2 in the quark model, later calculations showed that renormalization effects cause this flat behavior to break down for any quantum field theory formulation[18] However, the asymptotic freedom inherent in non-abelian QCD leads to an approximate scaling, with the cross-section having a logarithmic dependence on Q^2, which was seen in the experiment[19].

[2]While the standard model describes the universe very well, there are still gaps in what it can explain. Cosmological observations suggest that a form of matter invisible to us (Dark Matter), makes up 85% of the matter of the universe. As of now, the particles of the standard model cannot explain this discrepancy [20].

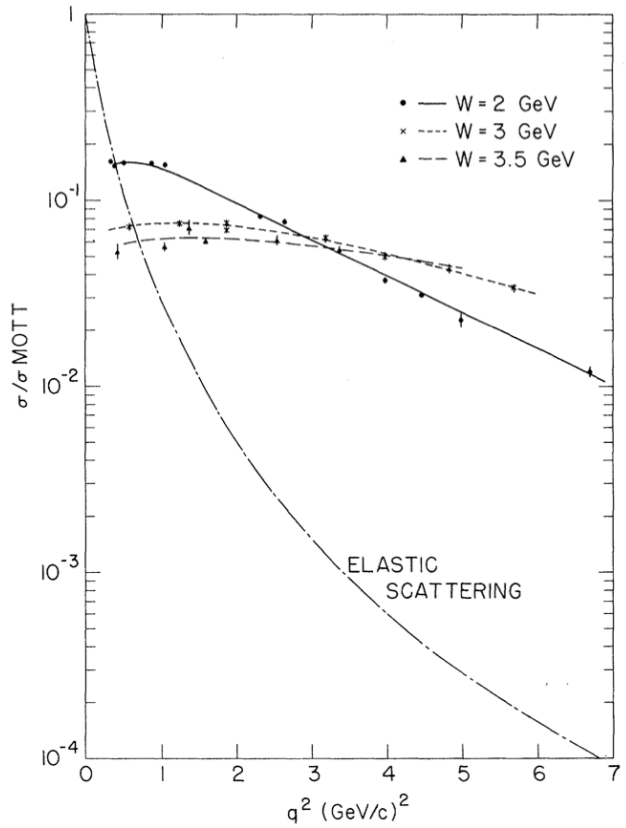

Figure 1.2: Scattering results from SLAC and MIT measuring the cross-section of the proton vs. the momentum transfer $q^2 = -Q^2$. The measured cross-section behaves very different than the elastic scattering cross-section, and the rough independence vs. q^2 agreed with the predictions of a proton made of point-like quarks[14].

carriers, the W and Z bosons. These particles and their properties can be seen in schematic representation in figure 1.3.

The quarks fall into three generations, with the lightest being the up ($2.2\,\mathrm{MeV/c^2}$) and down ($4.7\,\mathrm{MeV/c^2}$) quarks that make up normal nuclear matter. The next heaviest quark is the strange quark, with nearly 50 times more mass than the up quark at $96\,\mathrm{MeV/c^2}$. These three together make up the light flavor quarks, so called because the masses of these flavors of quark are all less than the characteristic QCD scale of $\Lambda_{QCD} \sim 225\,\mathrm{MeV}$[21][3]. At temperatures around 200 MeV, the three light flavors are

[3]Since the coupling strength of the strong interaction α_s varies with the momentum transfer of

often treated as massless to aid in calculations[22][4]. The last three flavors of quarks - charm, bottom, and top - are substantially more massive than the lighter flavors, and therefore are aptly named the heavy flavor quarks. Due to their heavy masses, these quarks can only be created in hard scattering collisions involving very large momentum transfers.

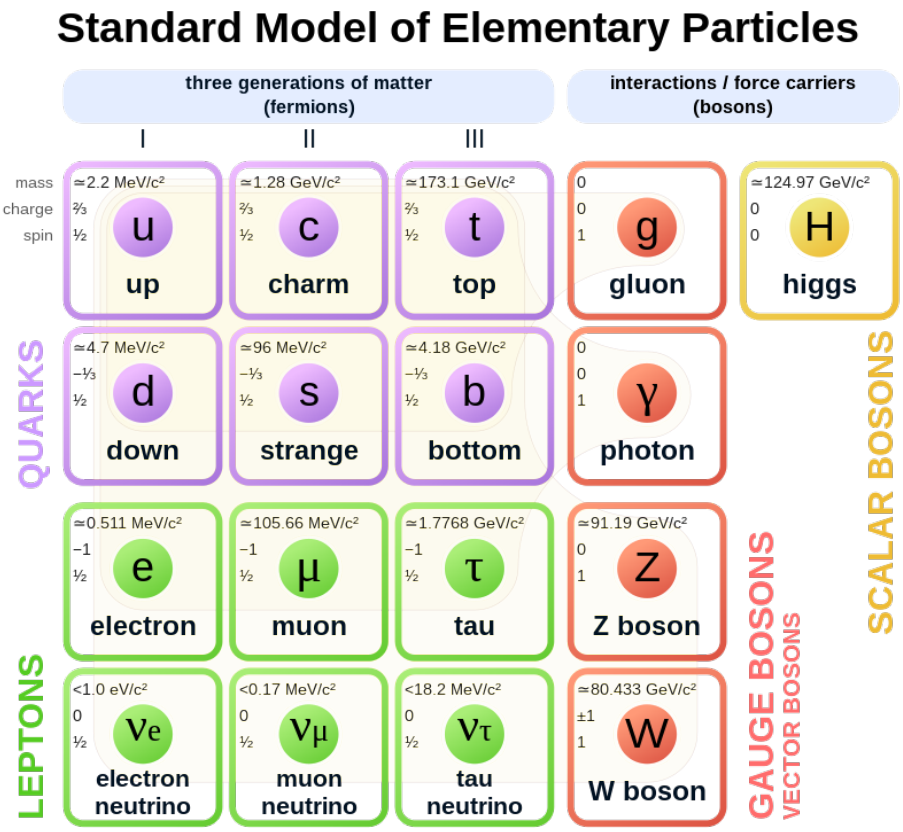

Figure 1.3: Chart of the fundamental particles within the Standard Model [23].

the process involved, the QCD scale Λ_{QCD} is the energy where the coupling constant is ~ 1 and below which perturbative QCD is no longer applicable (i.e. Λ_{QCD} acts as an infrared cutoff).

[4]In QCD renormalization, the mass of the quarks is inversely related to the renormalization scale. This means that at higher probing energies, the masses of the quarks appear lighter. For this reason, QCD loop calculations are often performed by taking the number of flavors of quarks N_f to be only those quarks whose mass lies below the scale of interest, and these are all assumed to be massless. Heavier quarks are then ignored for these calculations

1.3 Quantum Chromodynamics

The theory governing the interaction between quarks and gluons (collectively referred to as **partons**) is an SU(3) gauge theory known as quantum chromodynamics (QCD). The Lagrangian for the QCD component of the standard model is given by[19]:

$$\mathcal{L}_{QCD} = \sum_q \overline{\psi}_{q,a}(i\gamma^\mu \partial_\mu \delta_{ab} - g_s \gamma^\mu t^C_{ab} \mathcal{A}^C_\mu - m_q \delta_{ab})\psi_{q,b} - \frac{1}{4} F^A_{\mu\nu} F^{A\mu\nu}, \tag{1.2}$$

with all repeated indices being summed over. The $\psi_{q,a}$ are the quark field spinors for a quark of flavor q and color $a = 1, 2, 3$. The gluon field is given by $\mathcal{A}^C_\mu$, where C can take on any value from 1 to 8, representing the 8 different types of gluon. The gluon field tensor $F^A_{\mu\nu}$ is defined as:

$$F^A_{\mu\nu} = \partial_\mu \mathcal{A}^A_\nu - \partial_\nu \mathcal{A}^A_\mu - g_s f_{ABC} \mathcal{A}^B_\mu \mathcal{A}^C_\nu, \tag{1.3}$$

with f_{ABC} being the structure constants of the SU(3) group and t^C_{ab} the generators of SU(3).

As written above, the form of the QCD Lagrangian is a sum of four terms. The first is the kinetic component of the quark spinors, $\overline{\psi_q}\gamma^\mu \partial_\mu \psi_q$. The second term is the interaction between the quark spinor fields ψ_q and the gluon fields $\mathcal{A}^C$. The presence of the generators $t^C_{a,b}$ in this term shows that the gluon interaction rotates the quark spinor in color space. The QCD coupling factor, g_s or $\alpha_s = \frac{g_s^2}{4\pi}$, dictates the strength of the quark-gluon interactions, and is the sole fundamental parameter of QCD. The third term is the mass term of the quarks $m_q \overline{\psi_{q,a}} \psi_{q,b}$, and the fourth term describes the gluon fields. Note that within the definition of the gluon field tensors, the gluon field is coupled to itself with the same coupling constant g_s, allowing for gluon-gluon interactions[5].

[5]Specifically, the fundamental Feynman vertices of QCD are the quark-gluon vertex, the three-gluon vertex, and the four-gluon vertex.

Renormalization of QCD leads to the strength of the QCD interaction α_s varying with momentum transfer. As the momentum transfer decreases (i.e. the distance between the interacting quarks increases), the QCD coupling strength quickly becomes greater than 1, and then diverges. This growth of the coupling has two important consequences. First, as the coupling strength approaches 1, perturbation techniques for performing QCD calculations are no longer applicable, and so perturbative QCD's predictive power breaks down. Second, since the coupling strength diverges as distance increases, quarks are confined within bound state hadrons[24]. This means, for example, that if the quark-antiquark pair within a meson are separated, the increasing energy of the color fields between the two make it energetically favorable to create a new quark-antiquark pair from the vacuum, creating two new mesons, rather than separating the original quarks. This property, known as **confinement**, has the effect of forbidding any naked color charge in the universe, instead allowing only color-neutral composite objects like hadrons to exist.

1.3.1 Resonances

Many of these hadrons decay very quickly into lighter particles, primarily via QCD interactions. For these particles, the decay happens probabilistically, and can be modeled by adding a decaying exponential term with characteristic time $\tau = 1/\Gamma$ to the wavefunction. The particle's wavefunction as a function of energy can then be given by[25]:

$$\Psi(E) \sim \frac{1}{E - M + \frac{i\Gamma}{2}} \tag{1.4}$$

$$\rightarrow |\Psi(E)|^2 \sim \frac{1}{(E-M)^2 + \left(\frac{\Gamma}{2}\right)^2} \tag{1.5}$$

Here, the parameters M and Γ represent the mass peak and width of the mass

distribution, respectively. The relationship between the mass width Γ and the characteristic lifetime τ is a manifestation of the quantum uncertainty relation between ΔE and Δt: the shorter a particle species' mean lifetime is, the wider its mass distribution will be, and vice versa. This distribution is known as a Breit-Wigner distribution[6], and particles that follow it are known as **resonances**.

Since resonance states decay into less massive and more stable particles, any resonance particle can itself be construed as the decay child of an even more massive, even shorter lived resonance particle. A QCD-naive approach to this "ladder" of resonances, known as the statistical bootstrap model (SBM), can be used to calculate the number of possible resonant states in a specific mass interval[26]. While this method is somewhat obsolete within the current Standard Model picture of quarks, it does give the interesting result that for any sort of hadron gas, there is a temperature limit, known as the Hagedorn temperature $T_H = 160\,\mathrm{MeV}$, above which the existence of bound resonance states appears to vanish[27]. This limit would later be reinforced using perturbative QCD in high energy regimes, where a state of asymptotic freedom was predicted at roughly the same temperature.

1.3.2 Hard Scattering and Jets

Partons that undergo **hard scattering** interactions (i.e. interactions with a large exchange of momentum Q^2) tend to produce back-to-back showers of hadrons known as **jets**[7]. In these cases, the initial result of this hard scattering that leads to jets can be calculated via perturbative QCD calculations, due to the large Q^2 and therefore

[6]The ubiquity of this distribution in various fields leads to it having many names, depending on who you're asking. It is also known as the Cauchy distribution (named for mathematician Augustin Cauchy), and the Lorentz distribution (named for physicist Hendrick Lorentz).

[7]While often jets are observed as back-to-back pairs (dijet events), the fundamental Feynman vertices allow for gluon splitting to produce trijets in hard scatterings as well, though this is a more rare process [28].

small α_s. Calculations in this regime show that these initial partons can undergo branching that results in, for example, small angle gluon radiation. Repetition of this parton branching leads to a shower of partons being produced, traveling in roughly the same direction as the initial high momentum parton. Eventually, after the initial partons branches a great number of times, the parton will have lost enough energy such that no more branching can occur[29].

Because partons must always be confined inside color neutral objects, after these parton showers are produced, some form of hadronization must take place. However, hadronization is not a calculable process in QCD, so phenomenological models are needed to describe how the high energy parton showers turn into their final state hadrons. One such model that is often used, the Lund string model, treats the gluons (which contain color charge themselves, and are therefore attracted to each other) between partons as color field lines. These field lines contract due to their mutual attraction to form color flux tubes, known as strings. As the distance between the partons increase, the energy of the color string, which is uniform along the string, also increases. Eventually, as this energy increases high enough, the string "breaks" via spontaneous quark-antiquark production, forming new hadrons along its length. The fraction of the energy of the initial parton that is carried by a specific hadron species in the jet is given by the **jet fragmentation function**, which can be studied in high energy collisions.

1.3.3 Asymptotic Freedom & The Quark Gluon Plasma

Just as confinement of colored objects follows from the increasing QCD coupling at large distances, the decrease in the coupling at small distances also leads to new behavior. Since α_S decreases as momentum transfer increases, there should be a

region of very short distance where the strength of the QCD interaction is much weaker[30]. This phenomenon is known as **asymptotic freedom**, and is a fundamental property of QCD. This discovery allowed for accurate predictions of the results of deep-inelastic scattering experiments, since the behavior of scattering with large momentum transfer, and therefore small coupling strength, is solvable using perturbation theory techniques[31].

Another important consequence of the discovery of asymptotic freedom was the prediction of a new state of matter: the **quark-gluon plasma** (QGP)[32]. At extreme temperatures and densities, such as those that would have been present in the universe mere microseconds after the big bang[33], the asymptotic freedom of QCD implies that the interactions between quarks should be small. Much like how a conventional plasma is formed when energies are high enough to allow positive and negative particles to interact without falling into bound states, the QGP would exist in energy regimes where quarks are no longer bound together in hadrons, but instead allowed to interact quasi-freely with each other in a deconfined state[34].

1.4 Heavy-Ion Collisions: QGP in the Lab

The only avenue for studying the properties of the QGP in a laboratory setting is through relativistic heavy-ion collisions. These collisions, which are performed by accelerating the nuclei of heavy elements such as gold (Au) or lead (Pb) up to relativistic speeds before colliding them, are able to briefly create temperatures well above where the QGP should form[35]. However, this high temperature state will only last for an extremely short time, on the order of a few femtoseconds, before cooling down and reforming hadronic matter. It is therefore useful to consider heavy-ion collisions as occurring in semi-discrete stages (see fig. 1.4).

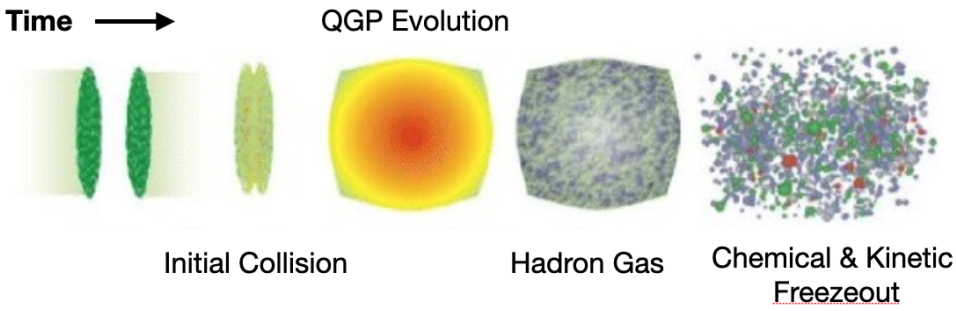

Figure 1.4: Cartoon depicting the evolution of a heavy-ion collision, beginning on the left pre-collision, and ending with the particles streaming into the detector. Adapted from S. A. Bass.

As the heavy ions are traveling at a significant fraction of the speed of light before the collision, the nuclei themselves are Lorentz contracted in the laboratory frame in the direction of the beam. As the two nuclei approach and overlap, individual nucleons will collide with each other, producing new particles from parton-parton interactions. As new particles are produced, the energy density quickly reaches a point above the phase transition temperature of hadronic matter (on the order of 10^{-24}s after the collision[36]), and the QGP is formed. Once formed, partons within the QGP interact with each other to quickly reach a thermal and chemical equilibrium. As the QGP expands and cools, it falls below the critical phase transition temperature and hadronization occurs. Now a hadronic gas rather than a QGP, the collision volume continues to expand until inelastic collisions between the hadrons cease, a point called the **chemical freeze-out temperature**. Finally, the gas cools and reaches the **kinetic freeze-out temperature**, where elastic collisions between the hadrons also cease, and the hadrons free stream into the detector.

1.4.1 Geometry of a Collision

Before delving into the details of the experimental signals of QGP in heavy-ion collisions, and the many techniques used to measure these signals, it's important to understand the common variables used by the experimental heavy-ion community. Since many particle detectors in collider experiments are cylindrical in nature (compared to, say, fixed target experiments), it is natural to choose a cylindrical coordinate system when looking at the detector signals. However, when looking at a particle collision in the rest frame of the collision center of mass, it makes more sense to consider a spherical coordinate system centered on the collision. For these reasons, often a combination of cylindrical and spherical coordinates are chosen for experimental measurements.

The common choice of axes is to have the Z axis defined as being along the particle beam axis, and the XY plane perpendicular to the beam direction denoted as the transverse plane (fig. 1.5). With this orientation, an azimuthal angle φ is used to denote orientation in the transverse plane, and a polar angle θ is used to denote angle from the Z-axis. With this arrangement, since the particle beams are defined to be in the Z direction, any final state momentum in the transverse plane must then be produced via interactions within the collision. This creates a natural division of a produced particle's momentum $\mathbf{p}$ into components of Z momentum p_Z and **transverse momentum** $p_{\mathrm{T}} = \sqrt{p_X^2 + p_Y^2}$.

However, because collider experiments involve initial relativistic particle velocities in the Z direction, the polar angle θ is not particularly useful in collider experiments, as it is not Lorentz invariant and will change between different reference frames. A more useful variable to measure is **rapidity**, defined as:

$$y = \frac{1}{2} \ln \frac{E + p_Z}{E - p_Z} \tag{1.6}$$

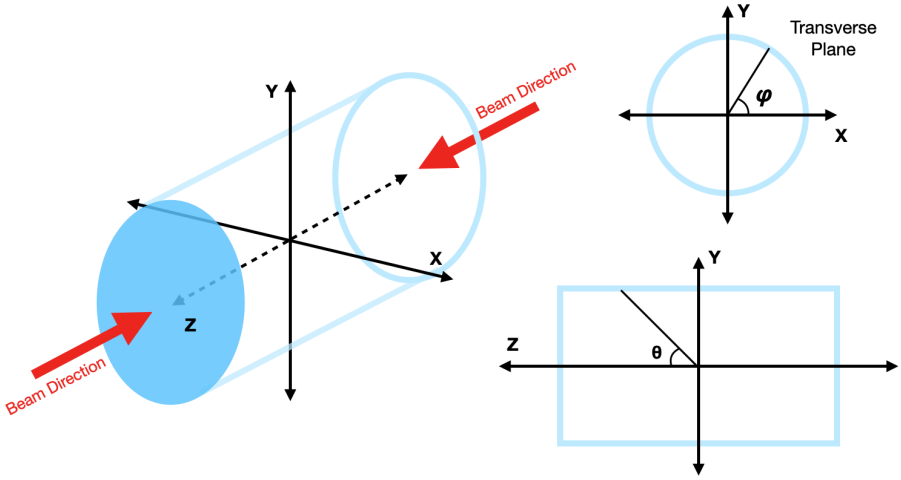

Figure 1.5: Schematic diagram of the collision geometry used in collider experiments. The light blue represents a typical cylindrical detector.

where E is the relativistic energy $E = \gamma mc^2 = \sqrt{m^2c^4 + \mathbf{p}^2c^2}$. Rapidity is used experimentally because particle production within collisions is roughly constant as a function of rapidity near $y = 0$, and because differences in rapidity (Δy) are Lorentz-invariant. More specifically, the shape of the distribution of produced particles in rapidity space dN/dy is invariant under Lorentz boosts in the Z direction.

Often times in experiments, the total relativistic energy of a particle isn't fully known, and so another variable, **pseudorapidity**, is used instead. Pseudorapidity is defined as:

$$\eta = \frac{1}{2} \ln \frac{|\mathbf{p}| + p_Z}{|\mathbf{p}| - p_Z} \tag{1.7}$$

$$= -\ln\left[\tan(\theta/2)\right] \tag{1.8}$$

Pseudorapidity allows for a way to look at an observable related to the polar angle θ, while still having differences ($\Delta\eta$) be Lorentz-invariant (see fig. 1.6).[8]

[8] As opposed to differences in rapidity, differences in pseudorapidity are only truly Lorentz-invariant in the case of massless particles. However, in the case that the mass is small compared to the particle's momentum, this invariance still approximately holds.

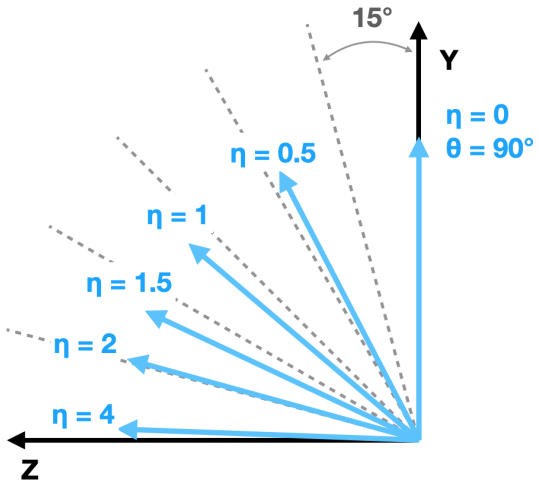

Figure 1.6: Examples of different pseudorapidity values and their relation to the polar angle θ for reference.

1.4.2 Multiplicity & Centrality

It can be useful to categorize heavy-ion collisions based on the amount of event activity produced. The experimentally measurable way to do this is using the event multiplicity, or total number of particles produced within a collision. Conventionally, events are separated into multiplicity percentiles, with events within the 0-10% decile being those with the highest multiplicity, and those within the 90-100% decile being those with the lowest multiplicity.

Another useful way to categorize heavy-ion events is through event centrality. Centrality can be defined using the impact parameter of the collision (i.e. the transverse distance between the centers of the two colliding nuclei). Like multiplicity, centrality is conventionally broken up into percentiles of the total cross-section, with the 0-10% decile referring to the most central collisions (those with the smallest impact parameters), and the 90-100% decile referring to the most peripheral collisions (those with the largest impact parameters).

Since the impact parameter in a heavy-ion collision is not directly measurable, a

model must be used to estimate the centrality of a given event based on the observed multiplicity. A common model for this purpose is the Glauber model, which uses the nuclear density functions of the two nuclei to randomly distribute the nucleons for each simulated collision [37]. The heavy-ion collision is then broken up into a collection of nucleon-nucleon collisions, with the number of participating nucleons denoted as N_{part}, while the non-participating nucleons (known as spectators) continue in the direction of the beam[9] (see fig. 1.7). Since each participating nucleon might be involved in multiple scatterings, another useful parameter is the number of binary collisions that occur, denoted N_{coll}. This model then gives us a relationship between centrality/impact parameter and N_{part} and N_{coll} involved in the collision.

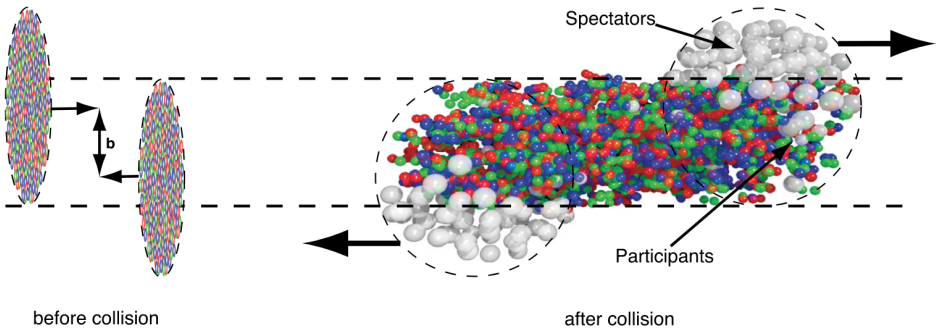

Figure 1.7: Cartoon of a heavy-ion collision showing the Lorentz contracted nuclei pre-collision, and the nucleon participants and spectators after the collision[38].

Next, a relationship between multiplicity and number of participants N_{part} is needed. To do this, the multiplicity can be divided into a "soft" part that scales with N_{part}, and a "hard" part that scales with N_{coll}, giving the relationship:

$$\frac{dn}{d\eta} = (f)\langle N_{part}\rangle + (1-f)\langle N_{coll}\rangle \tag{1.9}$$

where $dn/d\eta$ is the multiplicity per pseudorapidity, and f is a parameter that determines the participant vs. binary collision scaling[39]. With this relationship in

[9]The actual treatment is slightly more complex, since nucleons can undergo multiple scatterings, and additional scattering terms can interfere to produce "shadowing"[37].

hand, and with the Glauber model giving a relation between N_{part} and N_{coll} and impact parameter, it is now possible to take the measured multiplicity over a large number of events, and separate out this distribution based on the centrality of the collisions. An example of this separation is seen in figure 1.8 for ALICE Pb-Pb collisions. Here, VZERO amplitude is an uncorrected stand-in for charged particle multiplicity, and it can be seen that the Glauber model fits very well with the measured multiplicity data. This enables us to study collisions with different centralities based on the measured event multiplicity. Characterizing events by multiplicity can also allow for a more direct comparison between different collision systems, allowing comparisons to be made between measurements taken in proton-proton, proton-lead, and heavy-ion lead-lead collisions.

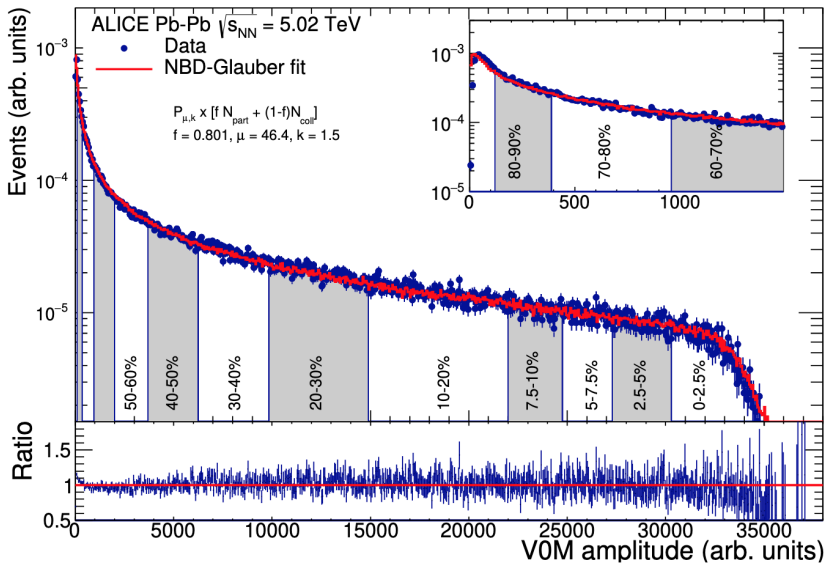

Figure 1.8: Example of how the Glauber model is used to relate charged particle multiplicity (here VZERO amplitude as an uncorrected stand-in) to the centrality of the collision[40].

1.5 Experimental Signatures of the QGP

Since the QGP produced within heavy-ion collisions should last only fractions of a second once formed, experiments must look for signatures within the final state hadrons that give information about the early QGP phase of the collision. While there are a multitude of QGP signatures within the current theoretical and experimental heavy-ion literature, the main focus of this thesis will lie in three signatures specifically: strangeness enhancement, jet modification, and collective flow. In each of these cases, deviations from the behaviour observed within proton-proton collisions helps give evidence for the presence of this new state of matter.

1.5.1 Strangeness Enhancement

One of the first predicted signatures of the formation of a QGP in heavy-ion collisions was an increase in strangeness production, measured as the production ratio of strange quarks to up and down quarks [41]. Since real strange quarks are not present in nuclear matter - the valence quarks of protons and neutrons being only up and down quarks - all strangeness created in a collision must be created via inelastic production processes. The enhancement in heavy-ion collisions was initially predicted due to the fact that the temperature of the QGP allows for the thermal production of the heavier strange quark through gluon fusion in the medium producing strange quark-antiquark pairs ($gg \rightarrow s\bar{s}$)[42]. Provided these strange quarks survive through re-scattering and the hadronization process, this enhancement would lead to an increase in observed strange hadrons among the final state particles.

1.5.1.1 Strangeness Suppression

In order to establish an enhancement of strange quark production in heavy-ion collisions, a thorough understanding of the expected baseline production in smaller systems such as pp collisions is necessary. The up, down, and strange quark were initially treated using an SU(6) representation for the symmetry between the light mesons and baryons. However, since the strange quark is considerably more massive than the up or down quarks, a suppression factor λ was defined to characterize how the mass of the strange quark breaks this SU(6) approximation [43]. This factor is defined using the mean number of up, down, and strange quarks (and antiquarks) produced in a collision:

$$\lambda = \frac{2\langle n_{s\bar{s}}\rangle}{\langle n_{u\bar{u}}\rangle + \langle n_{d\bar{d}}\rangle}. \tag{1.10}$$

Here, a value $\lambda = 1$ would indicate a completely symmetric treatment of the up, down, and strange flavors. Due to the larger mass of the strange quark, numerous collider experiments [44], [45] used particle ratios to measure a value of $\lambda \sim 0.2 - 0.3$ in pp collisions across a range of center of mass energy from 20 GeV to 1 TeV [46].

Along with the determination of the strangeness suppression factor, these studies in relative particle abundances determined that a canonical ensemble model could describe these ratios relatively well for light flavor particles. These models rely on a temperature T and strangeness fugacity $\gamma_s = e^{\mu_s/T}$ [47]. The fugacity parameter gives the amount of phase space that the strange quark is able to occupy within a hadronic gas. If $\gamma_s = 1$, then the strange quark is in full equilibrium with the other light quarks, while a value $\gamma_s < 1$ reflects a system where strange quarks haven't had the time (or energy) to fully equilibrate. In pp collisions, γ_s is measured to be ~ 0.5 [48]. This is essentially the equivalence of treating the collision products as going through a canonical hadronic gas phase, where changes to the relative abundances

of particle species would be constrained by the rate of specific hadronic interactions, rather than the chemical potentials of the ensemble. In this case, the number of hadrons produced is fairly low and the strangeness must be exactly conserved in each interaction [49].

1.5.1.2 Grand Canonical Model of Strangeness Production

Unlike the lower multiplicity pp collisions, the multiplicities found in heavy-ion collisions are high enough to move towards a grand canonical model of light flavor production. In this framework, at the energy density of a heavy-ion collision the equilibrated QGP can produce strange, up, and down quarks within a similar phase space, pushing the value of γ_s to ~ 1. This allows for the production to be modelled statistically using just the temperature T and the baryon chemical potentials μ_b, rather than explicitly enforcing the microscopic conservation conditions (see figure 1.9).

Note that a grand canonical model does not necessarily imply the existence of a QGP, since a large enough hadronic gas can also be described with these parameters. However, in order to explain the relative abundance of different strange species to each other (e.g. Ξ/ϕ), a hadronic gas grand canonical phase does not match the observed dependence on **total** strangeness ($s + \overline{s}$), rather than **net** strangeness ($s - \overline{s}$) [50]. For multi-strange hadrons to be produced solely within a hadronic gas, a sequence of hadronic interactions would be necessary that would require an un-physical lifetime of the hadron gas phase, while the QGP can produce $s\overline{s}$ pairs in abundance from gluon fusion in a very short time-frame [51]. This points to the strangeness enhancement in heavy-ion collisions being almost entirely driven by the pre-hadronic QGP phase.

The relative success of the statistical model in recovering the abundances of

strange and non-strange particle species with a single temperature parameter strongly suggests that the overall particle abundances in heavy-ion collisions are determined by the thermalized QGP [52]. Moreover, the increase in strangeness production is seen to plateau at multiplicities found in more central heavy-ion collisions [53]. This saturation of strangeness enhancement is well explained by the grand canonical statistical model of the QGP medium [54], where above a certain system size there is no further strangeness enhancement since the up, down, and strange quark production would be in equilibrium.

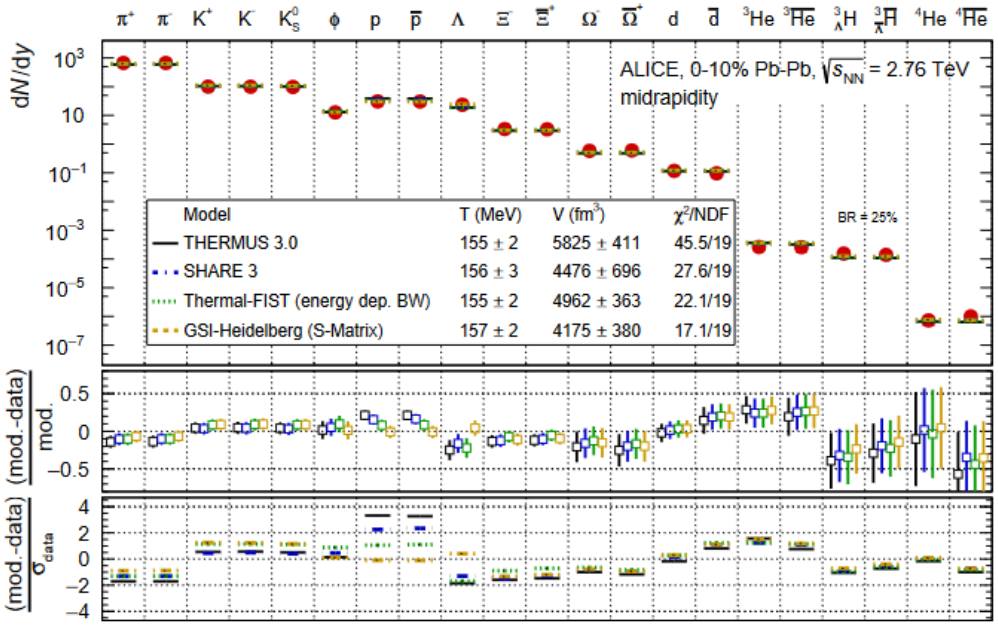

Figure 1.9: Graph showing the comparison of different light flavor particle multiplicities (per unit rapidity) in central heavy-ion collisions compared to different thermal models. From the ratio of model to data (shown in the middle and bottom plots), the thermal models still slightly under-predict the multi-strange containing hadrons, while over-predicting some baryons like the proton [52].

1.5.2 Jet Quenching

Much like how an electrically charged probe traveling through a medium can tell us about the medium's electrodynamic structure based on the energy lost as the probe travels, so too can high momentum partons be used as probes of the QGP medium. However, as described in section 1.3.2, these high momentum partons are not experimentally accessible, manifesting themselves instead as jets of hadrons all traveling in a similar direction within the detector. The energy loss of a high momentum parton in the QGP medium must then be inferred from the final state of the hadron jets. Changes in the jet energy, multiplicity, shape, and hadrochemistry can give us experimental data that can help constrain how these hard probes are interacting with the QGP.

Within a heavy-ion collision, the location of the hard scatterings that lead to dijets being produced should be distributed roughly uniformly within the collision overlap region over a large enough sample of collisions. Because of this random distribution, typically one of the jets will be pointed more towards the "edge" of the collision region, while the other will be pointed more towards the center of the collision region. This means that for dijets produced in a heavy-ion collision, one of the jets will usually have a longer path length traveling through the QGP medium. As this parton travels through the QGP, it loses energy via gluon radiation and collisions within the medium[55], as depicted in the cartoon in figure 1.10.

This asymmetric energy loss in one of the dijets can by seen experimentally by looking for high momentum particles - which most likely belong to a high energy jet that had a short path length through the medium - and measuring the particle production on the opposite side of the collision, where the recoil jet would normally be. First measured by the STAR collaboration at RHIC[57], this phenomenon, known

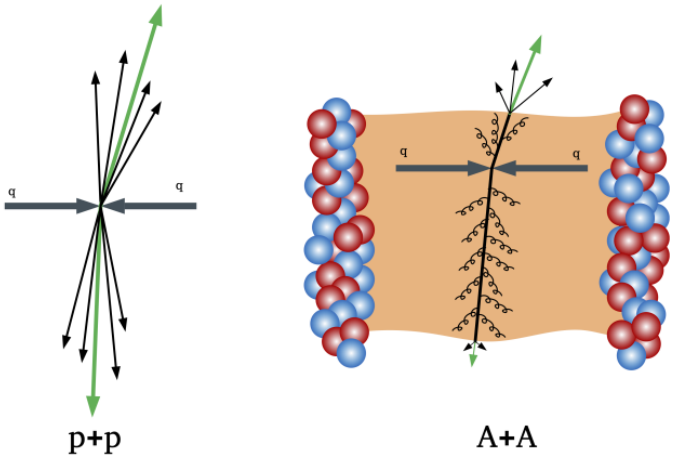

Figure 1.10: Cartoon depicting a parton losing energy in heavy-ion collisions, leading to the QGP signature of jet quenching. Credit: CERN, ATLAS collaboration[56]

as **jet quenching**, is a clear signature that high momentum partons are losing energy within the collision medium, and that this energy loss is path length dependent. This strong energy loss of high momentum partons was first seen as a surprising result: in the perturbative QCD limit, the QGP was originally predicted to behave like a weakly coupled ideal gas. This strong energy loss pointed instead towards a strongly coupled fluid. Numerical Lattice QCD calculations have suggested that some deviation from the ideal gas limit at high temperature is expected ($\approx$ 20% deviation) [58], [59]. However, this deviation is thought to not be sufficient to describe the large strength of these QGP medium interactions, and thus these jet-medium interactions are still not understood on a microscopic level [60].

1.5.3 Collective Flow

Since individual partons within the QGP should strongly interact with the overall medium, collision systems that produce QGP should show the emergence of collective phenomena in the final state hadrons. One way the collective behavior of the medium can be modelled is through **collective flow** components. One method of explaining

collective flow is by using a hydrodynamic model, as depicted in figure 1.11. This cartoon roughly depicts the process of collective flow within heavy-ion collisions in the following way:

i. A collision between two nuclei with a non-zero impact parameter results in an anisotropic, almond-shaped collision region (dotted line) where the initial QGP is formed.

ii. As the QGP expands, it quickly thermalizes[10], the spatial anisotropy is "frozen" into the system as a pressure gradient that is larger along the short axis, and smaller along the long axis. This can be thought of as a consequence of the directional-dependent path length of a parton traveling through the QGP.

iii. This difference in pressure gradients results in an anisotropic momentum distribution in the final state hadrons, with more high momentum hadrons being produced in the direction of the steepest pressure gradients.

This flow in momentum space can be expressed as a Fourier series in the azimuthal angle φ, with the typical form:

$$\frac{dN}{d^2\mathbf{p}_T} = \frac{dN}{2\pi p_{\mathrm{T}} dp_{\mathrm{T}}}\left(1 + \sum_{n=1}^{\infty} 2v_n \cos\left(n(\varphi - \Psi_{RP})\right)\right), \tag{1.11}$$

where Ψ_{RP} is the angle of the reaction plane, which is defined by the line connecting the centers of the two nuclei at the moment of impact. Conventionally, the first two Fourier coefficients are known as **directed flow** (v_1) and **elliptical flow** (v_2).

[10]Since the anisotropy of the initial collision region is "washed out" as the system expands prior to thermalization, the timing of when the system thermalizes determines how much of the initial anisotropy is preserved in the final state momentum distribution. Experimental results suggest an almost instantaneous thermalization in the hydrodynamic picture, giving more weight to the description of the QGP as "strongly interacting."

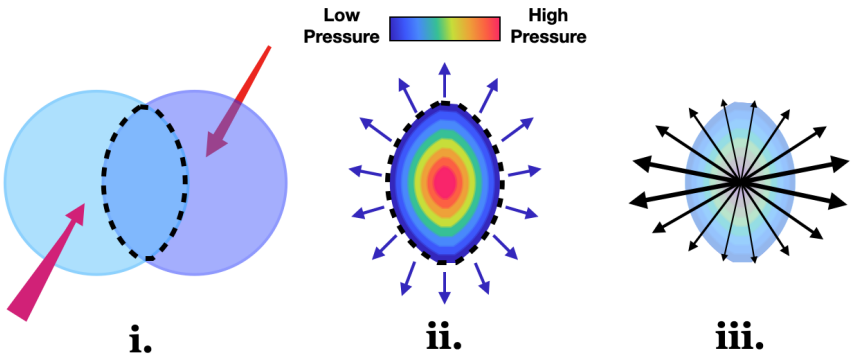

Figure 1.11: Cartoon depicting a hydrodynamic toy model for how an initial anisotropy in space within the collision region (i.) can lead to an anisotropy in momentum distribution for the final state hadrons (iii.).

In the cartoon example of figure 1.11, the initial almond shape of the collision area leads to a large elliptic flow component.

The large flow coefficients measured in semi-peripheral heavy-ion collisions have been interpreted as a signature of hydrodynamic behavior in the initial strongly interacting medium. In fact, the initial flow measurements in Au+Au collisions from the STAR collaboration were consistent with the perfect hydrodynamic limit[61]. Moreover, recent studies have measured non-zero flow coefficients for smaller collisions systems as well, including p-Pb and even high multiplicity pp collisions[62].

1.5.4 Small systems: the Onset of Collectivity?

As discussed above, the success of hydrodynamical and statistical models to describe the collective behaviour found within heavy-ion collisions has pointed to the presence of a strongly interacting, thermalized QGP. However, more recent measurements have shown that these signals also appear both in smaller systems like pp collisions and larger systems like PbPb collisions. Instead, the important system parameter seems

to be the event multiplicity, regardless of the collision system. This can be viewed as evidence of the formation of "QGP droplets" in small collision systems.

While these signatures of collective behavior are present in pp and p-Pb systems, the use of hydrodynamics in explaining them in small systems is still an active topic of debate. The two primary assumptions of the hydrodynamic model of heavy-ion collisions - that the system is in equilibrium and that the system size is much larger than the mean free path of the partons - are challenged by smaller collision systems. The strength of the observed collective behavior means these signatures would have to have been generated in small systems even earlier than the predicted time it takes gluons to thermalize, and the mean free path assumption does not hold in these small QGP droplets. However, new theoretical studies are investigating how and why hydrodynamic models can still match the results of these small systems, even when these systems don't meet the assumptions of traditional hydrodynamic models[11][63], [64].

This tension in the signatures of a strongly coupled QGP existing in smaller collision systems invites a closer look at the nature of these signals, such as the observed strangeness enhancement. Specifically, if signals in heavy-ion collisions that are interpreted through a hydrodynamic lens also appear in small systems where hydrodynamics doesn't fully apply, then studies in small systems may help identify underlying QCD interactions that mimic hydrodynamic behavior, and may better explain these signals across all system sizes. Especially interesting is the fact that while strangeness enhancement and collective flow are found in pp and p-Pb systems, other signatures associated with QGP formation such as jet-quenching have not been observed [65],

[11]In these new approaches, the damping of "non-hydrodynamic modes" at early timescales can approximate a hydrodynamic evolution in non-equilibrium systems, leading to the ability of hydrodynamic models to match p-Pb, pp, and even e+e- collisions successfully

[66]. This opens the possibility that the observed multiplicity-dependent behaviors commonly attributed to the same QGP phase may in-fact have different points of onset in the collisions, or even separate physical origins altogether.

Experimentally, strangeness enhancement can be measured through the ratio of strange hadrons to charged pions as a function of system size. Comparing the production of strange containing hadrons in this way shows that the increase in production clearly scales with multiplicity, with significant overlap between the highest multiplicity pp, mid-multiplicity p-Pb, and low multiplicity PbPb collisions (see figure 1.12). This enhancement also scales with the number of strange quarks in the measured particle, with the most enhancement seen for the Ω baryon (sss). This fits will with the explanation of strangeness production as a shift towards a grand canonical ensemble as the system size increases. However, the microscopic processes responsible for the smooth increase in strangeness even in lower multiplicity pp and p-Pb collisions is not currently understood. With this in mind, smaller collision systems such as p-Pb, which span the multiplicity range between pp and PbPb collisions, are crucial to understanding the origin of these collective signatures. By more closely examining strangeness production in these intermediate-sized collisions, the origin of strangeness enhancement can be further explored.

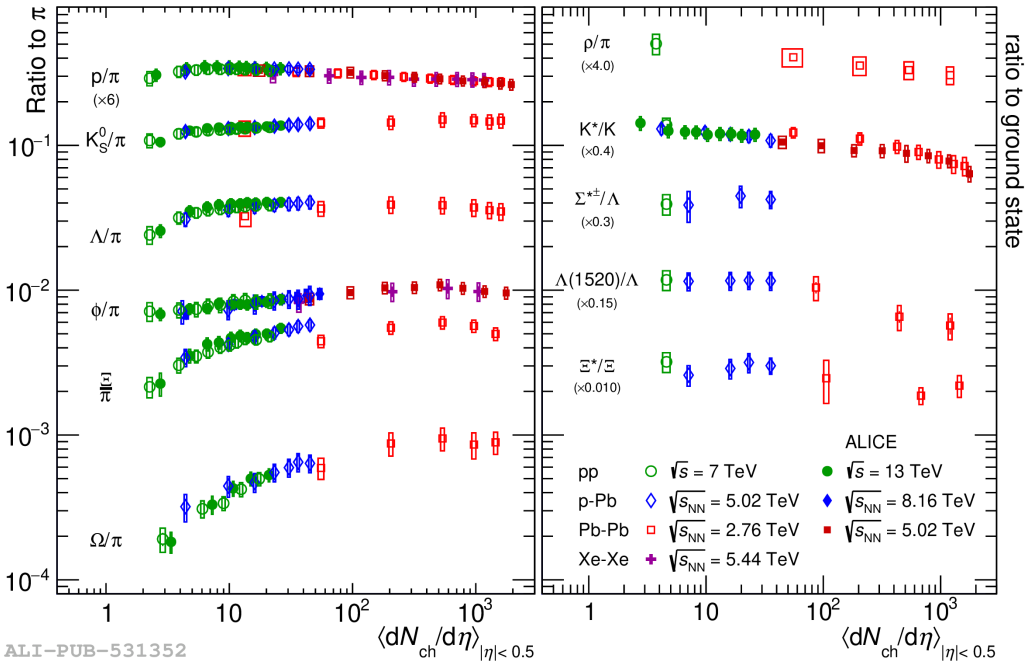

Figure 1.12: (Measurement of the ratio of strange hadrons to charged pions, as a function of multiplicity (left). Strangeness enhancement can be seen in the smooth increase of this ratio as multiplicity increases. Also depicted are resonance ratios to their stable counterparts (right), which show a steady decrease. This decrease is due to the longer time between the chemical and kinetic freeze-out in the collision evolution as system size grows [52].

Chapter Two: Experimental Setup

2.1 The LHC

The Large Hadron Collider (LHC) is currently the largest, most powerful particle accelerator in the world. Run by the European Organization for Nuclear Research (CERN) and located on the border between France and Switzerland, the LHC is a 27 km long circular particle accelerator capable of colliding protons at a center of mass energy of 13 TeV and with a maximum luminosity of 10^{34} $\mathrm{cm}^{-2}\mathrm{s}^{-1}$ [67]. Complimentary to the proton-proton collision program, the LHC is also capable of performing high energy heavy-ion collisions, including with PbPb, p-Pb, and XeXe systems.

For the heavy-ion program, beams of Pb ions are collided together at center of mass energies of 2.76 and 5 TeV per nucleon. The LHC's first data taking period, Run 1, occurred from 2009 to 2013, and included a dedicated PbPb configuration in 2010. After a shutdown of three years to upgrade the detectors, as well as the accelerator itself, the LHC entered its second data taking period, Run 2, from 2015 to 2018. The upgrades performed allowed the LHC to reach its full operating beam energy and its design luminosity in Run 2. During this period, p-Pb and Pb-Pb ions were collided during dedicated runs in 2016 and 2018.

The LHC contains four interaction points along the accelerator ring where the two particle beams cross and collisions can occur. These correspond to the four main detector experiments at the LHC: **A** **T**oroidal **L**HC **A**pparatu**s** (**ATLAS**), **C**ompact **M**uon **S**olenoid (**CMS**), **A** **L**arge **I**on **C**ollider **E**xperiment (**ALICE**), and LHC-

beauty (**LHCb**).

Protons and heavy ions are created at dedicated facilities at CERN (protons from ionized hydrogen gas, lead ions from ultra pure vaporized lead). These particles are then sent through a series of accelerators in order to be brought up to their full energy. The penultimate step is injection into the Super Proton Synchrotron (SPS), where clouds of protons or heavy ions circulate the ring in bunches that are accelerated to 99.9998% the speed of light [68]. These bunches are then injected into the main LHC ring, where they are accelerated to their final energy. Each of these $\sim$ 3000 (600) proton (lead) bunches contains on the order of 10^{11} protons (10^8 lead ions), and is squeezed into a width of approximately 20 μm near the interaction points. At full energy and luminosity, bunch crossings happen at a rate of 40 MHz, or every 25 ns for proton crossings [69]. Though each bunch contains billions of particles, the density of the bunches is such that each crossing will result in an average of $\approx$ 20 collisions for protons. For ion bunches, the odds of a crossing interaction are lower due to the lower density of the bunches. In the case of p-Pb collisions, only 0.06 hadronic interactions occur per bunch crossing, and the rate of p-Pb crossings is $\approx$ 200 kHz [70].

2.2 The ALICE Experiment

The ALICE Experiment is one of the four major detector experiments at the LHC, and is primarily dedicated to heavy-ion physics. Situated underground at the LHC's Interaction Point 2, the ALICE detector was designed explicitly to look for signatures of the QGP produced in high-energy heavy ion collisions. For this purpose, the primary motivation for the detector's design was the ability to deal with high multiplicity Pb-Pb collisions, where upwards of 10,000 charged particles are produced and must be precisely tracked as they travel through the detector.

To achieve this goal, ALICE is composed of several layers of sub-detectors, each with an important role in the tracking and reconstruction of these large multiplicity collisions. Most of these subdetectors comprise the central barrel, and are housed within a large solenoid magnet formerly of the L3 experiment, with a nominal magnetic field of 0.5 T in the particle beam direction. The L3 magnet's strong magnetic field causes charged particles that are produced in collisions to undergo cyclotron motion, with a gyroradius of $r_g = \frac{p_T}{|q|B}$. By having a large magnetic field, and therefore a large gyroradius, high momentum tracks are able to have good momentum resolution in the central tracking detectors by reconstructing their curvature. The ALICE detector's central barrel, measuring approximately $16 \times 16 \times 16$ m^3 in size and weighing $\sim$ 10,000 tons, covers a rapidity window of $-1 < \eta < 1$ and has full coverage in azimuth. When a particle is produced in a collision, it travels through the central barrel detectors in the following radial order: the Inner Tracking System (ITS), the Time Projection Chamber (TPC), the Time of Flight Detector (TOF), and finally the Electromagnetic Calorimeter (EMCAL).

Outside of the central barrel are additional detector components in the forward and backward rapidity regions of the detector. These include the T0 and VZERO detectors, each made up of two end-cap calorimeters on either side of the central barrel, and the Muon Tracker, situated in the forward rapidity direction. The following sections will detail the specific subdetectors used in this dissertation's main analysis.

2.2.1 ITS

The ITS is the detector component that is closest to the beam interaction point, and is therefore vital for the reconstruction of the primary collision vertex. The ITS is composed of three distinct layers of detectors: the innermost Silicon Pixel Detector

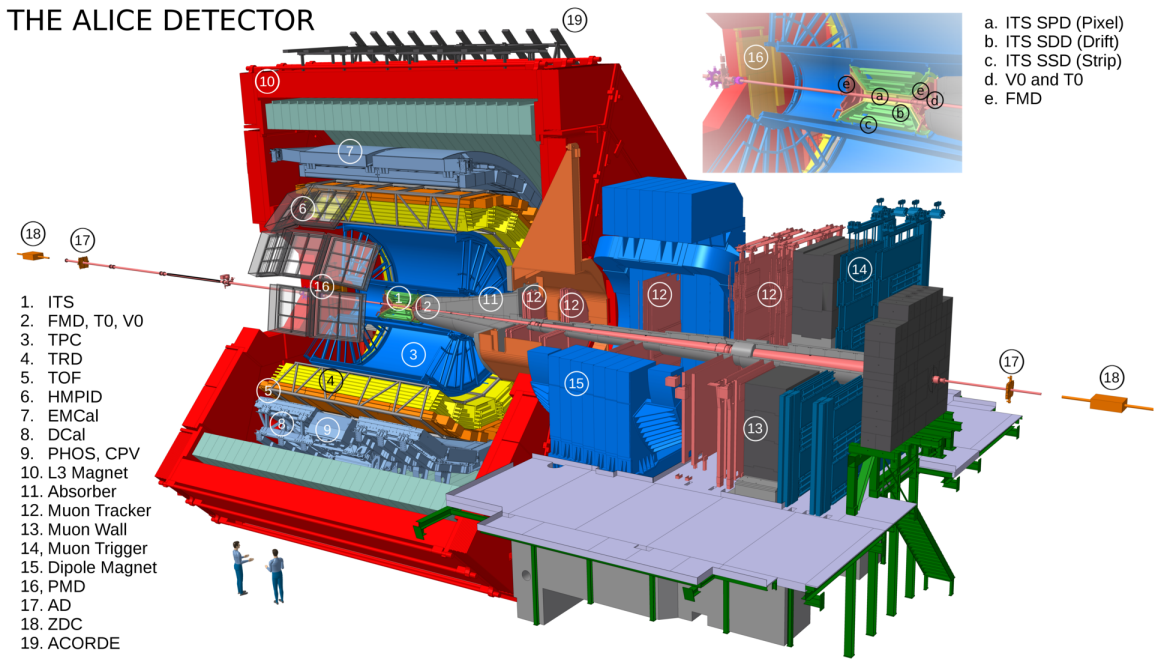

Figure 2.1: Schematic of the ALICE Detector as it was configured for LHC Run 2. The L3 magnet, depicted in red, houses the central barrel, which contains the main tracking detectors of the experiment. The two beams from the LHC are depicted in pink, with the crossover region happening in the center of the ALICE central barrel. Inset in the top right is an expansion of the ITS, the detector component closest to the interaction point. Image provided by ALICE.

(SPD), the middle Silicon Drift Detector (SDD), and the outermost Silicon Strip Detector (SSD). As the SPD sits ∼4 cm from the primary collision point, it is also useful for resolving secondary weak decays that happen small distances away from the initial collision [71]. For the analysis in this thesis, requiring a hit within the SPD layer is used to select only primary tracks (i.e. those tracks produced directly from the initial collision, or produced from resonance decays [72]), while excluding child particles of secondary decays.

2.2.2 TPC

The TPC is the primary tracking detector of the ALICE experiment, and the main component of the central barrel. Covering a pseudorapidity range of $|\eta| < 0.9$ and the full range in azimuth, the TPC is a cylindrical ionizing drift detector that allows for the reconstruction of the tracks of charged particles that are produced in the collisions, as well as allows for particle identification (see figure 2.2). A central electrode is held to a high voltage of 100 kV, which creates a 400 V/cm electric field in the axial direction throughout the detector. The central chamber of the TPC is filled with a mixture of Ne-CO_2-N_2 as the ionizing gas, contained at standard atmospheric pressure [73]. As a charged particle travels through the detector, it ionizes this counting gas. Due to the axial electric field, these ionized molecules drift towards the endplates of the TPC, where a series of high-voltage wire grids cause an avalanche effect in the gas. This takes the small number of ionized gas molecules and amplifies the signal as it approaches the readout wire chambers [74].

Since the primary goal of the ALICE Experiment is to study high multiplicity heavy ion collisions, single track resolution and two-track separation are primary concerns for the TPC. For single tracks, the spatial resolution for track points is $\sim$ 1 mm in the axial and transverse directions. The momentum resolution from the TPC as a standalone detector ranges from 2% to 7% as momentum increases from 1 GeV/c to 10 GeV/c.

In addition to spatial and momentum information, the TPC also functions as a means of particle identification. As a charged particle travels through the gas volume, it loses energy as it ionizes the gas. This energy loss can then be characterized by the Bethe-Bloch function [73]:

$$\langle \frac{dE}{dx} \rangle = \frac{4\pi N e^4 Z^2}{m_e c^2 \beta^2} \left(\ln \frac{2 m_e c^2 \beta^2 \gamma^2}{I} - \beta^2 - \frac{\delta(\beta)}{2} \right) \tag{2.1}$$

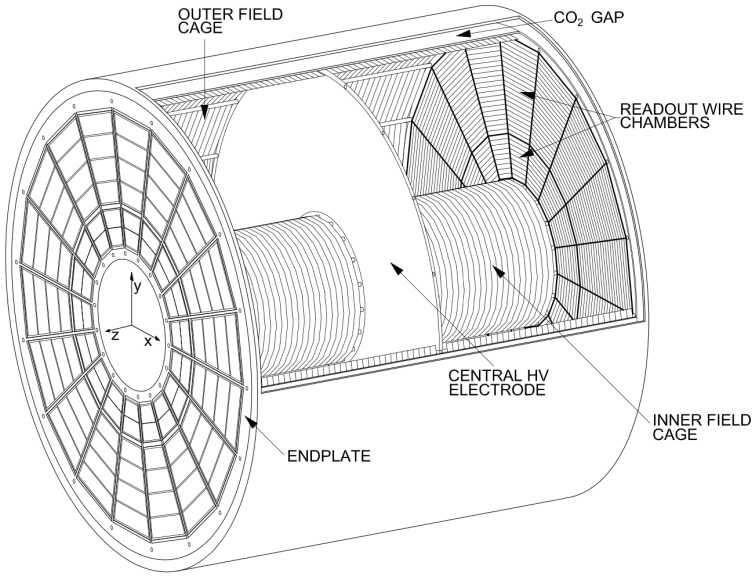

Figure 2.2: Schematic drawing of the ALICE Time Projection Chamber with a cutout showing the inner chamber [74]. A high voltage difference between the central electrode and the endplates causes the ionized gas to drift towards the readout chambers.

where m_e is the mass of the electron, Z is the charge of the particle traveling through the gas, β is the velocity of the particle as a fraction of the speed of light c, and I is the average ionization energy of the gas molecules. Since most of these parameters are fixed by the specifics of the gas chamber, this gives us a relationship between a particle's energy loss, momentum, and mass. Each particle species then has an expected energy loss as a function of its momentum, and therefore can be separated and identified (fig. 2.3). With an energy loss resolution of roughly 5%, the energy loss of a given track can be compared to the expected behaviors of different particle species [75]. Low momentum particles are well resolved by this method. However, even in the higher momentum regions where the different particles overlap, a cut on the expected energy loss can still be useful to minimize background.

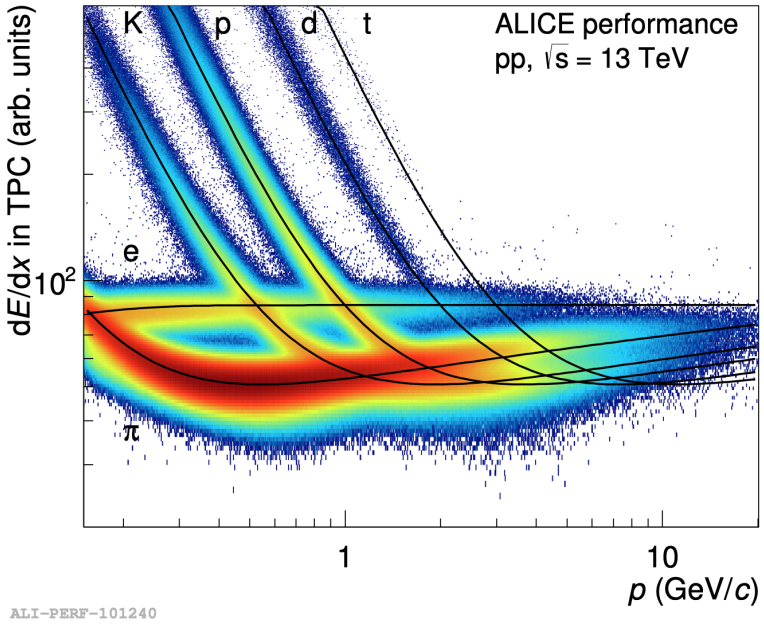

Figure 2.3: Example of the TPC energy loss (dE/dx) vs. momentum for LHC Run2. Expected curves for different particle species are shown in black. Image from ALICE.

2.2.3 TOF

The TOF is a Multigap Resistive Plate Chamber detector that covers the central region of $|\eta| < 0.9$ and full azimuth. It is designed to give particle identification information for particles whose momenta falls outside of the TPC's discriminatory range. The TOF is composed of a cathode and anode surrounding equally spaced layers of resistive plates and a Freon-rich gas mixture [76]. As a charged particle leaves the TPC, it passes through the gas filled gaps of the TOF, ionizing this gas mixture as it goes. This ionization gives an immediate time signal for when the particle hits the TOF. Signals from the endcap T0 detectors are used in order to find the t=0 for the collision to act as a baseline for the TOF measurement. This timing information

can then lead to particle identification using the formula (in natural units):

$$m = p\sqrt{\frac{t^2}{l^2} - 1} \tag{2.2}$$

$$\rightarrow \beta = \frac{1}{\sqrt{1 + \frac{m^2}{p^2}}} \tag{2.3}$$

where m is the mass of the particle, p the momentum, t the time traveled, l the track length, and β is velocity over the speed of light. With a resolution of ≈50 ps [77], this TOF time signal can give good particle mass discriminatory power for medium momentum particles from 0.2 GeV/c to 2.5 GeV/c. Above this, the detector is less able to distinguish between the lighter particles (π, K, e), though it maintains some discriminatory power for the proton (see fig. 2.4).

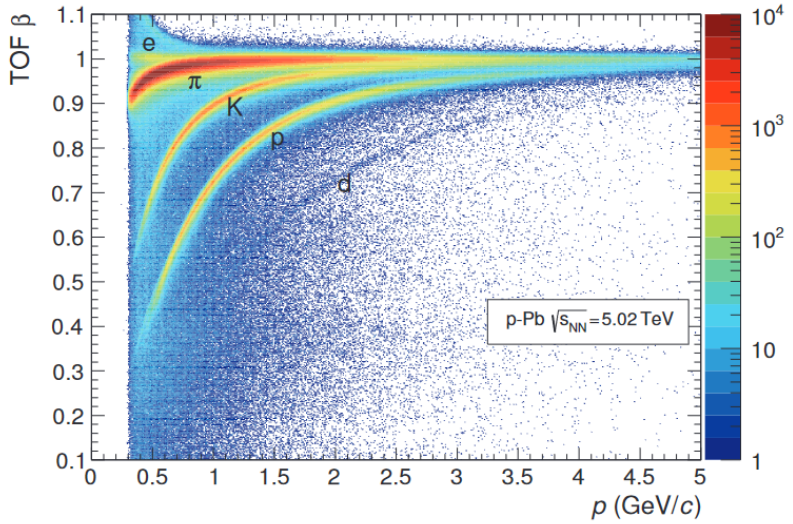

Figure 2.4: Example of the TOF timing signal (here combined with the track length to calculate $\beta = v/c$) vs. measured momentum in p-Pb collisions. The curves for the different particle species (separated due to their mass differences) are labeled in black [70].

2.2.4 VZERO

The VZERO subdetectors are comprised of two end-cap scintillator detectors: V0A, located in the forward rapidity region ($2.8 < \eta < 5.1$); and V0C, located in the backwards rapidity region ($-3.7 < \eta < -1.7$). The VZERO detectors, being outside of the central rapidity region used for the main measurements in this thesis, are crucial for estimating the overall multiplicity of events, as well as for triggering purposes. Their asymmetric position in rapidity space is used with the timing of the two signals to trigger only on events that occurred within the center of the detector, rather than on peripheral beam-gas interactions[78]. In addition, as discussed in section 1.4.2, the measured activity in these forward and backward regions can be correlated with the multiplicity in the central pseudorapidity range. This allows for the separation of events into groups of similar multiplicity, and therefore similar collision system size.

2.2.5 EMCAL & DCAL

The EMCAL is a large lead scintillating calorimeter. Positioned at the outside of the ALICE central barrel, it covers a pseudorapidity range of $|\eta| < 0.7$ and roughly a third of the azimuthal range ($\Delta\varphi = 100\,\text{deg}$) [79]. The Di-jet Calorimeter (DCAL) is an identically built detector installed on the opposite side of the central barrel ($\Delta\varphi = 60\,\text{deg}$) for LHC Run 2 [80]. The DCAL is designed to capture back-to-back jet signals by expanding the ALICE calorimetry coverage.

The design of the two detectors are identical, consisting of individual calorimetry cells made up of 77 alternating layers of lead and scintillator tiles, leading to an array of optical fibers for signal readout. These individual cells are grouped together into modules, and then further into larger structures called supermodules. Within a supermodule, modules slightly change in orientation in the direction of increasing

rapidity. This allows each cell to cover the same area in ϕ and η ($\Delta\varphi \times \Delta\eta = 0.0143 \times 0.0143$) (see fig. 2.5). Each supermodule then sends its signal to its own Readout Control Units (RCU), which sends the data to be written to storage.

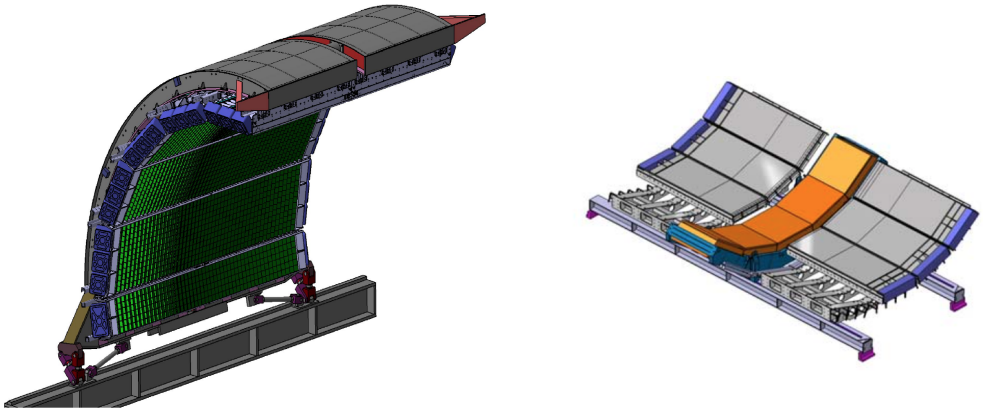

Figure 2.5: Schematic drawing of the ALICE EMCAL (left) [79] and DCAL (right) [80]. For LHC Run 2, both the EMCAL and DCAL were installed and operational, providing a large azimuthal coverage for better di-jet reconstruction.

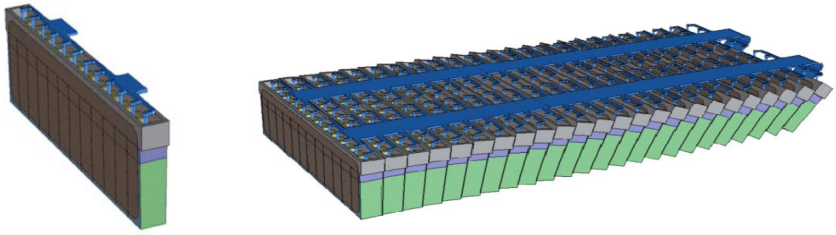

Figure 2.6: An example of an individual EMCAL module (left) and supermodule (right) [81].

2.2.6 Calibration for the EMCAL & DCAL

As part of the data processing and collection steps, the measurements coming from the detectors and sub-detector components of ALICE must be properly calibrated. The execution of timing calibration for the EMCAL and DCAL detectors was performed as part of specific service work requirements to become a member of the ALICE

collaboration. In addition to the service work of performing the established calibration procedure, additional new techniques were developed to allow for the successful calibration and recovery of run data previously considered as "bad."

2.2.6.1 Timing Calibration

In order to exclude any signals within the EMCAL and DCAL that may originate from pile-up collisions (i.e. nearby collisions that happened directly before or after the main, triggered collision), the time signal from the EMCAL must be precisely calibrated. As the pp interaction rate during Run2 of the LHC was 40 MHz, in order to exclude pileup events, a cut of less than $\pm$ 25 ns is needed around the primary collision, and therefore a timing calibration is necessary so that each cell of the EMCAL is aligned to the same primary interaction timing.

Due mostly to the length of wire connecting each cell to the readout unit and the signal processing time, the time signal of the EMCAL is offset from the interaction time by $\approx$ 600 ns. However, as a cell's position within a given supermodule (SM) effects the length of readout wire (as well as differences in readout time) a timing offset must be found for each individual cell. After this offset is found and removed, each EMCAL cell has a time signal that aligns with the initial collision corresponding to t = 0 ns, allowing for tight cuts to exclude pileup events.

To perform this calibration, we must first select all EMCAL signals that are likely to have come from the initial collision. For this, the EMCAL signals for the timing calibration are required to have high cluster and cell energy requirements, as these high energy signals have a tighter time spread. A sample of these signals can be seen in figure 2.7 for each cell, where each SM can be seen to have a different distinct distribution and average.

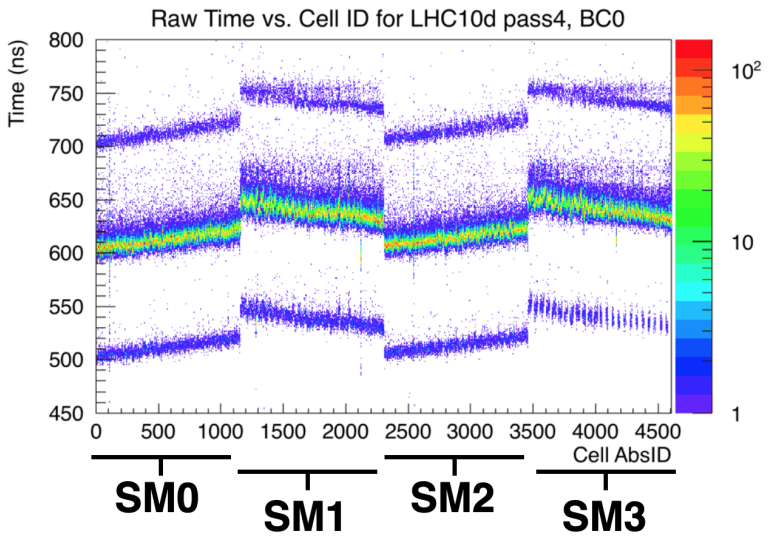

Figure 2.7: Example 2D plot of the raw timing information of each EMCAL signal for each cell in a subset of the full detector. The dense band at ≈ 600 ns corresponds to main collision events, while the lighter bands correspond to pileup events. The slope of the main band within each SM is due to the difference in readout wire length due to the position of a cell within the module.

Since the timing calibration offset is predominantly a function of the specific configuration of the detector's hardware and software, it is generally a stable value across multiple run periods as long as the detector remains unchanged. Nevertheless, the timing offset per cell is found for each run period separately as an initial pass. Afterwards, run periods with similar configurations - and therefore similar timing offsets - can be combined together to calculate a single overarching offset, giving greater timing resolution than the individual run periods on their own.

2.2.6.2 L1 Phase Correction

Complicating the time calibration procedure is a mismatch between the clock frequency of the EMCAL supermodules' readout window (10 MHz) and the LHC collision frequency (40 MHz). This mismatch in clock frequencies leads to a distinct

structure of 4 primary interaction peaks in the raw time distribution (fig. 2.8). To correct for this, a "phase" within the 100 ns SM clock window, referred to as the L1 phase, must first be accounted for in order to properly calculate the time offset. Before the L1 phase correction is applied, there is a separate peak structure for interactions depending on the mismatch between the LHC collision frequency and the DCAL clock readout window, creating four distinct peaks separated by 25 ns in the raw time distribution. Once the correct L1 phase is found, all collision data can be combined to produce a single time distribution peak for the main interaction, and the pileup signals can be cleanly removed.

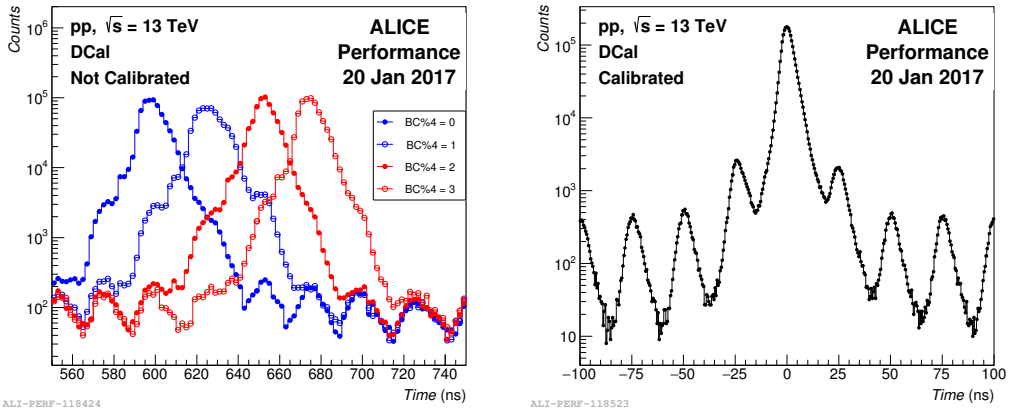

Figure 2.8: An Example of the effect of the L1 phase mismatch on the raw time signal of the DCAL (left), and the L1 phase and offset corrected time distribution (right). In both plots, the distribution of time signals for only a specific supermodule (SM 19) within the DCAL is shown.

To find the L1 phase of each SM, the EMCAL data is separated into four collections based on the collision Bunch Crossing (BC) number of the interaction modulo 4 (see fig 2.9). This separates out events based on where within the 100 ns window these events took place in steps of 25 ns (the time between pp collisions). We then find, for each SM, which of these four data collections has the lowest value for the mean interaction time, and the L1 phase correction is set to this particular BC(mod 4)

value. Once the L1 phase is found, the EMCAL timing data is corrected to show a single peak for the main interaction time, and the time calibration procedure can continue.

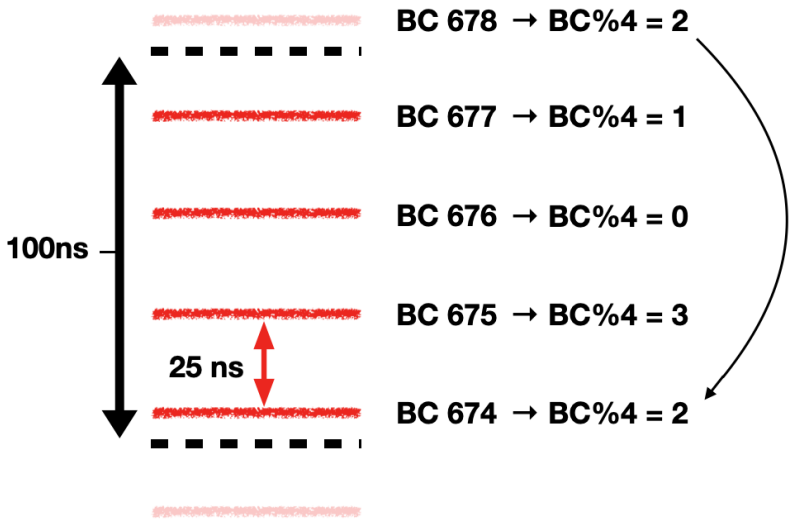

Figure 2.9: Diagram showing the effect of the frequency mismatch between the LHC and EMCAL readout clock. The 100 ns EMCAL readout clock period is depicted between the dashed lines, while the rough timing of individual pp collisions is depicted in red. For any given interaction in the ALICE detector, the bunch crossing number of the interaction modulo 4 gives where that interaction will occur in the EMCAL readout clock. The ability to separate out events in this way is crucial to being able to calibrate the time of the EMCAL signal.

2.2.6.3 Full Time Correction

Putting together the entire time calibration procedure, the following process is required for each Run Period:

1. Calculate the **L1 phase** for each SM, giving a phase correction of 0, 1, 2, or 3.

2. Using the L1 phase correction, calculate the average time for each cell using a large 400 ns window around a central value of 600 ns. This gives a first **rough time offset**.

3. Using the L1 phase and rough time offset, calculate the average time of each cell with a small 20 ns window centered at 0 ns to get a **final time offset**.

4. After quality checks, the L1 phase correction and final time offset are uploaded to the Offline Analysis Database (OADB) for the given run period.

While the final time offset should be the same for each period (unless the EMCAL detector has been modified between periods), the time calibration procedure is still performed separately for each run period in order to assure quality of the final time distribution. Once specific periods are shown to have well resolved time distributions (and therefore well resolved time offsets), they can be combined to increase the accuracy of the final time offset.

2.2.6.4 Pause & Reset Runs and Phase Alignment

When a data taking run in ALICE is ongoing, it will occasionally happen that a subdetector will malfunction and require a hard reset in order to continue to collect data. To avoid having to fully stop and start a new run of data collection each time one of these malfunctions happens, ALICE allows the option to perform a Pause & Reset (PAR) procedure. This allows for the reset of a specific detector subsystem without interrupting the entire run.

While this PAR procedure is useful for efficient data collection, it has an unintended consequence for the EMCAL: each time a PAR is performed, it will cause the EMCAL L1 phase to be reset across all SMs. This means that instead of having a single L1 phase correction, runs where a PAR occurred require multiple L1 phase corrections for data collected before and after each PAR in order to be calibrated (i.e. each run requires $N_{par} + 1$ phase corrections for each SM). Due to the way the time correction had been previously performed, the initial collision timing distribution is

then split from a single peak into multiple peaks (see fig. 2.10). This leads to no longer being able to separate the main collision from the pileup events, and these runs were thus considered bad runs and rejected for EMCAL analyses.

In order to maximize the amount of data available for EMCAL analyses, it was necessary to update the calibration procedure to allow for the recovery of these otherwise good PAR events. This requires a way to separate the PAR runs into data collected before and after each PAR, as each of these periods would require a separate L1 phase correction. This also requires a new way to store and retrieve this PAR information in order to perform the actual timing calibration and fully recover these runs for data analysis.

To identify the exact time when a PAR occurred in relation to the a given run, a unique timing identifier is given to each PAR event, computed as:

$$(\text{PAR ID}) = BC + O * 3564 + P * 597793994260$$

where BC is the bunch crossing number, O is the orbit, and P is the period where the PAR event occurred. By reading a list of all the unique times a PAR occurred during a specific run, collisions can be separated into timing distributions based on which PAR event they were before or after. These time distributions can then be fit separately for the L1 phase. Once these separate L1 phases are found, they are stored and applied before the rest of the calibration steps occur. This enables the full run to be used for the time calibration, giving a good time resolution for the final per-cell timing offset even in previously bad PAR runs. To allow these formerly bad runs to be used by analyzers, the calibration database was updated to include the unique PAR ID within the name of the L1 phase objects, allowing for on-the-fly calibration to be applied as needed for EMCAL and DCAL analyses.

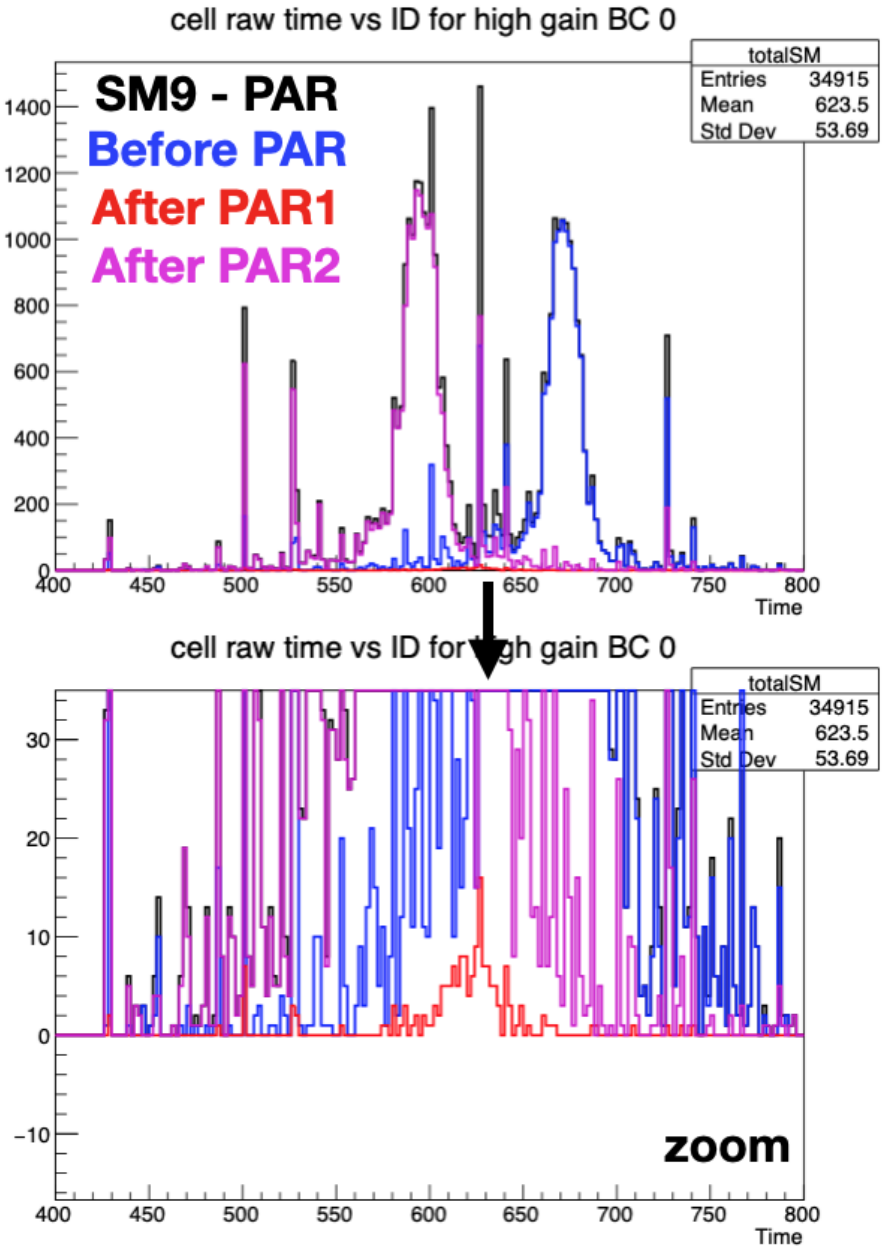

Figure 2.10: Example of the timing distribution for a single SM (SM9) during a run with multiple PARs. Each PAR here has reset the L1 phase, leading to distinct peaks for before and after the time when each PAR occurred. (bottom) A zoomed portion of the top plot to show the third peak structure, which is smaller due to the smaller number of collisions that occurred between when PAR 1 and PAR 2 were executed.

Chapter Three: Measuring Production of $\phi(1020)$ In p-Pb Collisions: How and Why

Finally, after establishing all the necessary theoretical frameworks and experimental history, it is possible to delve into the main topic of this dissertation: **Investigating the onset of strangeness enhancement using $\phi(1020)$ meson production in p-Pb collisions.** The goal of this work is to look for the origin of strangeness enhancement via different production processes within small collision systems. In order for a study to accomplish this, it would need to:

1. Separate strange particles from non-strange particles.
2. Separate out particles produced in hard scattering processes (i.e. jets) from those produced in softer processes, which would include production within a QGP phase.
3. Be performed across a range of intermediate event multiplicities to study the emergence of this behavior.

To the first point, the $\phi(1020)$ meson was selected for this analysis as a useful strange probe (see sec. 3). Comparing the production of the $\phi(1020)$ to inclusive charged hadrons provides a way to study strangeness production with respect to a non-strange baseline. To the second point, performing jet-like angular correlations can separate out particles that are associated with a jet (more hard scattering-like) from those that are not associated with a jet (more soft scattering-like).

And finally, p-Pb collisions measured at ALICE provide enough data to perform this measurement for several different multiplicity ranges, allowing for a look at $\phi(1020)$ production as a function of increasing system size. Putting all of this together gives a novel way to look at strangeness via $\phi(1020)$ production within small systems by using two particle angular correlations.

3.1 The $\phi(1020)$ Resonance as Strangeness Probe

The $\phi(1020)$ meson ($s\overline{s}$) is a resonance particle, and therefore decays via the strong force within a very short lifetime. However, this lifetime ($\approx 45\,\mathrm{fm/c}$) is longer than other strange resonance particles, such as the K^*. By virtue of this longer lifetime, ϕ produced early on in the collision can survive the entire collision evolution, specifically the hadronic gas phase that occurs after the QGP phase and before the final kinetic freeze-out. Lasting for $\approx 1\,\mathrm{fm/c}$ in p-Pb collisions ($\approx 0.5 - 10\,\mathrm{fm/c}$ for PbPb collisions), the hadronic gas phase is where rescattering and regeneration effects can act to enhance or suppress measured resonance production, respectively (see figure 3.1)[82], [83]. By living through the entire collision evolution before decaying, ϕ yield measurements are not notably changed by these two effects [84].

While the $\phi(1020)$ meson contains zero net strangeness itself (being composed of one strange quark and one strange anti-quark, for a total strangeness S=0), it still requires a strange quark anti-quark pair to be created within the collision in order to form. Since strangeness enhancement is seen to increase with the net strangeness of a particle species, by comparing the $\phi(1020)$ meson production with other strange particles, it is seen that the $\phi(1020)$ experiences enhancement similar to a particle with net strangeness S between 1 and 2 [85]. This enhancement is observed across many different collisions systems, and is dependent only on event multiplicity (see

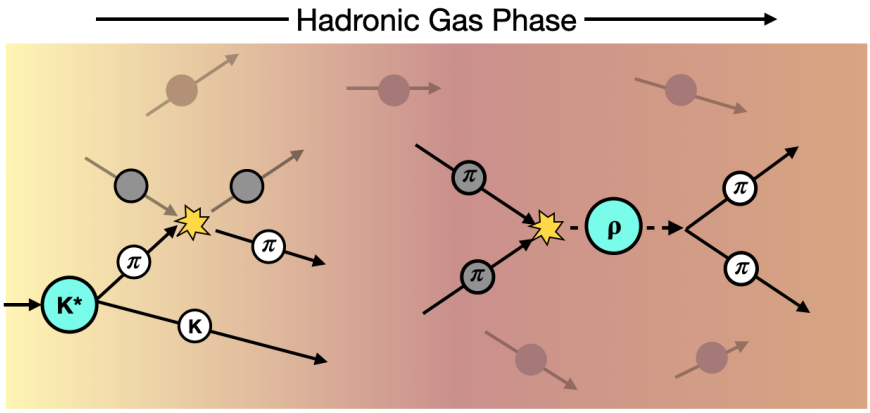

Figure 3.1: Cartoon depicting rescattering and regeneration processes in the hadronic gas that can effect the measured yields of resonances in heavy ion collisions. The left interaction shows a rescattering process, where one of the K^* decay particles elastically scatters off another hadron in the gas, destroying the invariant mass correlation between the two child particles of the K^*. The right interaction shows a regeneration process, where two pions scatter through a $\rho(770)$ resonance state, before decaying again to two pions. This will increase the measured production of the ρ meson by adding a resonance that was produced after the initial collision/deconfinement phase occurred.

figure 3.2). With these properties in mind, the $\phi(1020)$ is a useful probe for studying strangeness enhancement with little "contamination" from other physical effects on the measured production.

3.2 Two-Particle Correlations

Given some property θ of interest to be measured in a collision experiment, it is often useful to study the correlation between θ measured for a "trigger" particle X and for an "associated" particle Y. Here, the requirements for a particle to be considered a "trigger" or "associate" can be any of a number of different properties (particle species, momentum, energy, etc.), or they may have no requirements at all. If the measurement is carried out over an ensemble of many collisions, and the measured

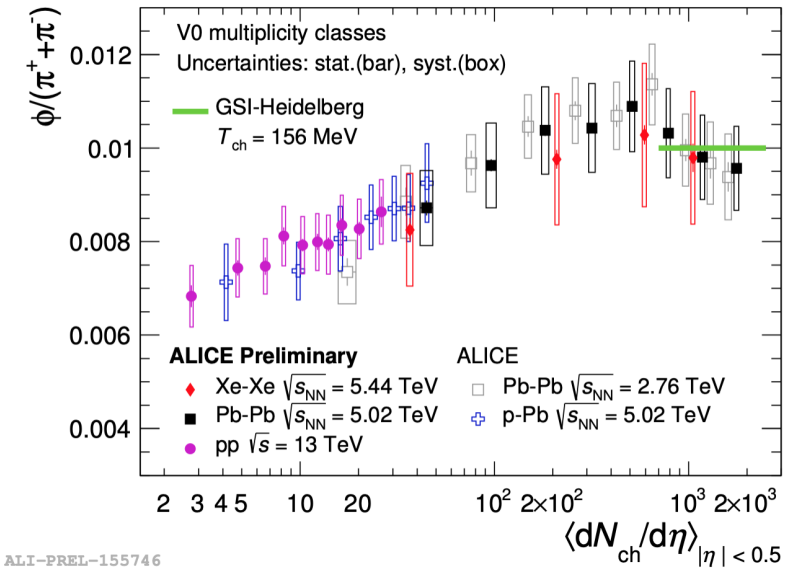

Figure 3.2: The momentum integrated ϕ/π ratio plotted as a function of event charged particle multiplicity. This ratio increases smoothly across a wide range of multiplicities, with no dependence on the specific collision system studied.

value of θ is binned in a histogram with bins of finite width, then the number of counts in bin i for particle X can be thought of as a random Poisson variable $\theta_{i,X}$. In other words, the number of times that a particle X is measured with property θ in bin i in the ensemble is now the random variable of interest. This allows for the use of the standard Pearson's correlation coefficient between the count for particle X in one bin, and the count for particle Y in another bin:

$$corr(\theta_{i,X}, \theta_{j,Y}) = \frac{cov(\theta_{i,X}, \theta_{j,Y})}{\sigma_{\theta_{i,X}} \sigma_{\theta_{j,Y}}}, \tag{3.1}$$

where the numerator is the covariance of the joint probability distribution for counts in bin i for particle X and bin j for particle Y, and the denominator is the product of the standard deviations of the single particle, single bin distributions [86]. Pearson's correlation coefficient measures the linear correlation between the two variables, varying between a value of 1 (perfectly correlated) and -1 (perfectly anti-

correlated). In this application, the correlation coefficient answers the question "If more X particles with properties θ_i are measured, would the number of Y particles with property θ_j be expected to rise or fall, or are the counts in these two bins for the two particles not linearly correlated?" The covariance is defined as:

$$\begin{aligned} cov(\theta_{i,X}, \theta_{j,Y}) &\equiv \langle \theta_{i,X} - \langle \theta_{i,X} \rangle \rangle \langle \theta_{j,Y} - \langle \theta_{j,Y} \rangle \rangle \\ &= \langle \theta_{i,X} \theta_{j,Y} \rangle - \langle \theta_{i,X} \rangle \langle \theta_{j,Y} \rangle, \end{aligned}$$

with $\langle\rangle$ denoting the average value over the ensemble of events.

The histogram bin counts are assumed to follow a Poisson distribution over the large number of events in the ensemble. Thus, one can use the fact that $\sigma^2_{\theta_i} = \langle \theta_i \rangle$ (i.e. the variance is equal to the mean number of entries in bin i) for Poisson random variables to re-write the full correlation function as:

$$\begin{aligned} corr(\theta_{i,X}, \theta_{j,Y}) =& \frac{\langle \theta_{i,X} \theta_{j,Y} \rangle - \langle \theta_{i,X} \rangle \langle \theta_{j,Y} \rangle}{\sqrt{\langle \theta_{i,X} \rangle \langle \theta_{j,Y} \rangle}} \\ =& \sqrt{\langle \theta_{i,X} \rangle \langle \theta_{j,Y} \rangle} \left(\frac{\langle \theta_{i,X} \theta_{j,Y} \rangle}{\langle \theta_{i,X} \rangle \langle \theta_{j,Y} \rangle} - 1 \right) \end{aligned}$$

Next, it is noted that the expected number of counts in bin $\theta_{i,X}$ is the same as the probability of particle X having a θ value in bin i in a single event, multiplied by the total number of X particles N_X in the sample of events. This then lets all the expected bin counts to be re-written in terms of the probability function of the underlying variable, i.e. $\langle \theta_{i,X} \rangle = N_X P_X(\theta_i)$ and $\langle \theta_{i,X} \theta_{j,Y} \rangle = N_X N_Y P_{X,Y}(\theta_{i,x}, \theta_{j,Y})$. In practice, the correlation ratio is often simplified and presented without the initial pre-factor and -1, leaving:

$$C(\theta_{i,X}, \theta_{j,Y}) = \frac{P_{X,Y}(\theta_{i,X}, \theta_{j,Y})}{P_X(\theta_i) P_Y(\theta_j)} \tag{3.2}$$

3.2.1 Jet-like Two Dimensional Angular Correlations

From the derivation in the previous section, a two particle correlation function in 2-D angular space can be written as:

$$C(\varphi_t, \eta_t, \varphi_a, \eta_a) = \frac{P_{t,a}(\varphi_t, \eta_t, \varphi_a, \eta_a)}{P_t(\varphi_t, \eta_t) P_a(\varphi_a, \eta_a)},$$

where $P_{t,a}$ is the joint probability distribution of angular measurements (φ_t, η_t) of the trigger particle and angular measurements (φ_a, η_a) of the associated particle, and P_t and P_a are the single particle probability distributions.

For the purpose of this analysis, the "trigger" particle is always a high momentum hadron. When their transverse momentum is over $4\,\mathrm{GeV/c}$, high p_T hadrons are closely aligned with the center of a jet-axis (found using jet reconstruction methods such as the k_T or anti-k_T algorithms)[87]. This means that choosing a high momentum hadron as the trigger will give a good approximation of the correlation between jets and the measured associate particles, while also including hard scattering processes that may be missed when considering full jet reconstruction algorithms.

Symmetries inherent in the experimental setup can help simplify this correlation function. First, the four single-particle random variables $(\varphi_t, \eta_t, \varphi_a, \eta_a)$ can be transformed to two sum variables $(\Sigma\varphi, \Sigma\eta)$ and two difference variables $(\Delta\varphi, \Delta\eta)$. These are defined as $\Sigma\varphi \equiv \varphi_t + \varphi_a$ and $\Delta\varphi \equiv \varphi_t - \varphi_a$ (and likewise for η). Since experimentally the collisions must, on average, be symmetric in azimuth (due to the initial beam energy being entirely in the longitudinal direction), the correlation function should not depend on the sum variable $\Sigma\varphi$. Likewise, because experimentally measured particle production is roughly constant in the central η range (and therefore the physics of the collision should not depend on η in this central region) the correlation should not depend on the sum variable $\Sigma\eta$[1]. This argument that the correlation does

[1]These symmetry arguments are essentially equivalent to the criteria for a stochastic process to

not depend on the sum variables has also been experimentally verified [88], [90]. This then allows the four variable correlation to be reduced to two variables $(\Delta\varphi, \Delta\eta)$, without losing any physics information.

Using this simplification, an experimental correlation function using the difference variables can be approximated as:

$$C(\Delta\varphi, \Delta\eta) \approx \frac{S(\Delta\varphi, \Delta\eta)}{ME(\Delta\varphi, \Delta\eta} \tag{3.3}$$

here, $S(\Delta\varphi, \Delta\eta) = \frac{d^2N_{\text{pair}}}{d\Delta\varphi d\Delta\eta}$ is the distribution for trigger-associate pairs from the same event, which is equivalent to the joint probability distribution. The term $ME(\Delta\varphi, \Delta\eta)$ is the mixed-event correlation, and is constructed by taking trigger and associated particles from different events, which then acts analogously to the product of the single particle distributions [91].

This experimental form of the correlation measure can be re-scaled slightly to give a new quantity, the per-trigger correlation function:

$$C_{\text{trig}}(\Delta\varphi, \Delta\eta) \equiv \frac{1}{N_{trig}^{corr}} \frac{1}{\varepsilon_{trig} * \varepsilon_{assoc}} \frac{ME(0,0) * S(\Delta\varphi, \Delta\eta)}{ME(\Delta\varphi, \Delta\eta)}, \tag{3.4}$$

where N_{trig}^{corr} is the efficiency corrected total number of trigger particles and ε are the single particle efficiencies*acceptances [92]–[94]. Here, the mixed-event distribution acts as correction factor for the two-particle acceptance of the detector. The additional scaling factor, $ME(0,0)$, acts to scale the mixed-event distribution such that the scaled mixed-event correlation is equal to 1 for trigger and associate particles that are in identical directions [95].

This per-trigger correlation function contains roughly the same information as the original Pearson's correlation coefficient. However, rather than giving a correlation

be considered "stationary", and therefore for the autocorrelation function of the process at time t_1 and t_2 to only depend on the difference $\tau = t_1 - t_2$ [88], [89].

coefficient between 1 and -1, this formulation of the correlation function gives the number of correlated trigger-associate pairs per trigger particle in a given $\Delta\varphi, \Delta\eta$ bin. This is approximately equivalent to the **number of associated particles produced per trigger particle** within events that contain a trigger (see section 5.2.1 for more detail on this point). The correlation function then acts as a way to measure the associate particle yields in relation to the trigger particle - in the case of this dissertation, yields of $\phi(1020)$ mesons inside or outside of a jet.

3.2.2 Mixed Event Correlations

With this simplified version of the angular correlation function, there are two main measurements needed: the same event correlation and the mixed-event correlation (see fig. 3.3). For each event in the ensemble, the same-event correlation, $S(\Delta\varphi, \Delta\eta)$, is filled by finding a trigger particle and measuring the relative angles between it and all associated particles in the same collision event. The mixed-event correlation, $ME(\Delta\varphi, \Delta\eta)$, is constructed by correlating trigger and associated particles from separate events, giving an approximation of the product of the single particle probabilities in the denominator of the correlation function. In order for this approximation to hold, the mixing of events must be between two relatively similar events. For this reason, the mixing occurs in three different multiplicity bins, and is also separated into mixing pools based on the location of the primary collision vertex within the detector.

An example of a two dimensional same event and mixed event correlation can be seen in figure 3.4. The characteristic triangular shape in the $\Delta\eta$ direction is explained by the finite acceptance of the detector in η. In general, if two independent random variables X and Y have a uniform probability distribution, then the variable $Z =$

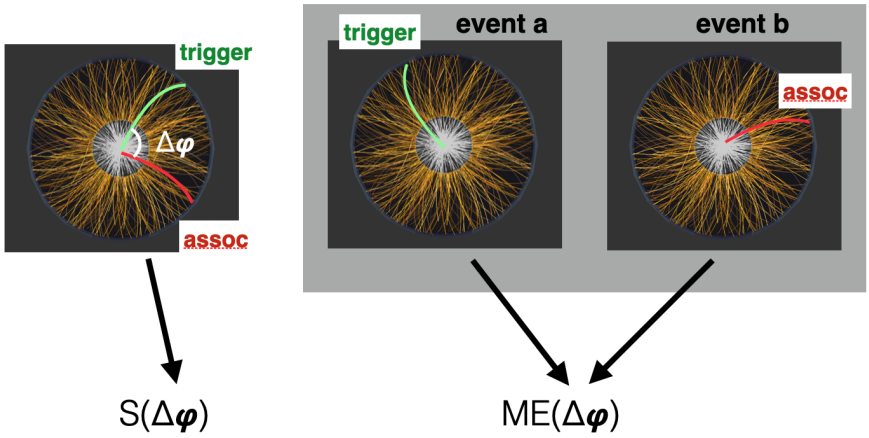

Figure 3.3: Cartoon schematic showing the construction of same-event and mixed-event correlations for simple 1D angular correlations. The yellow tracks are the produced particles within a single collision, while the green and red tracks are the trigger and associate particle, respectively.

$X - Y$ will have a triangular probability distribution of the form $P(Z) = a|Z + b| + c$ for some constants a, b, and c. As particle production in the collisions is roughly uniform across the central η region (and the trigger and associate particles must be independent of each other in the mixed event case by definition), the difference, $\Delta\eta$, is dominated by this triangular expression. Dividing the same event by the mixed event distribution then removes this finite detector effect. Normalizing the mixed-event distribution by its value at $ME(0, 0)$ ensures that the two particle acceptance effect is equal to 1 when the trigger and associate particle are going in the same direction. This must be true by definition, since there cannot be a two-particle detector acceptance effect if both particles are traveling in the same direction: either they're both in the acceptance, or neither is.

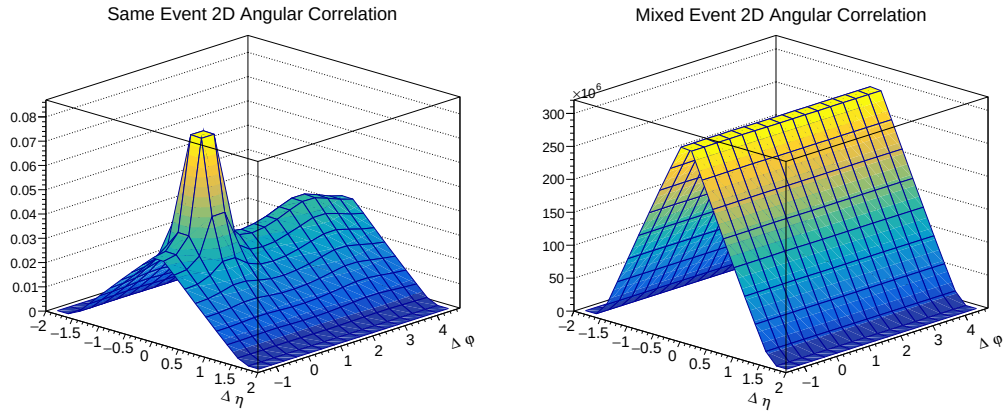

Figure 3.4: An example of a two dimensional angular correlation $(\Delta\eta, \Delta\varphi)$ for trigger and associated particles from the same event (left) and from different, mixed events (right). The same-event correlation contains both physical correlation structures (e.g. the peak around $(\Delta\eta, \Delta\varphi) = (0, 0)$), as well as effects from the finite detector size. The mixed-event correlation should only contain the detector acceptance effects (e.g. the triangular distribution in $\Delta\eta$), and is therefore used to correct for these effects in the same-event correlation.

3.3 Measuring $h - \phi$ Angular Correlations

Since the ϕ meson decays well before entering the ALICE detector, it must be reconstructed from its decay children particles. For this analysis, the ϕ is reconstructed from the $\phi \to K^+K^-$ decay channel (B.R. 49%)[19]. This reconstruction is performed by taking all unlike-sign (US) K^+K^- pairs in the event and computing the invariant mass and momentum of the parent particle assuming the pair came from a single decay. That is, the parent invariant mass can be calculated as:

$$m_{KK} = \sqrt{(E_{K_1} + E_{K_2})^2 - |\vec{p}_{K_1} + \vec{p}_{K_2}|^2} \tag{3.5}$$

where the energy of each of the kaon candidates is calculated assuming the particle has the mass of a kaon (i.e. $E_{K_1} = \sqrt{m_K^2 + |p_{K_1}|^2}$). The invariant mass distribution can then be used to find those pairs that fall within the mass peak of the ϕ meson (fig. 3.5). However, some random combinations of unlike-sign kaon pairs will fall into

the ϕ mass peak range even if they didn't decay from a ϕ. In order to successfully reconstruct the number of $\phi(1020)$ mesons produced, these random pairs, known as the combinatorial background, must be removed. To do this, the invariant mass of like-sign (LS) kaon pairs (which will not contain the ϕ decay peak) is used as a background estimate. The LS distribution must then be scaled to the same value as the US distribution in the sideband regions (i.e. far away from the ϕ mass peak) to accurately capture the combinatorial background. The scale factor, k_{LS} is defined as the yield in the left and right sidebands in the unlike-sign distribution, divided by the same yields in the like-sign distribution.

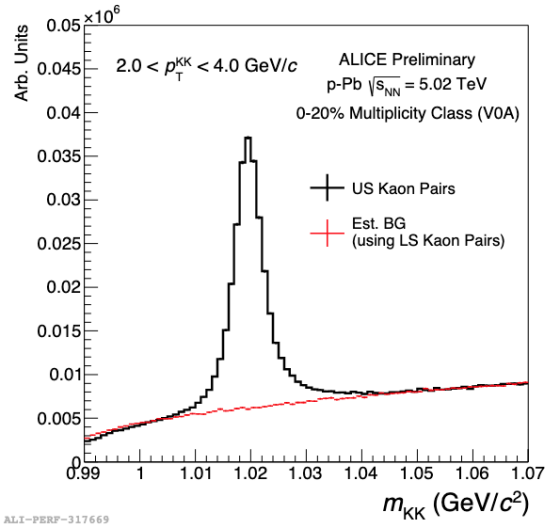

Figure 3.5: The calculated invariant mass of unlike-sign kaon pairs(black), and an estimate of the combinatorial background (red) using the scaled mass distribution of like-sign kaon pairs. The excess at a mass of $1020\,\mathrm{MeV/c^2}$ is the ϕ invariant mass peak.

The combinatorial background subtraction is tested by fitting the resulting BG-subtracted invariant mass distribution to a Voigtian function (a Gaussian convoluted with a relativistic Breit-Wigner distribution)[96] plus a polynomial term to capture residual background (see fig. 3.6). For the momentum ranges considered in this

analysis, the like-sign background subtraction leaves a residual background under the $\phi(1020)$ mass peak of less than 1% of the total $\phi(1020)$ signal. In addition, the ϕ mass peak region used in this analysis ($1.014 < m_{KK} < 1.026\,\mathrm{GeV/c^2}$) doesn't capture the entire mass distribution, so an additional factor is needed to correct for the missing distribution tails. This factor, k_{Signal}, is computed from the Voigt fit function of the like-sign subtracted mass distribution. By dividing the integral of the Voigt fit in the mass peak region by the integral across the entire mass space, the mass peak region is found to capture $\sim 80\%$ of the reconstructed ϕ mesons, giving a correction factor of $k_{\mathrm{Signal}} = 1/0.8$.

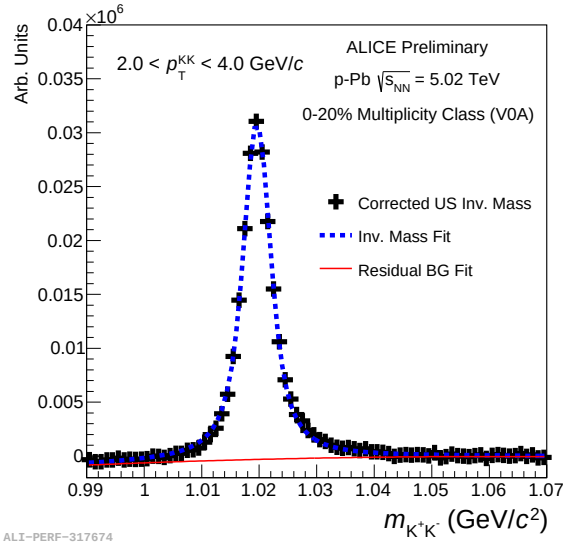

Figure 3.6: The unlike-sign invariant mass distribution after subtracting off combinatorial background, estimated using the scaled like-sign distribution. The mass peak is fit to a Voigt function for the mass peak, and an additional polynomial for the residual background (red). The residual background is $< 1\%$ of the signal, and for this analysis is ignored.

3.3.1 Reconstructing the $\phi(1020)$ for Angular Correlations

To reconstruct the ϕ for the angular correlations, the correlation measurement $(h - KK)$ is performed for three different US kaon-pair invariant mass regions: the ϕ mass peak region ($1.014 < m_{KK} < 1.026\,\mathrm{GeV/c^2}$), the left sideband region (LSB) ($0.995 < m_{KK} < 1.005\,\mathrm{GeV/c^2}$), and the right sideband region (RSB) ($1.040 < m_{KK} < 1.060\,\mathrm{GeV/c^2}$). The correlations in the two sideband regions are averaged together and used to estimate the shape of the distribution produced by correlating the trigger hadron with a combinatorial kaon pair (see fig. 3.7). By integrating the Voigtian fit, the unlike-sign kaon pairs in the sideband regions are calculated to contain much less than 1% ϕ decay kaon pairs.

Taking into account these additional terms for the reconstruction process, the final per-trigger $(h - \phi)$ correlation function is given as:

$$C_{h-\phi}(\Delta\varphi, \Delta\eta) = k_{\mathrm{Signal}}\Bigg(C_{\mathrm{trig}}^{h-(KK)\ \mathrm{Peak}}(\Delta\varphi, \Delta\eta) - \frac{k_{LS}}{2} * \left[\frac{1}{N_{Ent}^{LSB}} C_{\mathrm{trig}}^{h-(KK)\ \mathrm{LSB}}(\Delta\varphi, \Delta\eta) + \frac{1}{N_{Ent}^{RSB}} C_{\mathrm{trig}}^{h-(KK)\ \mathrm{RSB}}(\Delta\varphi, \Delta\eta) \right] \Bigg), \tag{3.6}$$

with the three different C_{trig} functions defined by eq. 3.4 for the three different collections of K^+K^- pairs (the ϕ mass peak, the left sideband, and the right sideband regions).

3.3.2 Jet and Underlying Event Yields

Once the two dimensional angular correlation is computed, for statistical considerations the correlation function is projected onto the single $\Delta\varphi$ axis (see fig. 3.8). While this does cause some loss of information in the $\Delta\eta$ direction (i.e. the near side jet is better captured with a cut in both $\Delta\eta$ and $\Delta\varphi$), the decrease in statistical

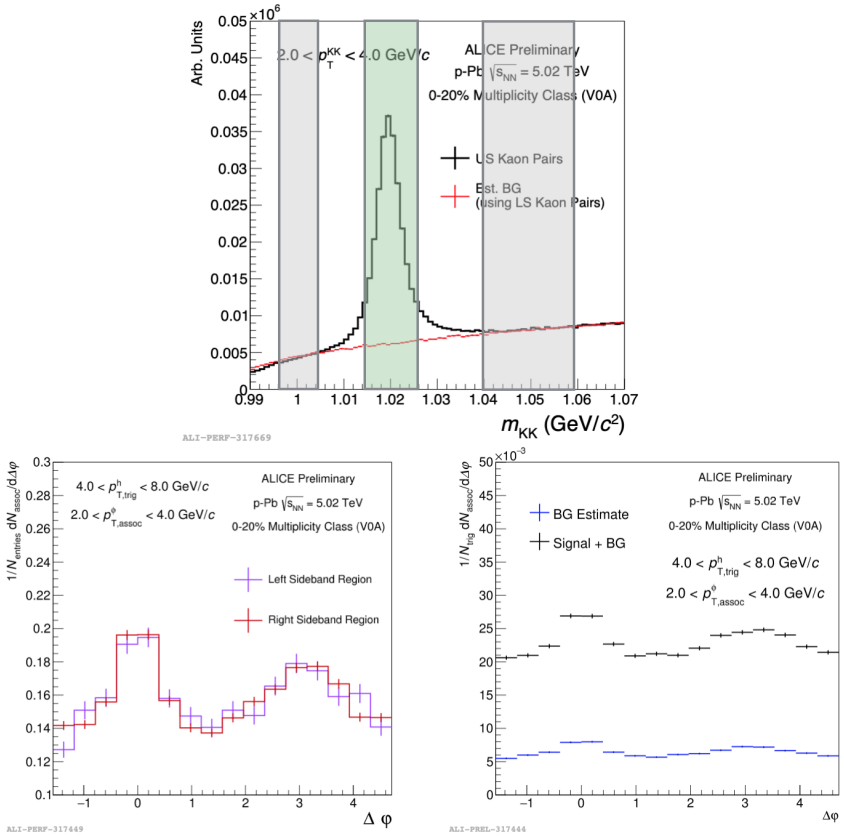

Figure 3.7: A depiction of the (one dimensional) angular correlations from the three different KK invariant mass regions: the correlation from the left and right sidebands (lower left), and the correlation from the mass peak region (lower right). The invariant mass distribution (top) shows the different ranges of the sideband regions (gray) and mass peak region (green). In the mass peak region correlation, both the full correlation is presented, as well as the background correlation from the combinatorial KK background laying underneath the mass peak (calculated as the average of the two sideband correlations).

fluctuations in the 1D correlation allows for a better distinction between the jet peaks and the uncorrelated background.

The now one-dimensional angular correlation is divided up into three different regions to calculate the yields of correlated pairs: the near-side jet, the away-side jet, and the underlying event (see fig. 3.9). In order to separate the jet peaks from the underlying event, a flat background estimate is used by computing the average over

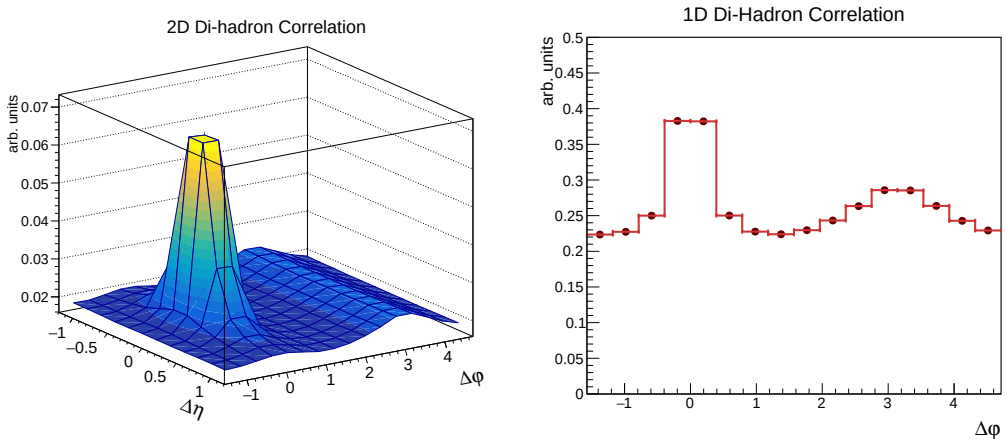

Figure 3.8: Example plot showing the result of projecting a 2D angular correlation (left) onto the $\Delta\varphi$ axis from the range $|\Delta\eta| < 1.2$ to produce a 1D angular correlation (right).

the region away from the two jet peaks ($-\pi/2 < \Delta\varphi < -\pi/4$, $\pi/4 < \Delta\varphi < 5\pi/8$, and $11\pi/8 < \Delta\varphi < 3\pi/2$). This flat background assumption is equivalent to a two-source model, where produced particles are either produced in jets or in the underlying event, and the two regions are uncorrelated with each other [97]. The near-side yield is then defined as the area above this background in the region $-\pi/2 < \Delta\varphi < \pi/2$. Similarly, the away-side yield is defined as the area above the background in the region $\pi/2 < \Delta\varphi < 3\pi/2$. The underlying event yield is computed as the area underneath this flat background across the whole angular range (more detail on the underlying event estimation is provided in section 5.2.3).

Since the correlation function gives the per-trigger pair-wise counts ($\frac{1}{N_{trig}}\frac{d^2N_{\text{pair}}}{d\Delta\varphi d\Delta\eta}$), if events only contain one trigger particle on average, then these pair-wise yields are approximately equal to the per-trigger single particle yields (i.e. the integral over the entire correlation is $\approx \frac{1}{N_{trig}}N_\phi$) (see section 5.2.1 for more details on this point). In this way, the one-dimensional $(h-\phi)$ angular correlation allows for the measurement of the per-trigger $\phi(1020)$ yields inside and outside of jets.

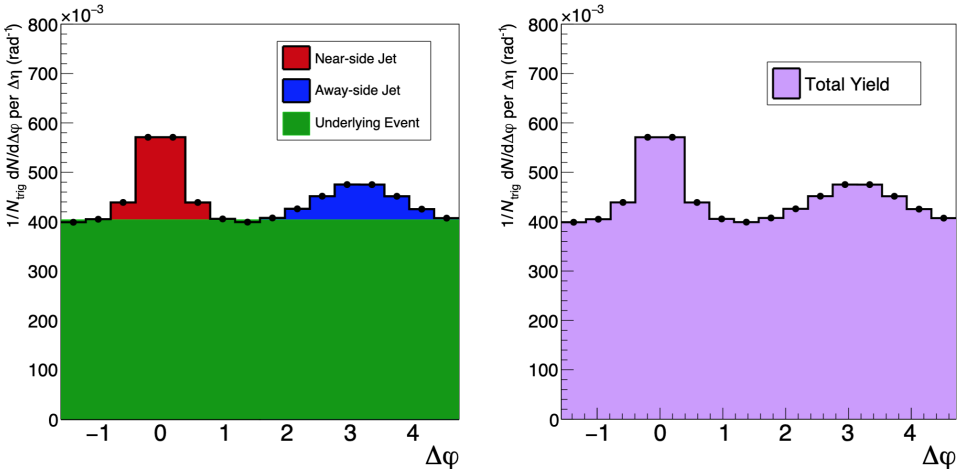

Figure 3.9: Example plot depicting the different regions of a dihadron angular correlation: the near-side jet (red), the away-side jet (blue), the underlying event (green), and the total pair yields (pink).

3.4 Measuring Dihadron Angular Correlations

Since the end goal of this analysis is to study strangeness enhancement through changes to the ϕ/h production ratio, additional $(h-h)$ correlations are needed to provide the non-strange baseline. For this purpose, dihadron correlation measurements are taken using inclusive charged hadrons as the associate particle. Because there is no additional reconstruction step for the inclusive hadrons, this per-trigger correlation function is given exactly by equation 3.4:

$$C_{h-h}(\Delta\varphi, \Delta\eta) \equiv \frac{1}{N_{trig}^{corr}} \frac{1}{\varepsilon_{trig} * \varepsilon_{assoc}} \frac{ME(0,0) * S(\Delta\varphi, \Delta\eta)}{ME(\Delta\varphi, \Delta\eta)}. \tag{3.7}$$

The dihadron same-event correlations are corrected for the two-particle detector acceptance by the mixed-event correlation in the same way that the $(h-\phi)$ correlations were. The dihadron correlations then go through the exact same yield extraction procedure as the $(h-\phi)$, where the correlations are projected onto the $\Delta\varphi$ axis and

divided up into the different jet and non-jet regions. Integrating the dihadron correlation in each of these regions gives the **number of charged hadrons produced per trigger particle** within events that contain a trigger.

3.5 Measuring the ϕ/h Ratio In Different Production Regimes

Once both the $(h-\phi)$ and $(h-h)$ 1D correlations are measured, and the different regions within the correlation space are defined, integrating within each of those regions gives the number of per-trigger pairs ($N_{(h-\phi)}$ and $N_{(h-h)}$) produced within the near-side jet, the away-side jet, and the underlying event. Since these pair-wise yields are approximately equal to the number of per-trigger associate particles (N_{ϕ} and N_h) produced, then this allows access to the per-trigger ϕ/h yield ratios within jets and within the underlying event separately. These ratio measurements give a direct way to look for changes to the production processes that are responsible for the overall observed strangeness enhancement.

Chapter Four: Analysis Details

This chapter will explain the exact event and track cuts used for this analysis, as well as all relevant technical details in performing the measurements discussed in the previous section.

4.1 Event & Track Reconstruction

To understand the event and track quality criteria used in this analysis, it is useful to have a basic understanding of the event reconstruction process used by ALICE during the LHC Run 2 data taking period. The ALICE track reconstruction method uses an iterative process to determine track parameters and the primary vertex (i.e. initial interaction point) at the same time, using a Kalman filter for smoothing and fitting[98]. The initial step is to find a first estimate of the interaction point using just the hits on the inner layer of the ITS detector, the SPD. Next, tracks are found by propagating track points inwards through the TPC towards this interaction point. Next, the TPC tracks are matched with points in the ITS detector, continuing the propagation inward. Once all tracks are propagated inwards, the interaction point is then refit, and the tracks are now refit and reconstructed by propagating outwards. At this point, the tracks are also matched with other detector signals if possible (TOF, EMCAL, etc.). After this outward propagation, the primary vertex is refit for a last time using the final track parameters.

4.2 Event Selection

The dataset used for this analysis was collected in the 2016 p-Pb period (LHC16q) during LHC Run 2. This period was run with a center of mass energy-per-nucleon of $\sqrt{s_{\mathrm{NN}}} = 5.02\,\mathrm{TeV}$. The events that were considered were taken from two separate but similar reconstruction schemes, labeled "FAST" and "CENT_wo_SDD". These two schemes are cross checked to confirm they have identical efficiency. Since these two datasets have the same detector configuration and were therefore compatible from a physics stand point, they were combined together to give a total sample of $\approx$ 600 million p-Pb minimum bias (MB) collision events. The MB trigger simply requires coincident signals from the two VZERO detectors (accounting for the difference in distance from the interaction point to the V0A and V0C components).

Events were further selected for analysis by requiring a primary collision vertex position of less than 10 cm from the center of the detector in the longitudinal direction, and with at least 3 reconstructed tracks in the event. The V0A estimator, which uses the signal of the V0A detector located in the forward rapidity direction, was chosen to determine event multiplicity percentile, and the events were separated into three multiplicity percentile bins: **0-20%**, **20-50%**, and **50-80%**. These event and multiplicity requirements reduce the total number of events considered to approximately 420 million events (see Table 4.1).

Multiplicity	Total Evts.	Has 3 Tracks	$\lvert \mathrm{Vtx}_Z \rvert < 10\mathrm{cm}$ + 3 tracks	% Pass
0-20%	1.218E08	1.217E08	1.061E08	87.1%
20-50%	1.840E08	1.835E08	1.590E08	86.4%
50-80%	1.850E08	1.804E08	1.563E08	84.5%

Table 4.1: Number of events passing our criteria for each multiplicity bin considered.

Because the collision beams are composed of focused clouds of particles called "bunches", when a bunch crossing occurs there is a probability that multiple proton-

proton or Ion-Ion pairs will collide during the same crossing. The tracks from these additional collisions, known as "pile-up" events, must be removed in order to correctly reconstruct the central collision of interest. Thus, for all events, a standard "physics selection" was applied offline to remove tracks and signals originating from collisions that occurred far away from the primary vertex.

The event multiplicity percentile bins can be converted to their mean charged particle multiplicity, so that the measurements made in p-Pb collisions can be properly compared to other collision systems. Previous studies in p-Pb have measured the corrected charge particle multiplicities for the central barrel region at $\sqrt{s_{\mathrm{NN}}} = 5.02\,\mathrm{TeV}$[99]. These published values are combined to provide the average multiplicities across the exact multiplicity bins used in this thesis (see table 4.2). The mean multiplicity has an $\approx 4\%$ error due to tracking efficiency systematics.

Multiplicity	$\langle N_{ch} \rangle$ for $\lvert\eta\rvert < 0.8$, $p_{\mathrm{T}} > 0.2\,\mathrm{GeV/c}$
0-20%	49.1 ± 2.0
20-50%	29.3 ± 1.2
50-80%	15.3 ± 0.6

Table 4.2: Average number of charged particles in the range $|\eta| < 0.8$, $p_{\mathrm{T}} > 0.2\,\mathrm{GeV/c}$ for the three different multiplicity percentiles used in this analysis.

In addition to the p-Pb dataset, simulated data was used for efficiency calculations and cross checks. These datasets are comprised of events created by both PYTHIA and DPMJET event generators[100], [101].

4.3 Track Selection

Specific quality cuts are applied to the particles within an event to ensure the tracks that are chosen for the analysis are correctly reconstructed. These include cuts on the number of TPC clusters that make up the track, the χ^2 of the track fit per

TPC track point, and how many clusters are shared with other reconstructed tracks. Because the correlation measurement requires three different types of particles (trigger hadrons, associated hadrons, and kaon candidates), different collections of track cuts are needed. These track cuts will also cut out some of the particles of interest, and therefore the final result must be corrected for the track cut efficiency (i.e. how many particles of interest that were produced in our collision made it through our track cuts). To estimate this efficiency, collisions are simulated with a Monte Carlo event generator. These produced particles then travel through a full simulation of the ALICE detector, built using GEANT3 [102]. The final efficiency estimated in this way includes both the tracking cuts efficiency, as well as the detector efficiency itself:

$$(\text{acceptance})\times(\text{efficiency}) = \frac{(\text{Total simulated particles detected that meet track cuts})}{(\text{Total simulated particles produced})} \tag{4.1}$$

where both the numerator and denominator are constrained to only particles in the central rapidity region ($|\eta| < 0.8$). The exact reconstruction efficiency of the detector can sometimes be dependent on the total multiplicity of the event. Because of this, the efficiency is calculated using simulated events with similar multiplicity to the three multiplicity ranges used in this analysis. Ultimately, the multiplicity range considered for this p-Pb analysis had no effect on the estimated efficiency, and therefore the final efficiencies are calculated from the full 0-100% multiplicity sample.

For tracking purposes, there are two types of particle tracks within the collision: primary tracks, and secondary tracks. Primary particles are those whose tracks originated near the initial primary vertex. These include particles that are produced directly from the initial collision, as well as resonance decay products since resonances will decay very close to the initial collision point. Secondary particles, on the other hand, are those that are the result of secondary weak decays. With weakly de-

caying particles corresponding to significantly longer lifetimes, weak decays typically occur within the central barrel of the detector, but far away from the primary vertex. These can be differentiated from primary tracks by requiring specific geometric cuts on the distance of closest approach (DCA) from the track to the primary vertex (see fig. 4.1). To find the DCA, reconstructed tracks are propagated backwards from their first track point in the detector back towards the primary vertex, accounting for the curve of the particle's trajectory due to the magnetic field and the particle's momentum. The further away that the track originated from the primary vertex, the more likely that the measured DCA is large.

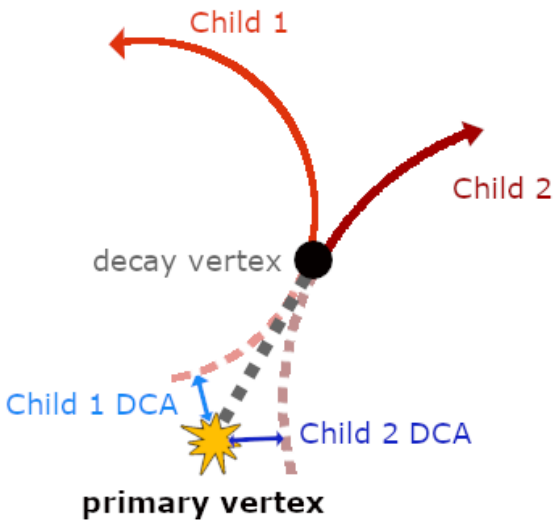

Figure 4.1: A diagram of the DCA of two secondary charged particle tracks. A neutral particle (grey dashed line) is produced in the initial collision, and decays into two charged child tracks (solid red lines) at the black dot. These secondary tracks are charged, and therefore show up in the detector. These two tracks are then propagated back towards the primary vertex (dashed red lines). The DCA is then the closest these back propagated tracks come to the primary vertex.

4.4 ϕ(1020) Reconstruction

In order to reconstruct the $\phi(1020)$ meson as discussed in section 3.3.1, the ϕ child track candidates require two types of track cuts. First, they need a set of track quality cuts to ensure they are well resolved tracks. Second, in addition to the quality cuts, they require particle identification (PID) cuts needed to identify kaon tracks specifically. While the invariant mass reconstruction will later remove any pions or protons misidentified as kaons, having PID cuts ensures that the signal to background ratio remains high in the ϕ mass peak region of interest.

Since the purpose of the analysis is to compare the production of $\phi(1020)$ inside and outside of jets, a momentum range of $1.5 < p_{\mathrm{T}}^{\phi} < 4.0\,\mathrm{GeV/c}$ is chosen for the associate $\phi(1020)$ meson. Performing the measurement above $4.0\,\mathrm{GeV/c}$ runs into statistical limits due to the lower number of $\phi(1020)$ produced. Conversely, performing the measurement below a momentum of $1.5\,\mathrm{GeV/c}$ gives a sufficiently large sample of $\phi(1020)$, but does not allow for a clear separation of jet and underlying event, due to the dominant non-jet production washing out the jet signal. This intermediate associate momentum range then gives a good mix of jet and non-jet production, while still ensuring sufficient statistical significance.

4.4.1 Kaon Track Reconstruction & Identification

Kaon candidates are selected from the central pseudorapidity region of $|\eta| < 0.8$ with a transverse momentum of at least $p_{\mathrm{T}} > 0.5\,\mathrm{GeV/c}$. To ensure high quality for the kaon candidate tracks, a standard set of quality cuts is applied to select for well-reconstructed primary particles, as also described in [103]. These include cuts on the minimum number of TPC clusters that make up the track ($N_{\mathrm{TPC}}^{\mathrm{clust}} \geq 80$ out of 159), as well as the χ^2 per TPC cluster in the final track reconstruction ($\chi^2/N_{\mathrm{TPC}}^{\mathrm{clust}} \leq 4$). They

also include a momentum dependent cut on the distance of closest approach (DCA) between the track and the primary vertex, using the requirement that $\mathrm{DCA}_{XY} < 0.0105 + 0.0350/p_{\mathrm{T}}^{1.1}$. Since the $\phi(1020)$ has a short lifetime ($\approx 46\,\mathrm{fm/c}$), this strict DCA cut ensures that the $\phi(1020)$ decay child candidates come from the primary interaction point of the event, cutting out particle tracks coming from secondary weak decays. Table 4.3 shows the full set of track cut parameters, including the requirement that the track parameters to be refit with the final reconstructed primary vertex.

Reconstruct with ITS Refit	true
Minimum Number of TPC Clusters	80
Max χ^2 Per TPC Cluster	4
Accept Kink Children	false
Max DCA To Vertex (Z)	2 cm
Max DCA To Vertex (XY)	$(0.0105 + 0.0350/p_{\mathrm{T}}^{1.1})$cm
2D DCA To Vertex	false
Max χ^2 TPC Constrained Global	36
Max χ^2 per ITS Cluster	36

Table 4.3: Track quality cut parameters for the kaon candidate (and associate hadron) tracks.

To isolate only kaon tracks, this analysis takes advantage of the two main ALICE subdetectors that have PID capabilities: the TPC and the TOF detector [104]. In both cases, the expected detector signal of a particle with a specific mass and momentum is a known quantity, using the Bethe-Bloche formula for the TPC energy loss dE/dx (eq. 2.1) and the TOF time (velocity) signal (eq. 2.3).

Due to the finite resolution of the track momenta and TPC energy loss ($\sigma_{dE/dx} \approx 5\%$) and TOF timing signal, the distribution of dE/dx (TOF β) signals for real kaons is treated as a Gaussian with a mean at the expected kaon value, and a width of σ_{TPC} (σ_{TOF}) that is fit experimentally. The distance of a particle's signal from the expected value can then be described in terms of the standard deviation of this

momentum dependent Gaussian fit, σ_{TPC} and σ_{TOF}. Explicitly, the TPC (TOF) signal is transformed with the equation:

$$n\sigma_{\mathrm{TPC(TOF)}} = \frac{(\text{signal}) - (\text{expected Kaon signal})}{(\text{std. deviation about Kaon expectation})} \tag{4.2}$$

where the expected Kaon signal and the standard deviation are both momentum dependent. A visual representation of this transform can be seen in figures 4.2 and 4.3.

To select kaon candidates, PID cuts were applied to both $n\sigma_{\mathrm{TPC}}$ and $n\sigma_{\mathrm{TOF}}$ of:

- $|n\sigma_{\mathrm{TPC}}| < 3$
- $|n\sigma_{\mathrm{TOF}}| < 3$

This relatively wide PID cut ensures that the majority of kaons will pass our PID cuts, while still cutting out a large amount of the background by excluding a large number of pions and protons (see fig. 4.4). In the final invariant mass reconstruction, this gives a signal to background ratio of $\approx$ 3:1 in the ϕ mass peak region (see fig. 3.5). This large signal to background ensures that the combinatorial background subtraction in the correlation measurement does not contribute a large statistical error to the final results.

4.4.2 ϕ(1020) Reconstruction Efficiency

For the full ϕ efficiency calculation, there are essentially three components: the tracking efficiency of the kaon children, the efficiency of the PID cuts, and the TOF hit efficiency of the kaon children. This last component comes from both the fact that the TOF detector does not have full acceptance in the detector (see section 5.2.2 for

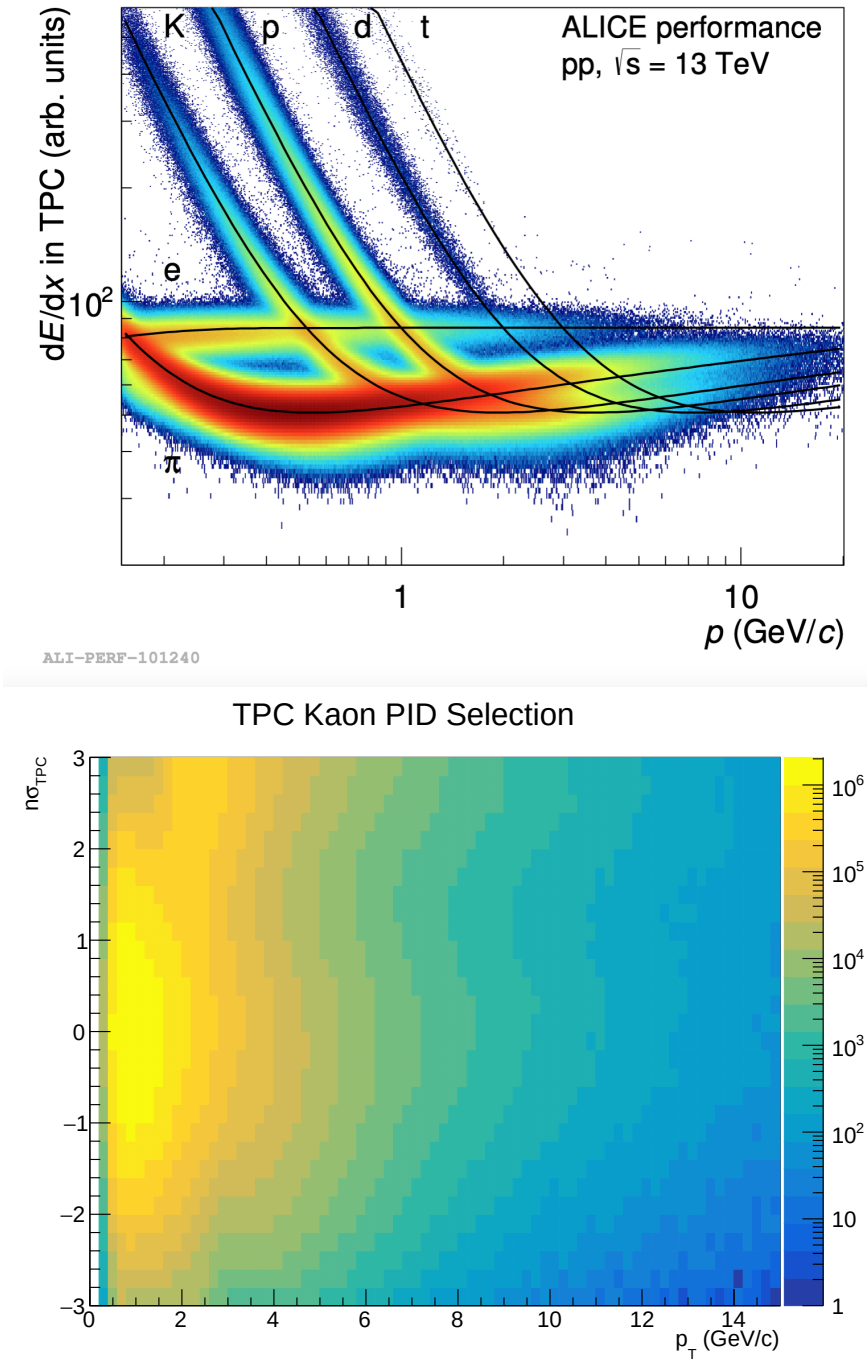

Figure 4.2: An example of the raw TPC dE/dx signal for a sample of tracks (top), and the dE/dx signal of tracks expressed in terms of the standard deviation of the distribution around the expected kaon signal vs. transverse momentum (bottom).

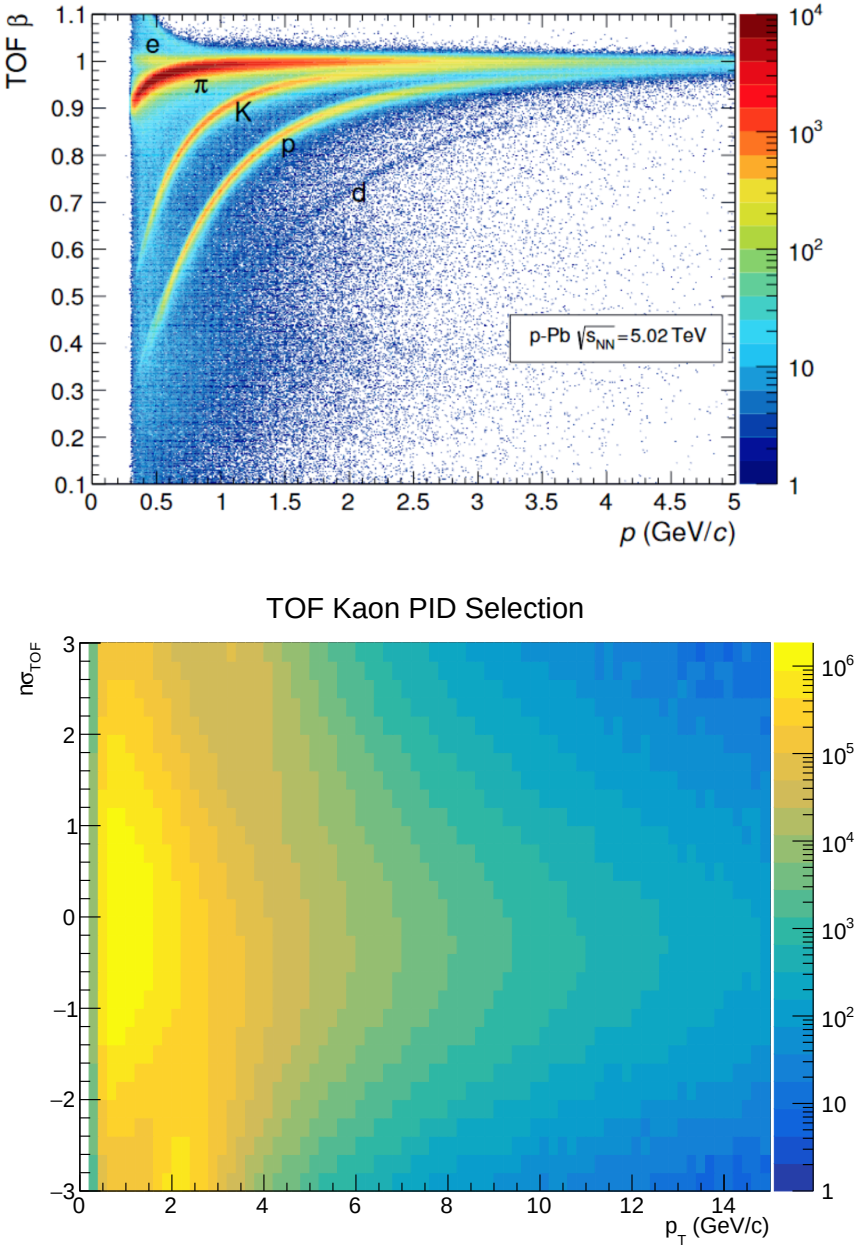

Figure 4.3: An example of the raw TOF β signal vs. momentum for a sample of tracks (top), and the β signal of tracks expressed in terms of the standard deviation of the distribution around the expected kaon signal vs. transverse momentum (bottom).

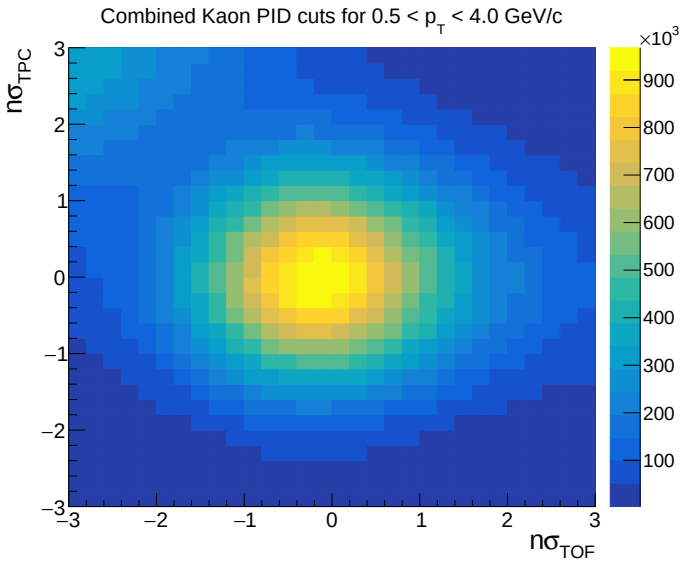

Figure 4.4: The 2D PID cuts on the kaon in $n\sigma_{\mathrm{TPC}}$ and $n\sigma_{\mathrm{TOF}}$ for the momentum range $0.5 < p_{\mathrm{T}} < 4.0\,\mathrm{GeV/c}$. The center peak is made up of kaons, while the peak at high $n\sigma_{\mathrm{TPC}}$ and low $n\sigma_{\mathrm{TOF}}$ (top left corner) is coming from pion contamination within these cuts.

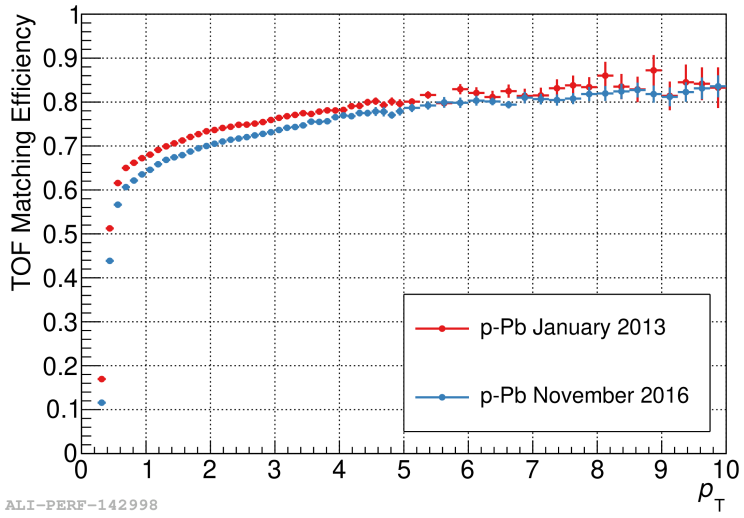

Figure 4.5: The ALICE TOF matching efficiency between TPC tracks and corresponding TOF signals in p-Pb collisions. Image from [105]

more information on TOF acceptance), and because not every reconstructed track is correctly paired with a corresponding TOF signal (see fig. 4.5) [105].

Reconstructed $\phi(1020)$ are chosen from the momentum range $1.5 < p_{\mathrm{T}} < 4.0\,\mathrm{GeV/c}$ for the correlation. The combined efficiencies give a final ϕ reconstruction efficiency that varies from roughly 10% to 25% across the momentum range for this analysis (see fig. 4.6). The momentum dependence of the $\phi(1020)$ efficiency is driven primarily by the two-track TOF hit requirement, as well as the simultaneous track quality cuts for both kaon tracks. The ϕ efficiency is found to be independent of event multiplicity, and therefore the final efficiency is calculated from the full 0-100% multiplicity event sample.

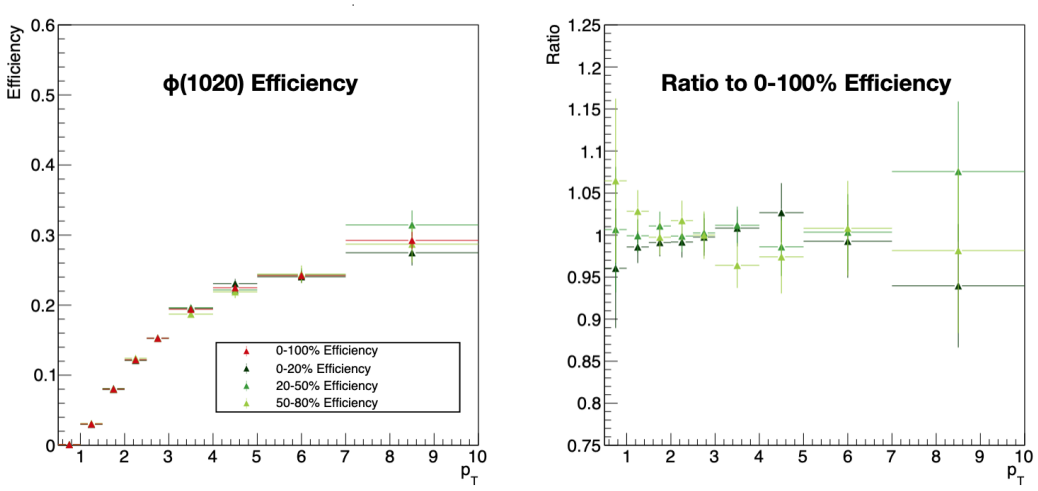

Figure 4.6: The efficiency for the reconstructed ϕ meson vs. p_{T} for four multiplicity bins (left), and the ratio between three different multiplicity bins and the full 0-100% multiplicity efficiency (right). From the ratio, within statistical fluctuations the efficiency is not dependent on multiplicity.

4.4.3 Trigger Hadron Tracking & Efficiency

The trigger particles are selected in a high momentum range in order to act as a proxy for a jet axis, specifically in the range $4.0 < p_{\mathrm{T}} < 8.0\,\mathrm{GeV/c}$. Because of this higher momentum requirement, the track quality cuts are slightly loosened in order to

capture a higher percentage of trigger candidates, and thus increase the statistics of the final correlation measurement. Specifically these trigger cuts, also used in [106], slightly relax the p_{T} dependent DCA requirement with a simple 2.4 cm (3.2 cm) cut in the transverse (longitudinal) distance to the primary vertex. However, the track does still need to be of sufficient quality to ensure an accurate momentum measurement, and to help ensure it is a real track and not a mis-reconstruction due to partial or merged tracks. This includes requiring that the track doesn't originate at a "kink" that would suggest a decay, and has a sufficiently low χ^2 per TPC cluster. These slightly looser track quality cuts are detailed in table 4.4.

Minimum Number of TPC Clusters	50
Max χ^2 Per TPC Cluster	4
Accept Kink Children	false
Max DCA To Vertex (Z)	3.2 cm
Max DCA To Vertex (XY)	2.4 cm
2D DCA To Vertex	true
Max χ^2 TPC Constrained Global	36
Max Fraction of Shared TPC Clusters	40%

Table 4.4: Track cut parameters for the trigger track.

With these relatively loose track requirements, we can again use Monte Carlo simulations to calculate the efficiency. These simulations give us an efficiency of $\approx$ 84% in the momentum range of the trigger particle, $4.0 < p_{\mathrm{T}} < 8.0\,\mathrm{GeV/c}$ (see fig. 4.7).

4.4.4 Associate Hadron Tracking & Efficiency

For the purpose of this analysis, the associate tracks of the dihadron correlation use the same quality cuts as the kaon candidate tracks (see table 4.3). This ensures that the associated hadron is also a primary particle, so that the comparison between

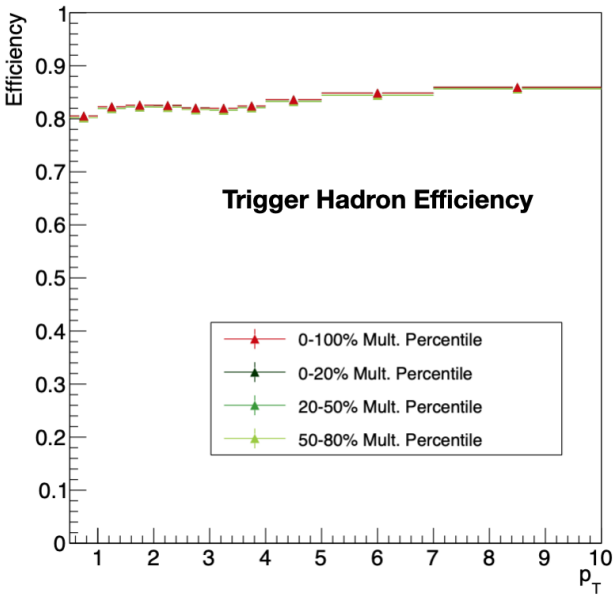

Figure 4.7: The efficiency for the trigger hadron vs. p_{T} for different multiplicity classes. Since the efficiency does not depend on the multiplicity, the final efficiency is calculated from the full 0-100% multiplicity sample.

ϕ and hadron production behavior is not influenced by any changes to secondary particle production.

Again, the reconstruction efficiency for these associate track cuts is computed using simulated Monte Carlo events. This gives a slightly lower efficiency compared to the trigger tracks (see fig. 4.8), with an efficiency of $\approx 80\%$ for the momentum region of interest, $1.5 < p_{\mathrm{T}} < 4.0\,\mathrm{GeV/c}$. It should be noted that even with the more stringent DCA requirements, a fraction of secondary decay particles do make it into our sample. This secondary contamination is estimated to be $\approx 1\%$ of the primary particles from simulations, and is included in the dihadron systematics. For the ϕ, this secondary contamination in the child candidates is removed via the invariant mass reconstruction process, and therefore does not impact the final results.

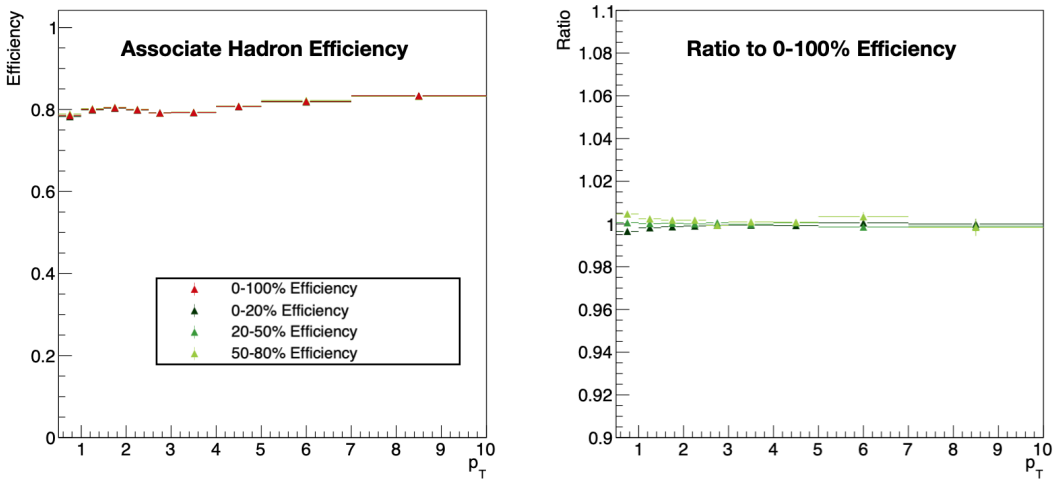

Figure 4.8: The efficiency for the associated hadron track vs. p_{T} for four multiplicity bins (left), and the ratio between three different multiplicity bins and the full 0-100% multiplicity efficiency (right).

Chapter Five: Systematic Errors & Cross-checks

Before the main results are discussed, it is important to look at the potential sources of systematic bias in both the central correlation measurement and the pair-wise yield measurement. To this end, a collection of systematic uncertainty sources is presented in this Chapter. Like-wise, in order to ensure that the final physics message is not influenced by potential biases in the measurement procedure, a collection of different cross-checks exploring biases in the measurement procedure are presented.

5.1 Monte Carlo Closure Tests

One of the more general tests for an experimental measurement process is a Monte Carlo closure test [107]. This test uses simulated data to ensure that the measurement is correctly capturing the "real" signal. The basic principle of a closure test in the context of this analysis is:

1. Produce a collection of simulated events where the particles travel through a full simulation of the ALICE detector, and the detector signals are processed through the same track reconstruction process as experimental data.

2. Perform the full, efficiency corrected measurement procedure on these simulated reconstructed tracks.

3. Access the true particles produced in the simulation, and take their species and exact momentum without considering the detector reconstruction.

4. Perform the correlation measurement in the simulation with the true ϕ and the true trigger hadrons.

5. Take the ratio of the "reconstructed" measurement and the "true" measurement.

This ratio directly tests both the measurement procedure and the efficiency corrections. If the ratio is equal to 1, then the procedure of reconstruction and efficiency correction fully reproduces the original distribution. On the other hand, deviations from 1 would reflect that the measurement procedure introduces a non-physical bias compared to the "real" correlation.

Since the measurement procedure includes both reconstructing the ϕ (1020) and obtaining the $(h-\phi)$ correlation, the closure test ratio was performed in two different stages. First, the results using the "true" ϕ meson (ϕ_{MC}) were compared with the measurement using "true" kaon particles (KK_{MC}) for the ϕ reconstruction procedure. This tests the invariant mass reconstruction method directly, without contributions from the track reconstruction or particle identification. For this closure test, trigger hadrons are selected from the real generated primary hadrons for both the $(h-\phi_{\mathrm{MC}})$ and $(h-KK_{\mathrm{MC}})$ cases. Kaon candidates are selected from the generated primary kaons such that the pair has a central pseudorapidity of $|\eta_{KK}| < 0.8$. The correlation using these kaon pairs then goes through the full reconstruction procedure as detailed in section 3.3.1 (i.e. mixed event correction, like-sign background subtraction using sideband scaling, branching ratio and mass peak correction factors applied). Comparing the true $(h-\phi_{\mathrm{MC}})$ correlation with the $(h-KK_{\mathrm{MC}})$ showed that the reconstruction method correctly recovered the underlying correlation, and was found to be closed (see fig. 5.1).

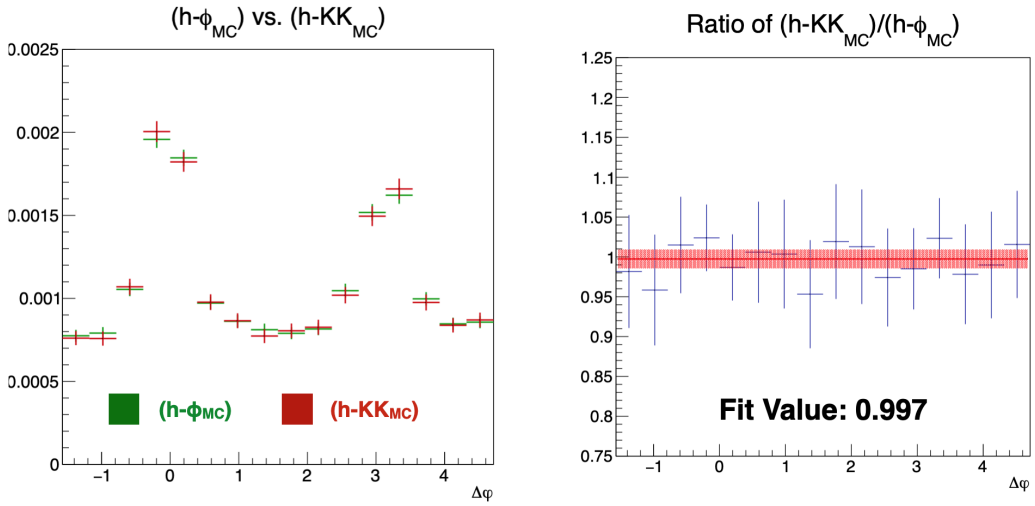

Figure 5.1: Monte Carlo closure test performed for the $(h-\phi)$ reconstruction method using unlike sign kaon pairs. The correlations within a collection of MC generated events are compared using the real $(h-\phi_{\mathrm{MC}})$ and the reconstructed $(h-KK_{\mathrm{MC}})$ measurement (left). The ratio of the reconstructed to the real correlation is found to be close to one (right), meaning the reconstruction technique is found to be closed.

Next, the "true" results were compared with the measurement using the full simulated track reconstruction, denoted $(h-KK_{\mathrm{track}})$. This both tests the efficacy of the efficiency correction and looks for biases in the kaon selection procedure on the final results. Similar to how the efficiencies were calculated in section 4.4.2, this test sends MC generated particles through a simulated ALICE detector and uses the same track reconstruction techniques that are used in data. These simulated tracks are subject to the same quality and PID cuts that the kaon candidates in data are, and then have the full efficiency and acceptance correction factors applied to them. These identified kaon candidates then go through the same reconstruction method as in data (and the previous closure test). The final results show that the efficiency corrected reconstructed per-trigger $(h-KK_{\mathrm{track}})$ correlations reproduce the original $(h-\phi_{\mathrm{MC}})$ correlation well (see fig. 5.2). The closure of these two MC tests give good confidence that the acceptance*efficiency calculation and the overall measurement

procedure are correctly reconstructing the per-trigger $(h-\phi)$ correlation.

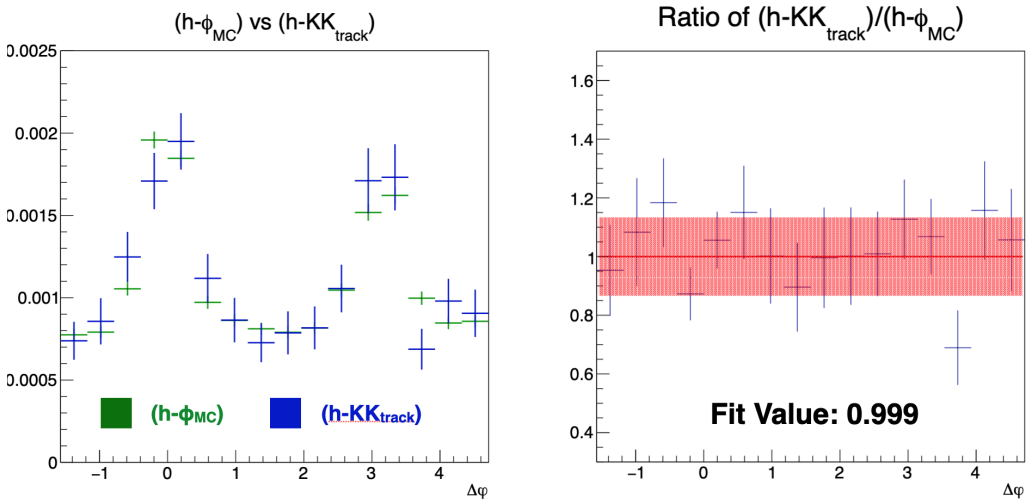

Figure 5.2: Monte Carlo closure test performed for the full efficiency corrected $(h-\phi)$ reconstruction technique. The correlations within a collection of MC generated events are compared using the real $(h-\phi_{\mathrm{MC}})$ and the reconstructed $(h-KK_{\mathrm{track}})$ measurement (left). The ratio of the efficiency corrected reconstructed to the real correlation is found to be close to one within the statistical errors(right), meaning the test of the full measurement procedure is found to be closed.

However, even with a full Monte Carlo closure test passed, the large errors on the closure ratio means that a thorough check of systematic uncertainty is still required. This includes both systematic biases in the measurement procedure, as well as errors introduced by the simulation in accounting for detector acceptance and efficiency effects.

5.2 Measurement Bias Cross-checks

Since the main physics message of this dissertation lies in the change of strangeness production in collisions as a function of multiplicity, it is necessary to examine the measurement procedure for any selection biases that would effect either the per-trigger yields, or the final $(h-\phi)/(h-h)$ ratios. Three avenues of bias were identified:

1. Biases due to using the per-trigger pair-wise $(h-\phi)/(h-h)$ yield ratios to approximate the underlying ϕ/h ratio.

2. Biases due to differences in the measurement procedure of the $(h-\phi)$ correlation compared to the $(h-h)$ correlation.

3. Biases due to the shape of the non-jet/underlying event portion of the correlation changing with multiplicity.

For each of these cases, cross-checks were designed specifically to assess the effect of these biases. These included: testing the effect that fluctuations in the number of triggers in an event would have on the ϕ/h approximation; cross-checking the effect of requiring a TOF hit for the $\phi(1020)$ children but not for the dihadron associate particle; and using different background shape assumptions to test the sensitivity of the near and away-side jet yields and yield ratios.

5.2.1 Bias in Events with Multiple Triggers

The main physics message of the correlation ratio technique described in this analysis relies on the ability to treat the per-trigger $(h-\phi)$ pair yields as an approximation of the number of ϕ produced per trigger particle. This relation can be expressed as:

$$\frac{1}{N_{\text{trig}}}\sum_{i}^{N_{\text{evts}}}\left(N_{\text{trig},i}\times N_{\phi,i}\right)\approx\frac{1}{N_{\text{trig}}}\sum_{j}^{N_{\text{evts}}^{\text{trig}}}N_{\phi,j} \tag{5.1}$$

where the left sum is taken over the total number of events, the right sum is taken over only events that have a high momentum trigger particle (N_{trig} being the total number of trigger particles), and $N_{\text{trig},i}$ and $N_{\phi,i}$ are the number of trigger particles and associated ϕ in event i, respectively. The left side of the equation is the total number of per-trigger pairs in the events, and the right side is the total number of

ϕ's produced per trigger. If each event contains at most one trigger particle then this relationship will hold exactly. For the trigger criteria in the jet-like ($h-\phi$) correlation, of the events that contain at least one trigger particle, $\sim 90\%$ contain exactly one trigger particle. Since this means the average number of triggers per triggered event is close to one, this relationship should approximately hold. However, fluctuations in the number of trigger particles per event can still cause the left side of the equation to be larger than the right, due to the pair-wise nature of the sum.

An additional cross-check was performed to ensure that the trends observed in the per-trigger $(h-\phi)/(h-h)$ measurement are not influenced by this approximation, and to ensure that the difference between the exact and approximate relationship is small. A cross-check correlation was performed using only the single highest momentum trigger particle in an event (within the trigger range $4.0 < p_{\mathrm{T}} < 8.0\,\mathrm{GeV/c}$) for the correlation. This highest-trigger requirement ensures that the relationship in equation 5.1 is exact, since $N_{\mathrm{trig},i} = 1$ for all events with a trigger. By then comparing the highest-trigger results with the standard measurement procedure using all triggers, the overall effect of pair-wise counting on the estimation of associate particle yields can be examined.

A direct comparison between the all-trigger and highest-trigger correlation functions can be seen in figure 5.3. This comparison shows the expected behavior, where the small number of events with multiple triggers causes the standard all-trigger correlations to be higher than for the highest-trigger case.

The all-trigger and highest-trigger cases can be quantitatively compared by taking the ratio between the two correlations for each multiplicity bin (fig. 5.4). This ratio shows that the correlation using all-triggers corresponds to a $\approx 5\%$ higher yield than the underlying "true" ϕ yield (which is equal to the highest-trigger $h-\phi$ yield). This

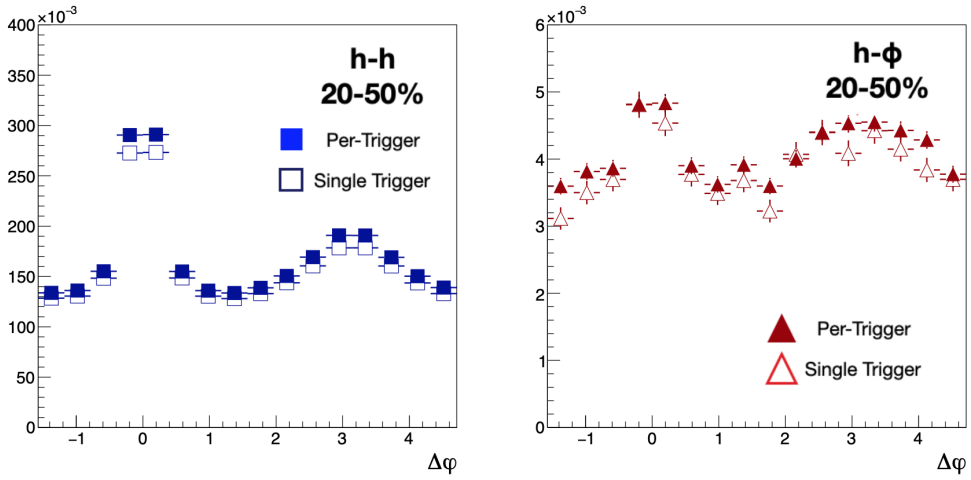

Figure 5.3: Comparison of the standard correlation taking all triggers (full points) with the correlation performed with just the highest momentum trigger of each event (open points) for the $h-h$ (left) and $h-\phi$ (right) correlations.

effect is seen to be the same for both the $(h-h)$ and $(h-\phi)$ correlations, leading to the final ϕ/h ratio being accurately estimated by the $(h-\phi)/(h-h)$ ratio, since this 5% effect cancels out.

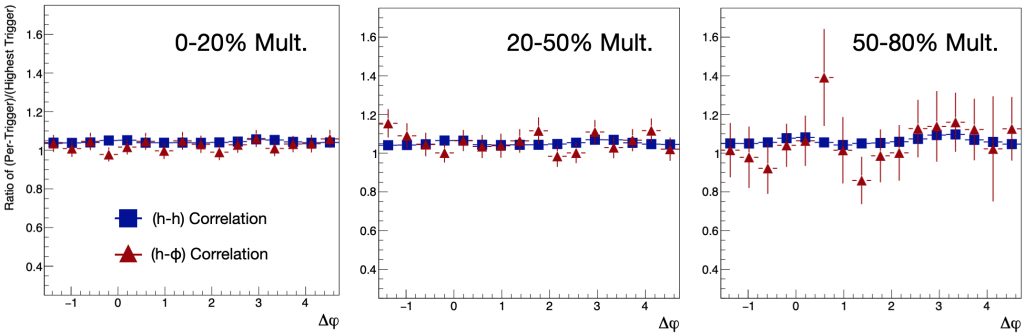

Figure 5.4: Ratio of the all-trigger correlation divided by the highest-trigger correlation, presented from high multiplicity (left) to low multiplicity (right).

This cross-check does also introduce a new bias, however, in that it slightly hardens the p_{T} spectra for the trigger hadron (see figure 5.5), which can then cause a change to the correlation shape as well. This effect on the correlation shape can be seen

in the all-trigger/highest-trigger ratio. While this change in shape is partly due to the selection bias in the highest-trigger correlation, and therefore should not affect the standard all-trigger correlation, it can be used to estimate an upper limit on any effect the "double pair counting" in the all-trigger correlation could have on the jet yield calculation. This shape effect is calculated to give a maximum systematic bias of a $\approx 5\%$ enhancement to the jet yields for the low multiplicity correlation, and has a negligible effect at high multiplicity.

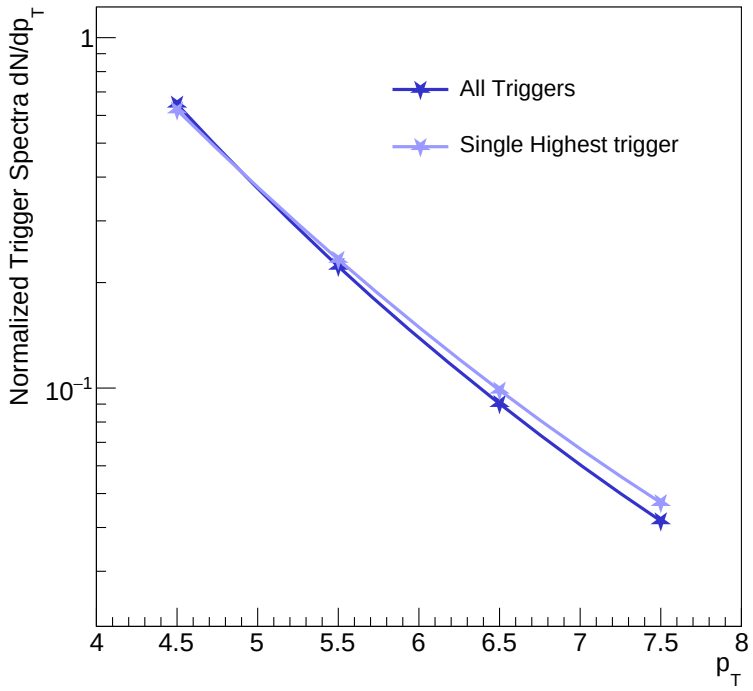

Figure 5.5: Comparison of the normalized p_{T} spectra of the triggers used in the standard correlation measurement (dark blue), and the normalized spectra from just taking the highest trigger particle in each event (light blue).

5.2.2 Effects of TOF Detector Asymmetries

Since the main goal of this thesis is to compare the differences in production between $\phi(1020)$ mesons and inclusive hadrons, it is important to look for steps in the correlation measurement process that would bias one of these measurements and not the other. One such possible source of bias lies in the requirement of a TOF signal, and therefore a hit in the TOF detector, for the kaon candidates. The associate hadrons have no such TOF hit requirement, so this creates a possible difference between the two measurements. Due to the physical space constraints within the ALICE central barrel, the TOF detector has incomplete coverage over the central η, φ range that is used in the correlation measurement (see figure 5.6). Since only the $\phi(1020)$ children are required to have a hit in the TOF detector, it is important to establish that this incomplete coverage does not significantly influence the correlation measurement.

To test this effect, when measuring the $(h-\phi)$ correlation the detector was broken into two regions for selecting the $\phi(1020)$: a region with the hole in the TOF detector $(-\pi < \varphi < 0)$, and a region with full TOF detector coverage $(0 < \varphi < \pi)$. The correlations using these two separate regions for the associate $\phi(1020)$ are compared with each other in figure 5.7. Within statistical fluctuations, these correlations are identical, showing that the hole in the TOF detector does not have a meaningful effect on the final $(h-\phi)$ correlation shape. Therefore, the requirement of having a TOF hit for the $(h-\phi)$ reconstruction does not affect the comparison between the $(h-\phi)$ and $(h-h)$ correlations.

5.2.3 Underlying Event Shape Assumptions

One of the main sources of systematic uncertainty on the final yields and yield ratios lies in estimating the underlying event (UE) within the correlations. Since this

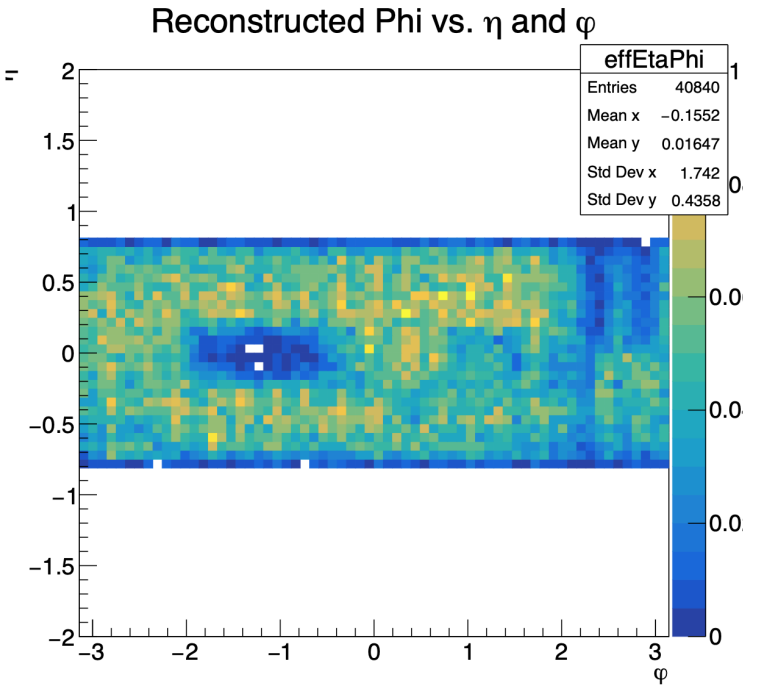

Figure 5.6: The (φ, η) position of reconstructed $\phi(1020)$ mesons within a subset of p-Pb events. The acceptance "hole" on the left is due to the incomplete TOF detector coverage, causing kaon candidates to be missed in that region.

baseline determines the cut-off point for the jet yield integrals, this effects both the underlying event and jet yield measurements. To estimate the effect the UE determination may have on the final yields, a variety of different background estimation methods are tested: a flat fit to different subsets of the non-jet points (i.e. just points around the near-side, just points around the away-side, etc.), a ZYAM-like [97] estimate by setting the UE at the lowest $\Delta\varphi$ point, and a full fit for the entire correlation structure, performed with the function:

$$f(a_i|\Delta\varphi) = a_0 + a_1\left(e^{\left(\frac{\Delta\phi-a_2}{a_3}\right)^2} + e^{\left(\frac{\Delta\phi-a_2\pm 2\pi}{a_3}\right)^2}\right) + a_4\left(e^{\left(\frac{\Delta\phi-a_5}{a_6}\right)^2} + e^{\left(\frac{\Delta\phi-a_5\pm 2\pi}{a_6}\right)^2}\right) \quad (5.2)$$

where the function contains a flat background plus Gaussian distributions for both the near and away-side jet peaks. To aid in the fitting, the means of the near

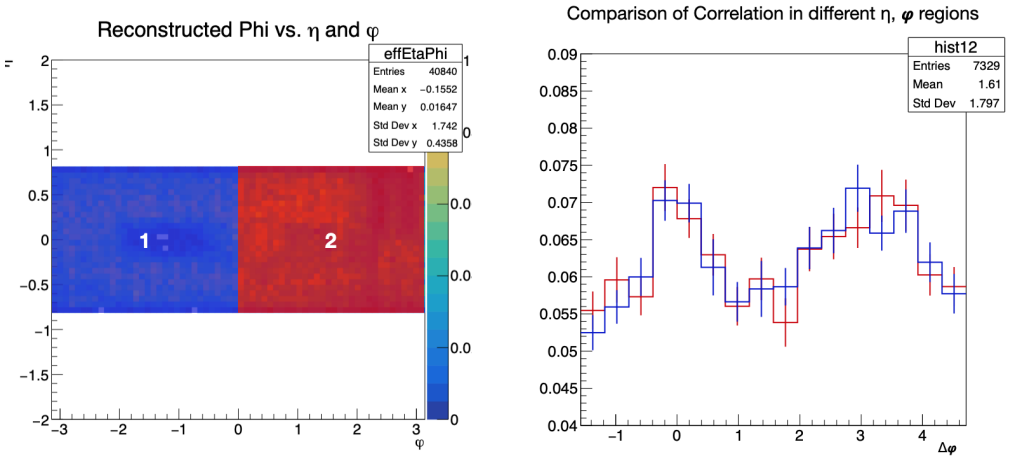

Figure 5.7: Comparison of the $(h-\phi)$ correlation from two different regions in the detector to test for effects from the TOF acceptance. The left plot shows the two regions of the central barrel that $\phi(1020)$ were taken from: the region with the TOF hole (blue), and the region with full TOF coverage (red). The right plot shows a comparison of the normalized $\Delta\varphi$ correlations using $\phi(1020)$ from the two described regions.

and away-side Gaussian peaks are fixed to 0 and π, respectively. The $\Delta\varphi$ variable is cyclical by nature, and so the near and away-side peaks are repeated at $\pm 2\pi$ to account for this.

Many of these methods (especially simply varying the number of points to fit for the UE) are susceptible to capturing mostly the statistical fluctuations of the correlation. However, they do also include the effects that the jet peak tails have on the UE estimation. Because of this, these variations give a good estimate of the effect that the jet tails could contribute to the underlying event determination. The total systematic effect of this on the per-trigger yields was then determined by taking the standard deviation of these yields across the different background methods, giving an error for the near-side yields ranging from $\sim$2% in the high multiplicity h-ϕ correlation, to $\sim$5% in the lowest multiplicity bin. The h-ϕ away-side yields

are slightly more dependent on the background estimation, and are found to have a systematic error of $\sim 7\%$ for each multiplicity bin. The effect of the different background estimations on the underlying event yields were negligible. For the h-h correlations, all different background estimation methods give similar jet yields ($< 1\%$ difference to the final yields), and the systematic effects from the h-h background estimation are therefore ignored.

5.2.3.1 Estimated v_2 Contribution to Correlation

The other main source of systematic uncertainty with respect to the underlying event is the assumption that the underlying, non-jet part of the correlation is flat in $\Delta\varphi$. Physically, this is equivalent to the assumption that the direction of a dijet axis is uncorrelated with the overall shape of the non-jet particle distribution within an event.

However, as discussed in section 1.5.3, previous studies of heavy-ion collisions have shown that the collective flow components of the QGP (v_1, v_2, etc.) influence the spatial distribution of particles within an event. Within two-particle angular correlations, these flow components can be described using an expansion in the two particle relative angle:

$$\frac{dN^{\text{pair}}}{d\Delta\varphi} = a_0 + 2a_1 \cos\Delta\varphi + 2a_2 \cos 2\Delta\varphi + \ldots \tag{5.3}$$

where as before, $v_n \equiv a_n/a_0$. This means that even without an event-by-event reconstruction of the reaction plane, the structure of general two particle angular correlations in heavy-ion collisions contains the effect of collective flow [108]–[110]. Specifically, this flow would manifest in the correlation as a non-jet background that is not flat with respect to $\Delta\varphi$, challenging the above UE estimation assumption.

Recent ALICE studies of collective behavior in small systems have measured positive flow components in high multiplicity p-Pb collisions[111]. For the purpose of two-particle correlation measurements, the only flow component that is large enough to significantly influence the $(h-\phi)$ and $(h-h)$ correlation in the momentum ranges considered here is the elliptic flow component, v_2. For the dihadron correlation, the measured values for inclusive charge particle v_2 can be used directly for the associate momentum bins in high multiplicity p-Pb collisions (see the measured v_2 vs. p_{T} in figure 5.8). However, the v_2 values for momentum higher than $4\,\mathrm{GeV/c}$ have not been measured in p-Pb collisions. Furthermore, the v_2 in lower multiplicity p-Pb collisions is less well constrained. As an estimate, this cross-check will assume a v_2 for the middle and low multiplicity bins as 15% and 50% lower than the high multiplicity v_2, respectively, and will assign a trigger v_2 value taken from the charged hadron $3.0 < p_{\mathrm{T}} < 4.0\,\mathrm{GeV/c}$ range (see table 5.1). It will also be assumed that factorization of flow components is a valid decomposition, so that the two particle flow can be calculated as $v_2^{h-h} = v_2^{\mathrm{trig}} \times v_2^{\mathrm{assoc}}$. This factorization assumption is shown to hold well in low associate and trigger momentum ranges, and to approximately hold for the trigger and associate momentum ranges considered in this analysis [112].

Multiplicity Pctl.	trigger v_2	assoc. hadron v_2	$(h-h)$ $v_2 = (v_2^{\mathrm{trig}}) \times (v_2^{\mathrm{assoc}})$
0-20%	0.11	0.13	0.014
20-50%	0.09	0.10	0.009
50-80%	0.06	0.07	0.004

Table 5.1: Estimated v_2 values used for systematic uncertainty related to the determination of the underlying event. Values taken from [111].

The v_2 of identified $\phi(1020)$ mesons has not been explicitly measured before in p-Pb collisions. Because of this, the flat background estimate was kept for the central measurement, while assigning a $\phi(1020)$ v_2 value that is the same as the inclusive

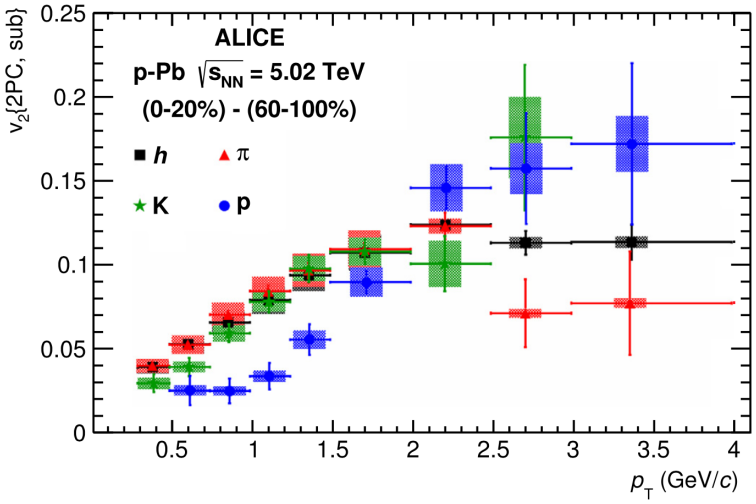

Figure 5.8: Measured values of elliptic flow coefficient v_2 in 0-20% multiplicity p-Pb collisions for different particle species, as a function of p_{T}. Due to the cross-over of different particle species in low momentum, the use of total charged particle v_2 for the associate hadron and ϕ meson is a good approximation [111].

charged hadron v_2 for the background is treated as a systematic uncertainty. In order to check that this assumption is valid to make for the $(h-\phi)$ correlation at all, the charged hadron v_2 is compared with a $\phi(1020)$ v_2 that is estimated from the $(h-\phi)$ correlation directly.

One method of extracting flow components from two particle angular correlations is to subtract off the low multiplicity correlation from the high multiplicity correlation (see figure 5.9). Since the low multiplicity correlation should have a much smaller flow contribution, this subtraction is a way to remove the jet contribution from the high multiplicity correlation. This remaining jet-subtracted correlation can then be fit with the flow coefficients for an estimate of the underlying v_2. This method allows for the extraction of v_2 for high and mid multiplicity regions, within the assumption that the lowest multiplicity bin used for subtraction has minimal collective flow.

As a cross-check, this low multiplicity subtraction technique was also applied directly to the correlations measured for this analysis. In order to increase statistics,

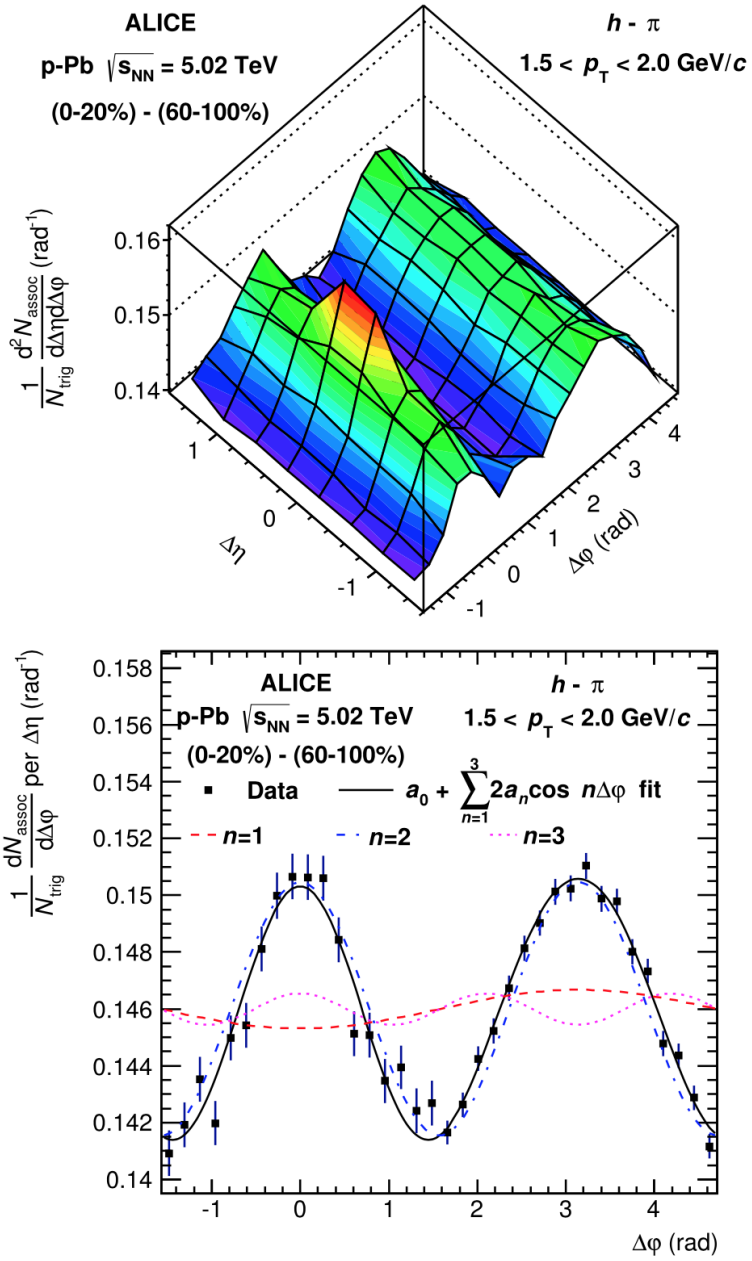

Figure 5.9: An example of finding the flow coefficients by subtracting the low multiplicity correlation from the high multiplicity correlation. The 2D subtracted correlation is shown for the $(h-\pi)$ case (top). This subtracted correlation is projected onto $\Delta\varphi$ from the large $\Delta\eta$ region ($0.8 < |\Delta\eta| < 1.6$ for the near-side, $|\Delta\eta| < 1.6$ for the away-side) for fitting the flow coefficients (bottom) [111].

the trigger momentum range was slightly widened to $3.0 < p_{\mathrm{T}}^{\mathrm{trig}} < 8.0\,\mathrm{GeV/c}$. Since the smallest multiplicity bin for this thesis is the $50-80\%$ bin where a small amount of collective flow is still expected, the subtraction is expected to remove some flow component as well as the jet. With this approximation, the subtracted correlation is then fit to find the elliptic v_2 contribution (see fig. 5.10). The fit value of the $(h-\phi)$ v_2 with this method is ≈ 0.017. Though the statistical errors are quite large, this fit value is in line with the assumption of 0.014 made with the published charged hadron v_2.

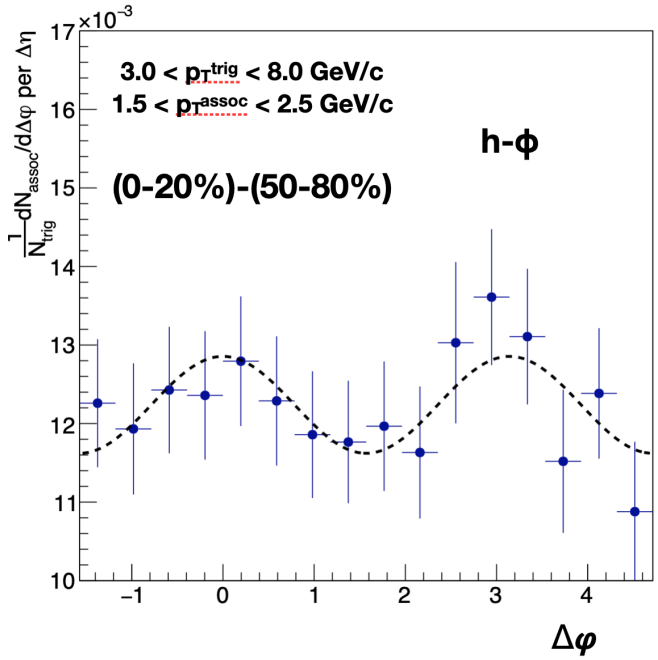

Figure 5.10: An estimate of the flow contribution of the $(h-\phi)$ correlation by subtracting the low multiplicity correlation from the high multiplicity correlation.

An additional cross-check to justify the assumption of using the charged hadron v_2 for the $(h-\phi)$ correlation was to look at the $\Delta\varphi$ correlation in the range where $\Delta\eta$ is far from 0. In this large $\Delta\eta$ region, the near-side jet should be mostly removed from the correlation, while the away-side jet and the flow contribution will still remain.

By then fitting the area under the near-side with a dipole term, the v_2 value can be extracted from these long range correlations.

For this v_2 estimation, long range correlations were measured by performing the standard 2D correlation procedure, then only projecting the range $0.8 < |\Delta\eta| < 1.2$ onto $\Delta\varphi$ for the final 1D angular correlation. The estimated flow contribution using the charged hadron v_2 values can be compared directly with the correlation shape on the near-side of this measurement (see fig. 5.11). Within errors, using the charged hadron v_2 was able to correctly describe the long-range near-side correlations, pointing to this v_2 value being a reasonable assumption for both the $(h-h)$ and $(h-\phi)$ underlying event.

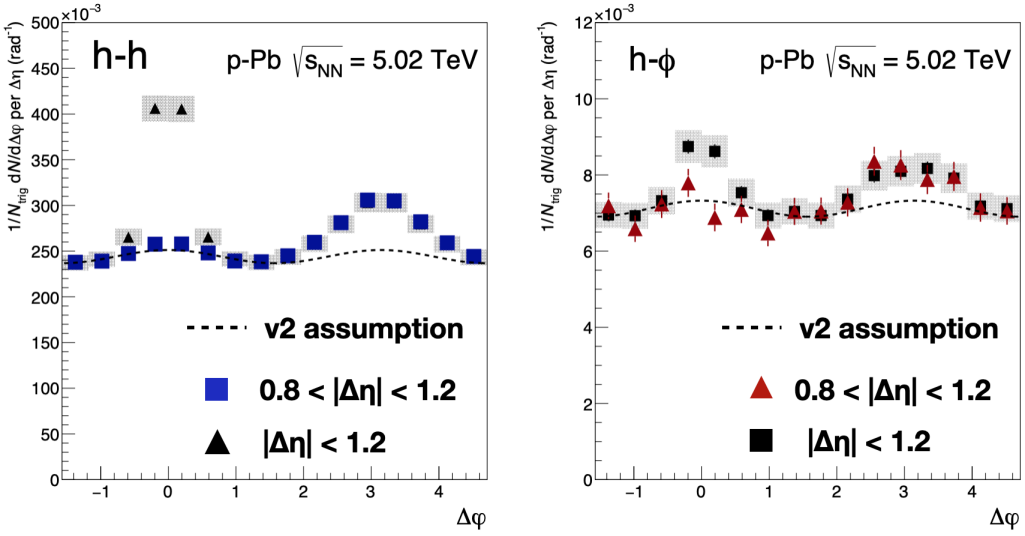

Figure 5.11: Comparison of the published charged hadron v_2 with the angular correlation in both the full $\Delta\eta$ range and the outer $\Delta\eta$ range $0.8 < |\Delta\eta| < 1.2$ for the dihadron (left) and $(h-\phi)$ correlation (right). The charged hadron v_2 values match the near-side region of the wide $\Delta\eta$ correlation in both cases.

For the lower $1.5 < p_{\mathrm{T}}^{\mathrm{assoc}} < 2.5\,\mathrm{GeV/c}$ momentum $h-\phi$ $(h-h)$ yields, the charged hadron v_2 assumption lowers the jet yields by between 4% (1%) for the lowest multiplicity and 25% (16%) for the highest multiplicity. Likewise, the higher

$2.5 < p_{\mathrm{T}}^{\mathrm{assoc}} < 4.0\,\mathrm{GeV/c}$ momentum $h-\phi$ $(h-h)$ yields are lowered by between 1.4% (0.6%) for the lowest multiplicity and 16% (9%) for the highest multiplicity. Due to the non-zero v_2 effecting the near and away-side yields in similar amounts, this does not effect any differences in the relative behaviour between the near and away-side jet yields. Because the $(h-\phi)$ and $(h-h)$ jet yields are both lowered by the v_2 assumption, the effect on the final ratio is smaller than on the individual yields. The v_2 assumption has a $\sim 10\%$ effect on the highest multiplicity jet yield ratios for the low momentum measurement, and an $\sim 8\%$ effect on the highest multiplicity jet yield ratios for the high momentum measurement.

5.3 Systematic Uncertainty Sources

The primary systematic uncertainties for the correlation measurements are divided into two main categories: those associated with tracking efficiency and reconstruction, and those associated with the $\phi(1020)$ reconstruction procedure used to measure the $(h-\phi)$ correlation. The tracking and reconstruction systematic uncertainties include the global tracking efficiency, the material budget of the detector, and the track selection cuts on the associated hadron and the $\phi(1020)$ decay children. These tracking errors are approximately 3.6% for the hadrons, and 5.2% for the reconstructed $\phi(1020)$ (due to the error on both of the two child tracks) [103], [113].

For the $h-\phi$ correlation, additional systematic errors are estimated by varying different steps of the ϕ reconstruction process, including: the invariant mass regions used for the $\phi(1020)$ mass peak, the left and right sideband mass regions used for combinatorial background removal, the like-sign background scaling factor, and PID cuts on the kaon daughters. To estimate the systematic effects on the measurement, the ratio of the correlation using a varied cut to the correlation with the standard

cut is calculated. Then the ratio for each $\Delta\varphi$ point is used to calculate the RMS of the variation across the entire correlation. The specific variations of these cuts are explained in the following sections, while the final contributions of these systematic errors are summarized in table 5.2 and shown in figure 5.12.

All systematic effects on the correlation measurement that were considered are found to be $\Delta\varphi$ independent, and are therefore applied evenly to the full $\Delta\varphi$ correlation. These errors also do not vary within the p_{T} ranges considered, and therefore are applied to both p_{T} bins equally. The dominant systematic errors for the correlation measurement are found to lie in the estimation of the tracking efficiency for the detector. For the per-trigger yield measurements, the main source of systematic uncertainty is in the flat UE background estimation, as discussed in the previous section.

h-ϕ Error per $\Delta\varphi$ bin

Multiplicity	0-20%	20-50%	50-80%
Mass Peak Range	0.8%	1.3%	2.7%
LSB Mass Range	1.1%	0.9%	2.6%
RSB Mass Range	0.2%	0.3%	1.2%
k_{LS} Scale Factor	0.9%	0.6%	3.0%
k_{Signal} Scale Factor	0.8%	0.8%	0.8%
PID cut	1.0%	1.0%	1.0%
Tracking Eff.	5.2%	5.2%	5.2%
Total Syst.	5.6%	5.6%	7.3%
Avg. Statistical Error	2.2%	3.2%	7.3%

Table 5.2: The systematic errors on the h-ϕ angular correlation, expressed as percent of bin value. Also shown here are the average statistical error per $\Delta\varphi$ bin as a comparison.

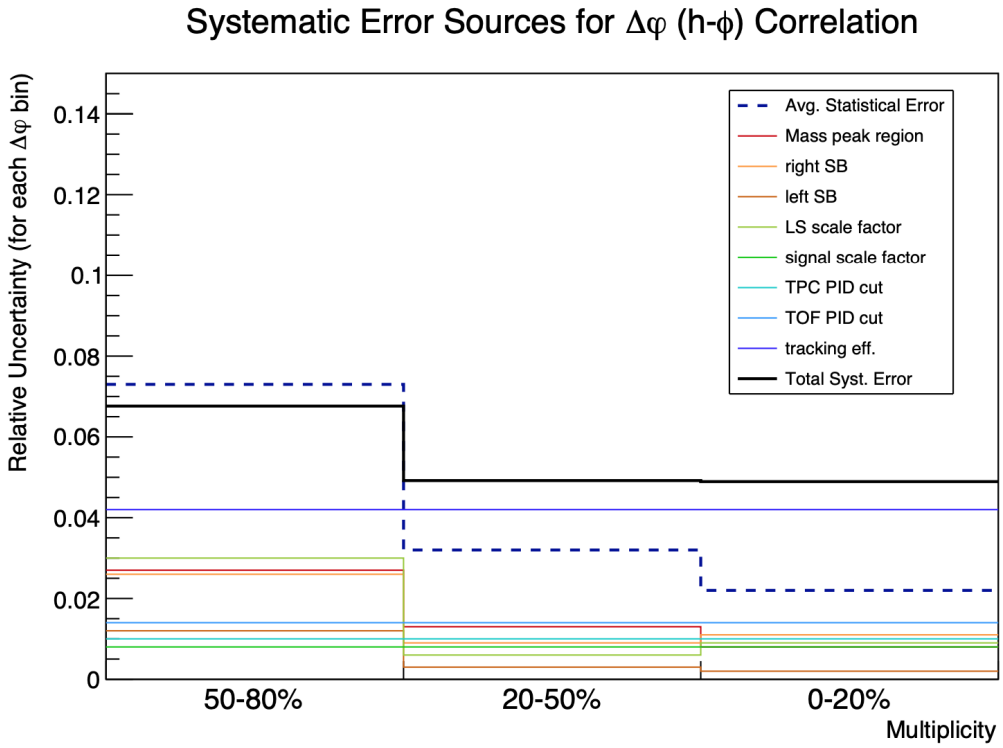

Figure 5.12: Visual depiction of the different sources of systematic uncertainty on the $(h-\phi)$ correlation for the three different multiplicity bins. Uncertainty is plotted as the average relative uncertainty (error/value) per $\Delta\varphi$ bin of the correlation. The total systematic error is depicted as a solid black line, and the total statistical error per $\Delta\varphi$ bin is shown for comparison (dashed line)

5.3.1 Particle Identification

Since the PID cuts to select kaon candidates are wide in order to capture a large percentage of the total produced kaons, there are a percentage of misidentified pions and protons that remain in the kaon candidate sample. The invariant mass reconstruction and background removal techniques should remove this non-kaon portion of the invariant mass distribution. However, this can be tested directly by varying the PID cuts (and the corresponding efficiency due to the MC efficiency calculations). The width of the TPC PID cut was varied by increments of 0.2 in units of $n\sigma_{\mathrm{TPC}}$

from the standard cut of $|n\sigma_{\mathrm{TPC}}| < 3$ to the tighter cut of $|n\sigma_{\mathrm{TPC}}| < 2$. With these cuts, the final $(h-\phi)$ correlation is seen to only vary by $\sim 1\%$ (see figure 5.13). Likewise, the TOF PID cuts are varied, though only through a three cuts ($|n\sigma_{\mathrm{TOF}}| < 3$, $|n\sigma_{\mathrm{TOF}}| < 2.75$, and $|n\sigma_{\mathrm{TOF}}| < 2.5$). Again, the final correlation is found to vary by $\sim 1\%$.

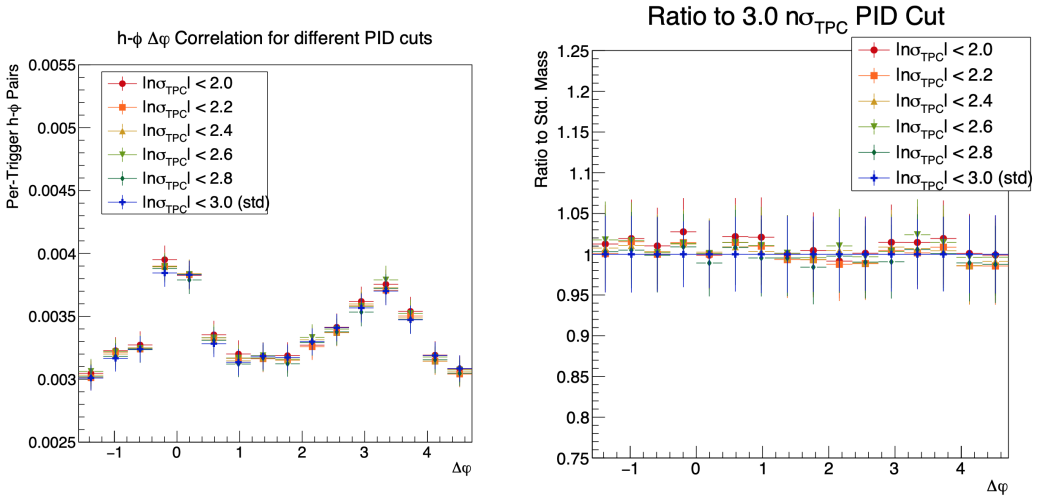

Figure 5.13: Effect of varying the PID cuts for the TPC detector from the standard cut of $|n\sigma_{\mathrm{TPC}}| < 3$ (left), along with the ratio of the correlation function using these variations to the standard cut (right).

5.3.2 Variation in m_{KK} Invariant Mass Regions

The mass peak range can be varied by widening and narrowing the $\phi(1020)$ signal region that is considered. Since this directly changes the signal/background ratio of the uncorrected $(h-KK)$ correlation, this variation tests whether or not the signal/background of the considered region has an appreciable effect on the final correlation shape. The fraction of total signal that is excluded because of the mass peak window is still taken into account and corrected with this variation (i.e. the correlation still must be corrected by the factor k_{Signal} from Eq. 3.6, which changes

with the mass window used). An invariant mass plot with the ϕ mass peak region (green) and the two sideband regions (gray) is included for reference in figure 5.14.

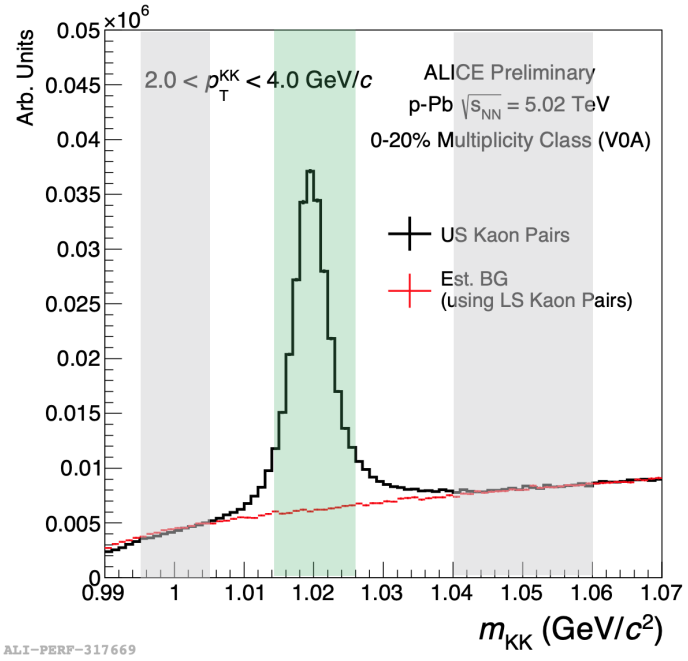

Figure 5.14: Invariant mass distribution of unlike-sign kaon pairs (black), with colored regions to show the ϕ mass peak region (green area) and the left and right sideband regions (grey area) that are used in the correlation analysis.

To test the mass peak selection, the invariant mass window used for the $\phi(1020)$ mass peak is varied in steps of $2\,\mathrm{MeV/c^2}$ between a widest cut $1.010 < m_{KK} < 1.030\,\mathrm{GeV/c^2}$ and a narrowest cut $1.015 < m_{KK} < 1.025\,\mathrm{GeV/c^2}$, which captures a range of 90% to 76% of the total ϕ signal. Within the range of variation considered, there is no significant effect on the shape of the correlation function due to the changing Signal/Background ratio (see figure 5.15). To estimate the size of this effect, the ratio of the correlation with varied cuts is taken to the correlation with the standard mass peak cut. The ratios for each $\Delta\varphi$ bin are then combined to find an RMS deviation of 1.4% for the mass peak cut variations.

Other cuts on the invariant mass distribution that are used in the measurement

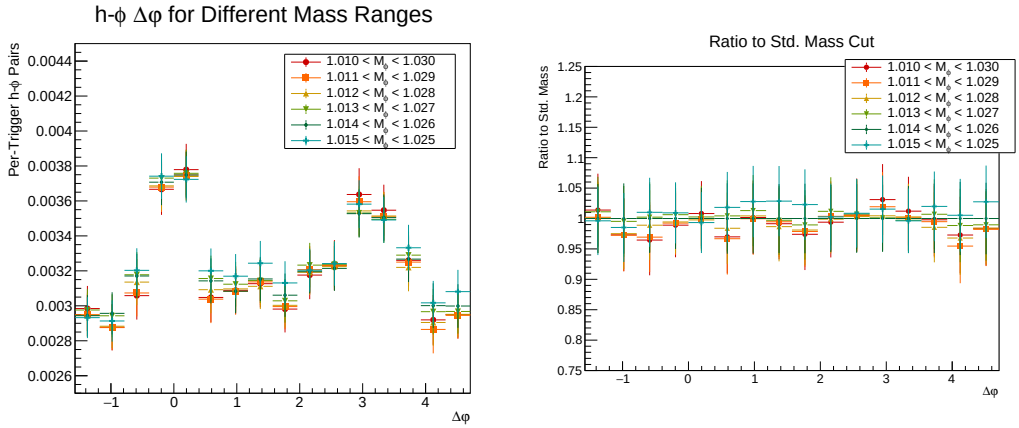

Figure 5.15: Effect of varying the ϕ mass peak region on the final $(h-\phi)$ correlation (left), and the ratio of each variation to the standard region of $1.014 < m_{KK} < 1.026\,\mathrm{GeV/c^2}$ (right).

procedure are in the sidebands, away from the $\phi(1020)$ mass peak. These sideband regions are used for both estimating the shape of the $(h-KK)$ background correlation underneath the mass peak, as well as for the calculation of the like-sign scaling factor. In order to make sure the choice of sideband region does not significantly change the final correlation structure, both the left and right sideband regions were varied from their standard ranges. The upper and lower limits of the two sideband regions were varied from their standard cuts of $0.995 < m_{KK} < 1.005\,\mathrm{GeV/c^2}$ for the left and $1.040 < m_{KK} < 1.060\,\mathrm{GeV/c^2}$ for the right by increments of $5\,\mathrm{MeV/c^2}$. In both cases, variation of the sideband region showed no significant changes to the correlation distribution, with a measured RMS of the deviation of $\sim 1\%$ (see figures 5.16 and 5.17). By taking the integral of the Voigtian fit of the mass peak, the unlike-sign kaon pairs within both sideband regions are calculated to contain much less than 1% of kaon pairs from ϕ decays, for all cut variations.

The final way that the invariant mass sideband region is used in the correlation procedure is to calculate the scaling factor k_{LS} in equation 3.6 needed to scale the

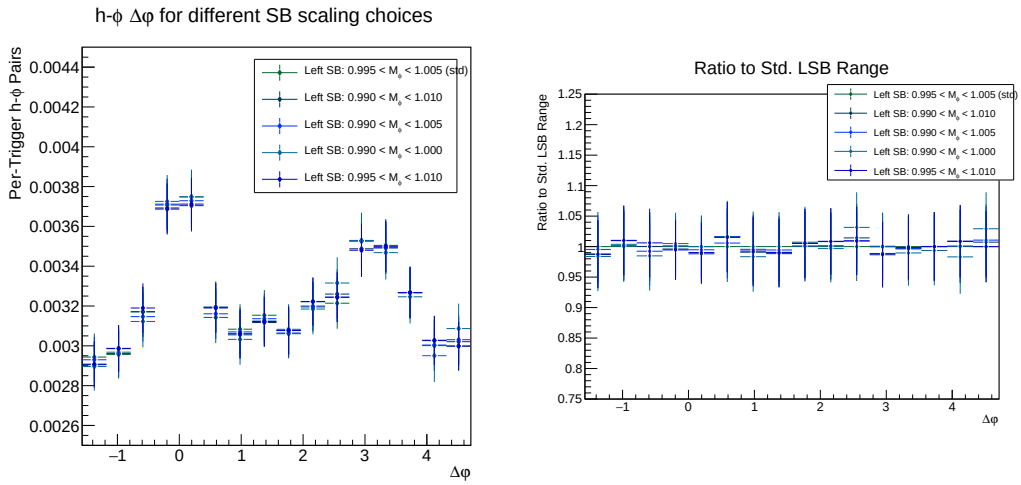

Figure 5.16: Effect of varying the left sideband (LSB) region of the invariant mass distribution on the final $(h-\phi)$ correlation (left), and the ratio of each variation to the standard region of $0.995 < m_{KK} < 1.005\,\mathrm{GeV/c^2}$ (right).

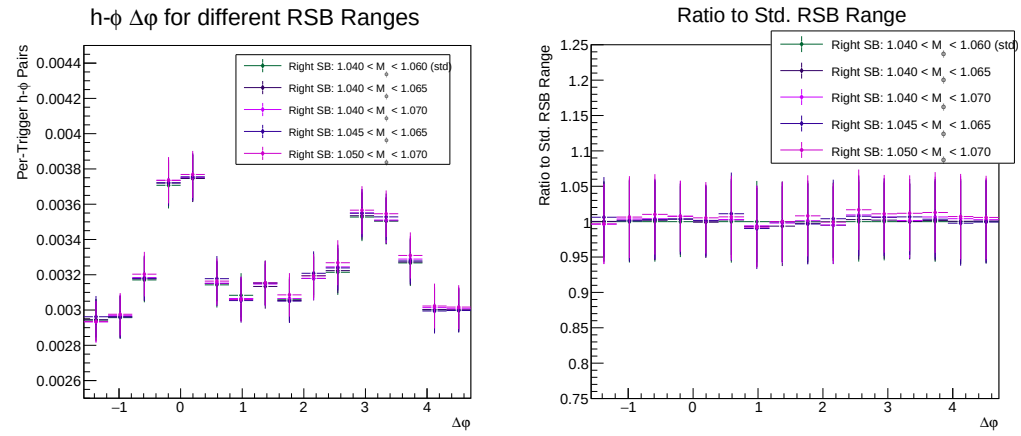

Figure 5.17: Effect of varying the right sideband (RSB) region of the invariant mass distribution on the final $(h-\phi)$ correlation (left), and the ratio of each variation to the standard region of $1.040 < m_{KK} < 1.060\,\mathrm{GeV/c^2}$ (right).

like-sign distribution to correctly estimate the combinatorial background under the $\phi(1020)$ mass peak. As this scale factor directly determines the baseline for the signal peak, variation in this value directly effects the final scale of the $(h-\phi)$ correlation function. This scale factor can be calculated in three different ways: by scaling the like-sign distribution to the integral of the unlike-sign in the left sideband region,

in the right sideband region, and to the integral of the unlike-sign in the sum of both sideband regions. The different choices of scaling region vary the final $(h-\phi)$ correlation by an RMS deviation of $\approx 2\%$ (see figure 5.18).

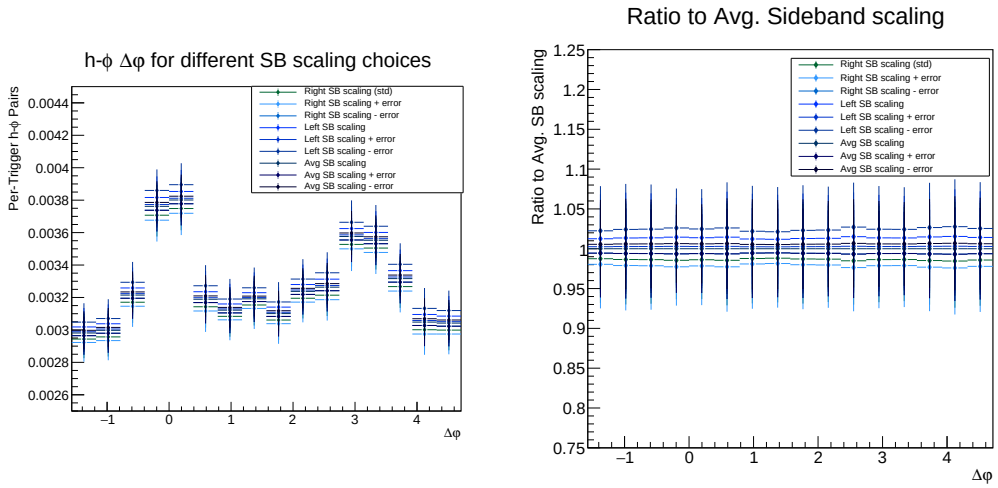

Figure 5.18: Effect of varying the normalization region used for estimating the combinatorial $(h-KK)$ background underneath the ϕ signal in the mass peak region (left), and the ratio to the standard method of averaging the scaling factor from the RSB and LSB together (right).

5.3.3 Investigation of Sideband Correlation Structure

The shape of the combinatorial background correlation is estimated by using the $(h-KK)$ correlations in the invariant mass sideband region. For the procedure outlined in section 3.3.1, the $(h-KK)$ correlation in the two sidebands is averaged together to estimate this background shape. However, since the right and left sidebands could select kaon pairs in slightly different kinematic regions, it is important to look at these sideband correlations individually as well. In order to visualize the differences of the correlation structure of the left and right sideband, the bin-by-bin difference between each 2D sideband correlation and the average of the two was plotted in units of bin statistical error (fig.5.19). The two methods using the different US

sidebands show only small difference to the average method used. This can be further checked by projecting the sideband correlations onto the $\Delta\varphi$ axis and normalizing them both to a total integral of 1 (see fig. 5.20). Again, this shows that within statistical fluctuations, the two sidebands have identical correlation structure. This gives confidence to the choice of averaging the two sidebands together in the standard measurement procedure.

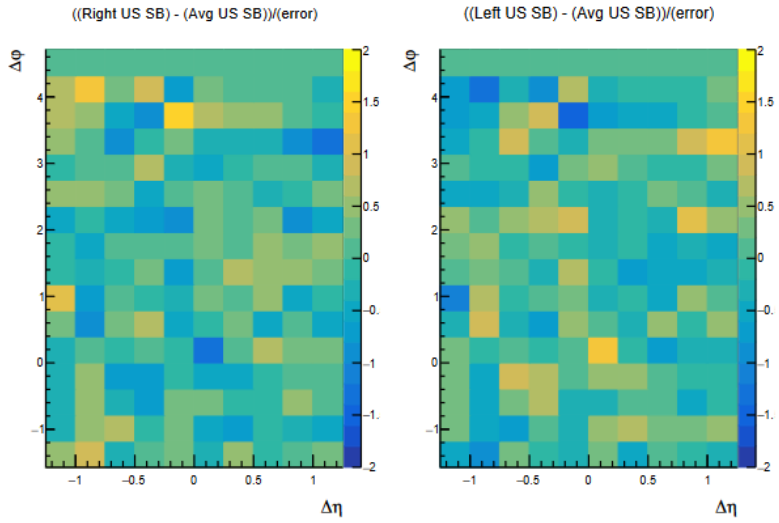

Figure 5.19: The bin-by-bin difference in between the 2D correlation shape in the left and right sidebands compared to the average of the two used in the standard procedure. These differences are plotted in units of the statistical uncertainty per $(\Delta\varphi, \Delta\eta)$ bin.

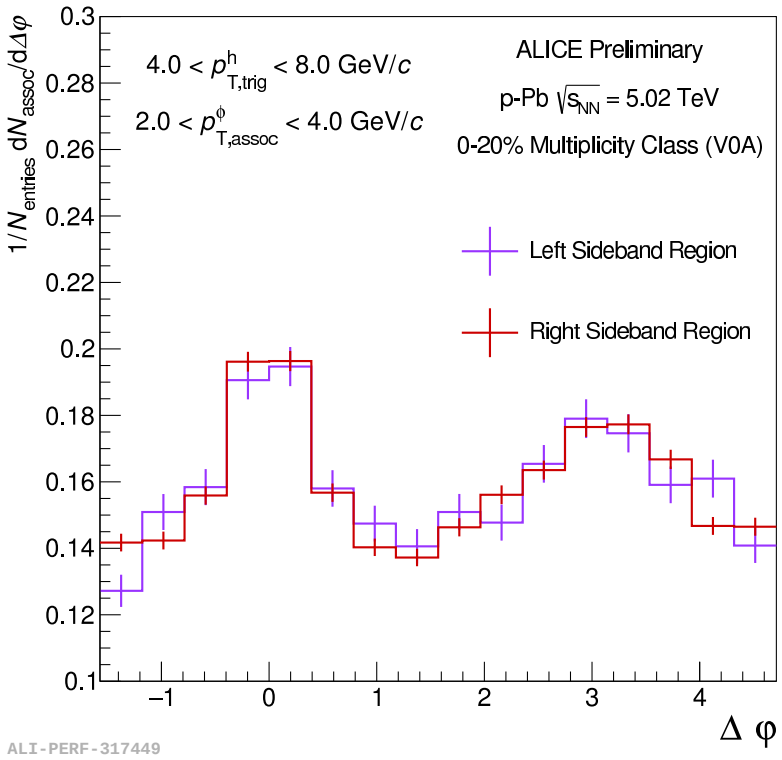

Figure 5.20: Comparison between the normalized 1D $(h-KK)$ correlation structures from the right (red) and left (pink) invariant mass sideband regions using unlike-sign kaon pairs.

Chapter Six: Results & Discussion

6.1 Jet-like $h-\phi$ Angular Correlations

For ease of reference, the full reconstructed $(h-\phi)$ correlation function, as derived in section 3.3.1, is repeated here:

$$C_{h-\phi}(\Delta\varphi,\Delta\eta) = k_{\text{Signal}}\Bigg(C_{\text{trig}}^{h-(KK)\ \text{Peak}}(\Delta\varphi,\Delta\eta) - \frac{k_{LS}}{2} * \left[\frac{1}{N_{Ent}^{LSB}} C_{\text{trig}}^{h-(KK)\ \text{LSB}}(\Delta\varphi,\Delta\eta) + \frac{1}{N_{Ent}^{RSB}} C_{\text{trig}}^{h-(KK)\ \text{RSB}}(\Delta\varphi,\Delta\eta)\right]\Bigg),$$

where each of the individual $C_{\text{trig}}(\Delta\varphi,\Delta\eta)$ functions are performed for a different m_{KK} invariant mass region, and are given by the equation

$$C_{trig}(\Delta\varphi,\Delta\eta) \equiv \frac{1}{N_{trig}^{corr}} \frac{1}{\varepsilon_{trig} * \varepsilon_{assoc}} \frac{ME(0,0) * S(\Delta\varphi,\Delta\eta)}{ME(\Delta\varphi,\Delta\eta)},$$

where the $S(\Delta\varphi,\Delta\eta)$ function is the same-event correlation, and the $ME(\Delta\varphi,\Delta\eta)$ is the mixed-event correlation. The trigger particle, as a proxy for a jet axis, is always required to be within the high momentum range $4.0 < p_{\text{T}}^{\text{trig}} < 8.0\,\text{GeV/c}$. The associated ϕ (or hadron) is split between a lower momentum range of $1.5 < p_{\text{T}}^{\text{assoc}} < 2.5\,\text{GeV/c}$, and a higher momentum range of $2.5 < p_{\text{T}}^{\text{assoc}} < 4.0\,\text{GeV/c}$.

From these two equations, it is clear that in order to calculate the reconstructed $(h-\phi)$ correlation within p-Pb collisions, six different measurements are required: same and mixed-event 2D correlations in the $\phi(1020)$ mass peak region, same and mixed-event correlations in the right sideband (RSB) mass region, and same and mixed-event correlations in the left sideband region (LSB).

To study the $\phi(1020)$ production as a function of system size, these six $(h-KK)$ measurements are carried out separately within three different charged particle mul-

tiplicity ranges, split based on multiplicity percentile: the 0-20% highest multiplicity events, the 20-50% highest multiplicity events, and the 50-80% highest multiplicity events. As previously mentioned, multiplicity percentile bins can also be converted to mean charged particle multiplicity $\langle N_{ch} \rangle$ in the range $|\eta| < 0.8$ and $p_{\mathrm{T}} > 0.2\,\mathrm{GeV/c}$. The values for the conversion to $\langle N_{ch} \rangle$ are presented again in table 6.1.

Multiplicity Pctl.	$\langle N_{ch} \rangle_{\lvert\eta\rvert<0.8}$
0-20%	49.1 ± 2
20-50%	29.3 ± 1.2
50-80%	15.3 ± 0.6

Table 6.1: Conversion between p-Pb multiplicity percentiles and the mean charged particle multiplicity, calculated for the range $|\eta| < 0.8$ and $p_{\mathrm{T}} > 0.2\,\mathrm{GeV/c}$ [99].

In order for the mixed-event correlation to accurately correct for the two particle acceptance of the detector, the pool of events for mixing must be grouped by similar event properties, specifically by the event multiplicity and by the primary vertex position in the longitudinal direction, Vtx_z. This is because if an event occurs at a large value of Vtx_z, the detector acceptance will be asymmetric in η, since the collision will have occurred closer to one end of the central barrel than the other. For this reason, both the same-event and mixed-event correlations are taken in 10 different bins within the range of $|\mathrm{Vtx}_z| < 10\,\mathrm{cm}$ (see table 6.2), for each of the three multiplicity bins. An example of these distributions can be seen in figure 6.1, while a closer look at the distributions for a single Vtx_z bin can be seen in figure 6.2.

The same-event correlation for each Vtx_z and multiplicity bin is then divided by the corresponding mixed-event distribution. After the mixed-event correction is performed, the corrected same-event correlations for each Vtx_z bin are combined together to give the full $C_{\mathrm{trig}}^{h-(KK)\ \mathrm{Peak}}(\Delta\varphi, \Delta\eta)$, $C_{\mathrm{trig}}^{h-(KK)\ \mathrm{LSB}}(\Delta\varphi, \Delta\eta)$, and $C_{\mathrm{trig}}^{h-(KK)\ \mathrm{RSB}}(\Delta\varphi, \Delta\eta)$ distributions. An example of these mixed-event corrected C_{trig}

Bin	Vtx_z min (cm)	Vtx_z max (cm)
0	-10	-8
1	-8	-6
2	-6	-4
3	-4	-2
4	-2	0
5	0	2
6	2	4
7	4	6
8	6	8
9	8	10

Table 6.2: The different bins in Vtx_z used for the mixed-event correction.

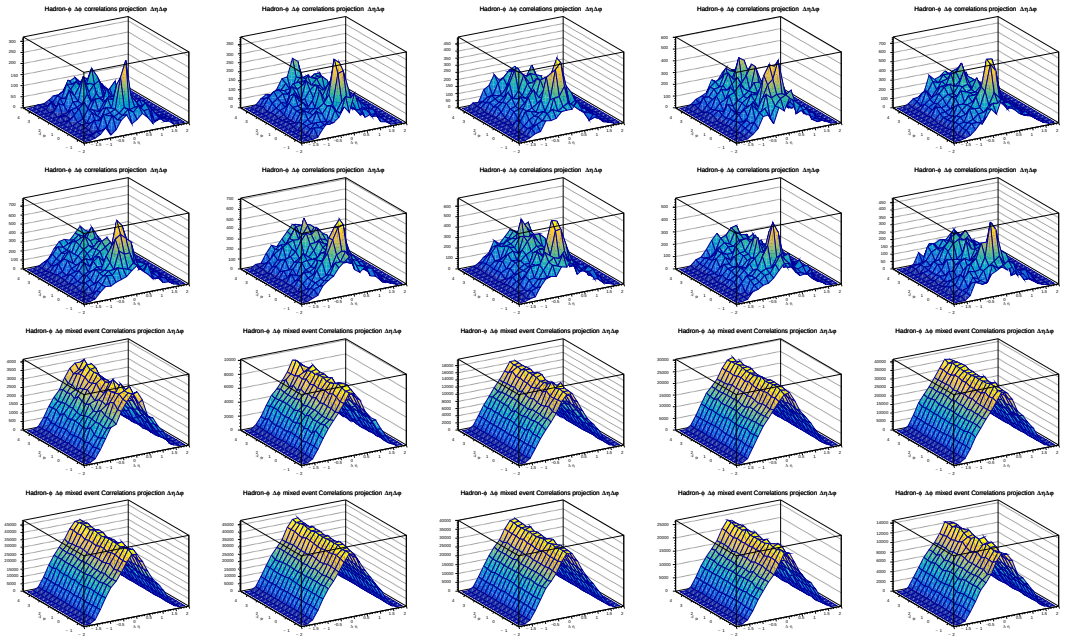

Figure 6.1: An example of 2D $(h-KK)$ correlations in the ϕ mass peak region, in the highest 0-20% multiplicity for different Vtx_z bins. This is using a trigger momentum of $4.0 < p_{\mathrm{T}}^{\mathrm{trig}} < 8.0\,\mathrm{GeV/c}$ and the higher associate momentum range $2.5 < p_{\mathrm{T}}^{\mathrm{assoc}} < 4.0\,\mathrm{GeV/c}$. The top two rows are the same-event distributions, while the bottom two are the mixed-event distributions. These are plotted from lowest Vtx_z bin=0 in the top left, increasing in Vtx_z bin from left to right, top to bottom.

distributions is shown in figure 6.3. The full collection of mixed-event corrected $(h-KK)$ distributions is presented in appendix A.

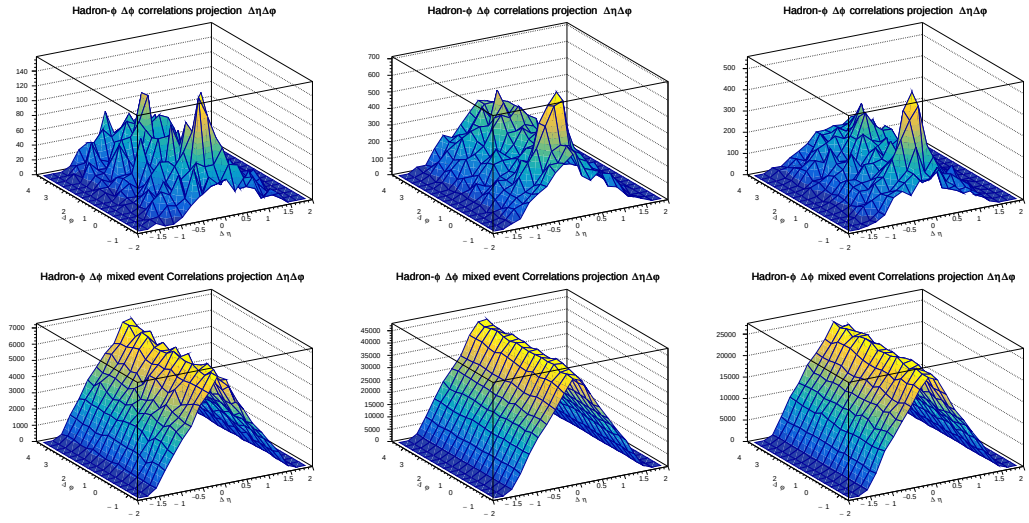

Figure 6.2: Same-event (top) and mixed-event (bottom) 2D $h-KK$ correlations for Vtx_z bin 6 in the highest 0-20% multiplicity range. This is using a trigger momentum of $4.0 < p_{\mathrm{T}}^{\mathrm{trig}} < 8.0\,\mathrm{GeV/c}$ and the higher associate momentum range $2.5 < p_{\mathrm{T}}^{\mathrm{assoc}} < 4.0\,\mathrm{GeV/c}$. From left to right, the correlations are being performed in the m_{KK} left sideband, $\phi(1020)$ mass peak, and right sideband regions

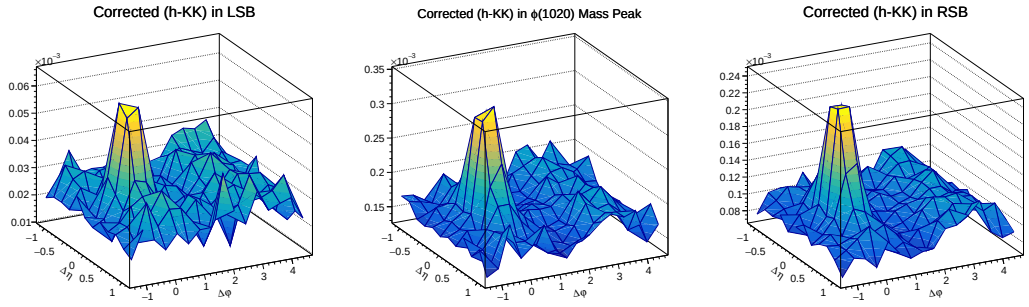

Figure 6.3: An example of mixed-event corrected $(h-KK)$ correlations for the 0-20% multiplicity, with a trigger momentum of $4.0 < p_{\mathrm{T}}^{\mathrm{trig}} < 8.0\,\mathrm{GeV/c}$ and in the higher associate momentum range $2.5 < p_{\mathrm{T}}^{\mathrm{assoc}} < 4.0\,\mathrm{GeV/c}$. Depicted are the correlations in the LSB (left), the $\phi(1020)$ mass peak (center), and the RSB (right) regions.

The correlations are split into two momentum ranges for the associate particle in order to further differentiate the $\phi(1020)$ production. With these two ranges, the $(h-\phi)$ correlation can be compared between a region with more hard-scattering production (higher momentum), and a region with more soft interactions (lower momentum), in addition to the separation that the differential jet-peak and underlying-

event yields give. Dihadron correlations are also measured for the same multiplicity and associate momentum ranges, using the same per-trigger correlation equation, $C_{\text{trig}}(\Delta\varphi, \Delta\eta)$. The final 2D $(h - \phi)$ and $(h - h)$ correlations for the two associate momentum ranges (across all three multiplicity classes) are shown in figures 6.4 and 6.5.

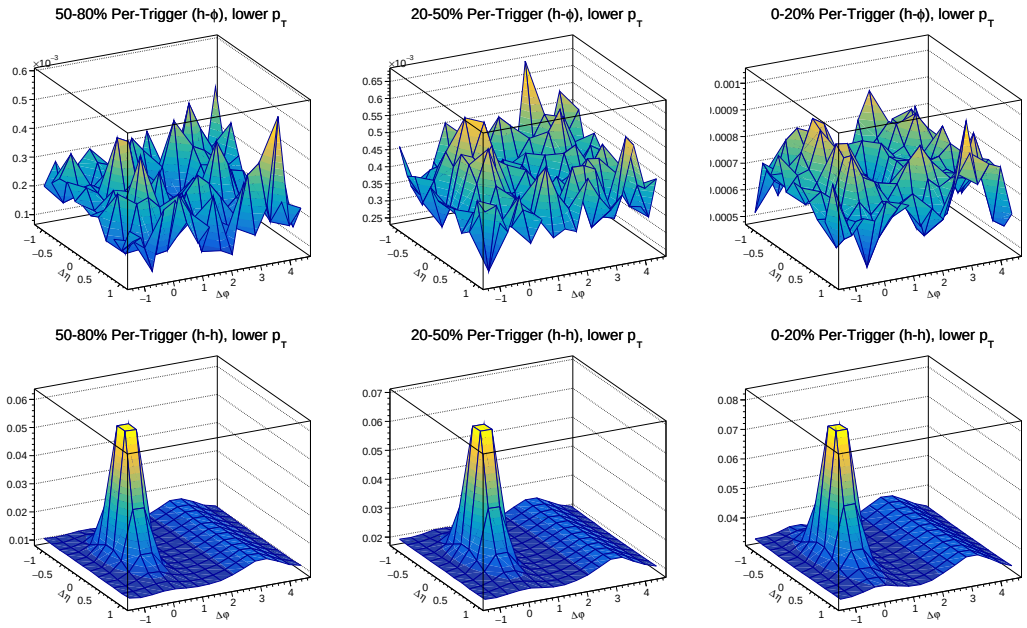

Figure 6.4: Final 2D angular correlations for the $(h - \phi)$ (top row) and $(h - h)$ (bottom row) for a trigger momentum of $4.0 < p_{\text{T}}^{\text{trig}} < 8.0\,\text{GeV/c}$ and the lower associate momentum range ($1.5 < p_{\text{T}}^{\text{assoc}} < 2.5\,\text{GeV/c}$). Correlations are shown for all three multiplicity bins, from lowest multiplicity (left) to highest multiplicity (right).

6.1.1 Per-trigger $(h - \phi)$ and $(h - h)$ $\Delta\varphi$ Correlations

After the full reconstruction procedure, the 2D correlations are then projected onto just the azimuthal $\Delta\varphi$ axis, giving the final one-dimensional per-trigger correlation results (see figures 6.6 through 6.9). These correlations are plotted such that the estimated underlying event is aligned across all multiplicities, and the scale of the

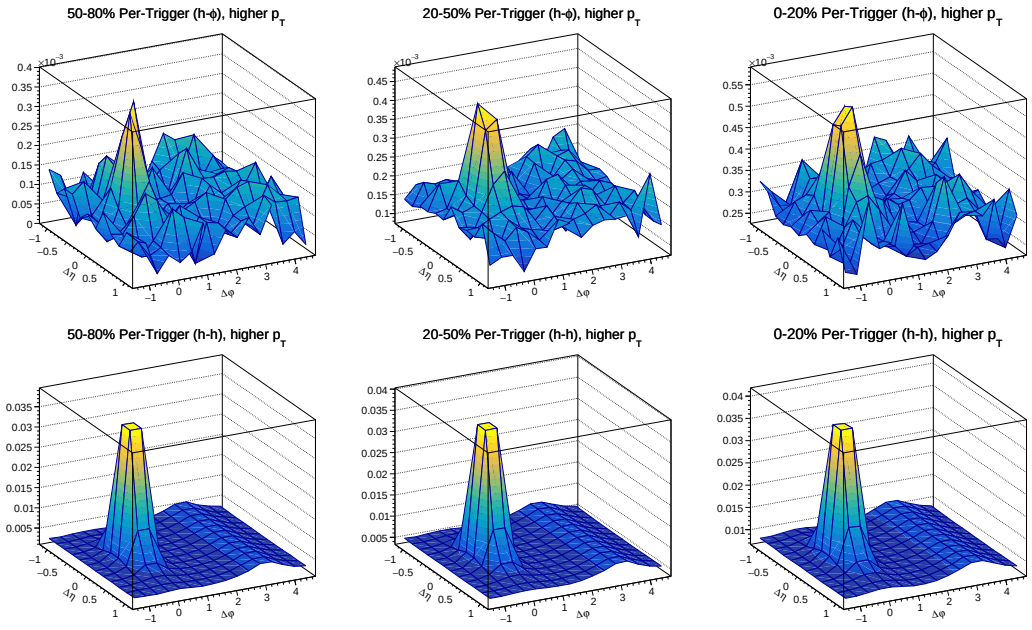

Figure 6.5: Final 2D angular correlations for the $(h-\phi)$ (top row) and $(h-h)$ (bottom row) for a trigger momentum of $4.0 < p_{\mathrm{T}}^{\mathrm{trig}} < 8.0\,\mathrm{GeV/c}$ and the higher associate momentum range $(2.5 < p_{\mathrm{T}}^{\mathrm{assoc}} < 4.0\,\mathrm{GeV/c})$. Correlations are shown for all three multiplicity bins, from lowest multiplicity (left) to highest multiplicity (right).

vertical axis is held constant for easy comparison. The systematic effect from varying the flat underlying event estimation is depicted as a grey band. The central flat UE value is depicted as a dashed line, while the charged hadron v_2 background assumption is depicted with a dotted line. For the dihadron correlations, the systematic uncertainty from variations in the flat underlying event estimation was small, and therefore excluded.

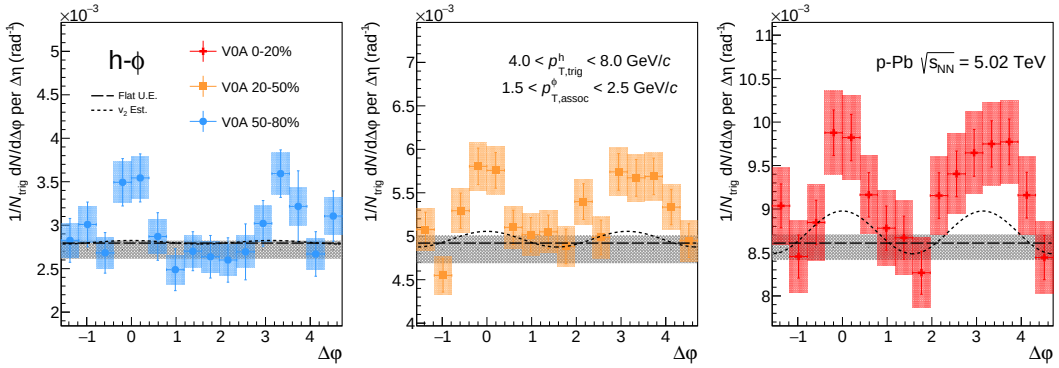

Figure 6.6: Per-trigger h-ϕ angular correlations for the lower associate $\phi(1020)$ p_{T} range, $1.5 < p_{\mathrm{T}}^{\phi} < 2.5\,\mathrm{GeV/c}$. The three multiplicity bins are plotted from low (left) to high (right) on the same scale axis, with offsets set to their respective underlying background estimation. The grey band shows the systematic range for the different flat background estimation methods.

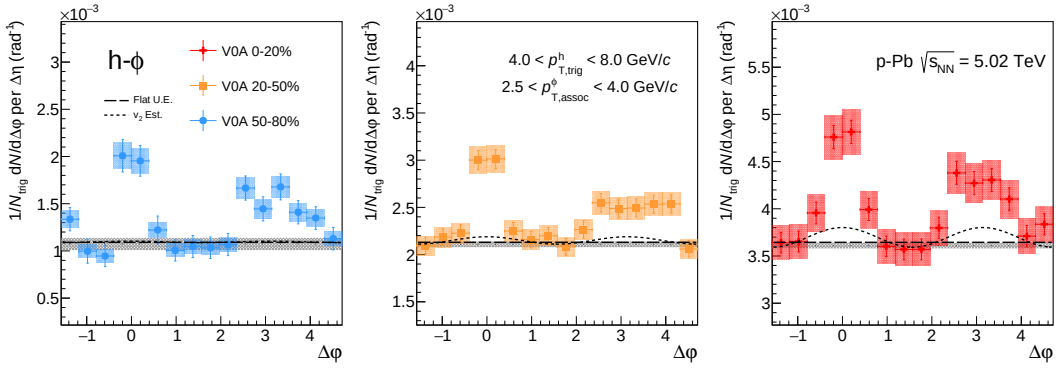

Figure 6.7: Per-trigger h-ϕ angular correlations for the higher associate $\phi(1020)$ p_{T} range, $2.5 < p_{\mathrm{T}}^{\phi} < 4.0\,\mathrm{GeV/c}$. The three multiplicity bins are plotted from low (left) to high (right) on the same scale axis, with offsets set to their respective underlying background estimation.

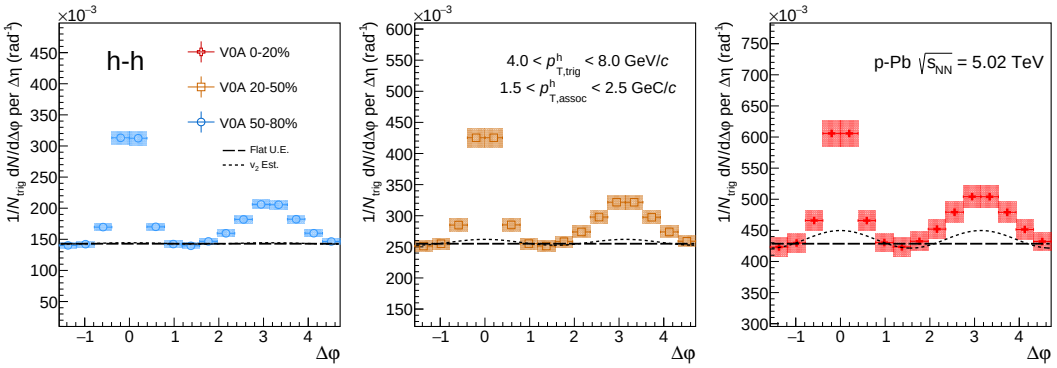

Figure 6.8: Per-trigger dihadron angular correlations for the lower associate p_{T} bin, $1.5 < p_{\mathrm{T}}^{h} < 2.5\,\mathrm{GeV/c}$. The three multiplicity bins are plotted from low (left) to high (right) on the same scale axis, with offsets set to their respective underlying background estimation.

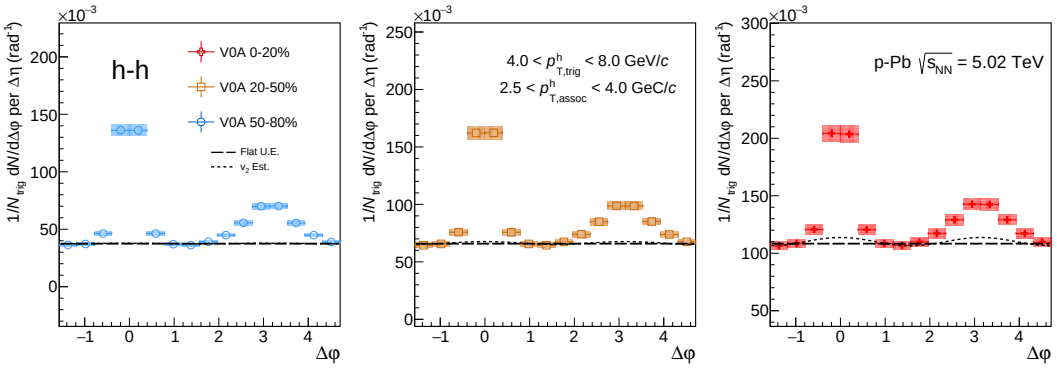

Figure 6.9: Per-trigger dihadron angular correlations for the higher associate p_{T} bin, $2.5 < p_{\mathrm{T}}^{h} < 4.0\,\mathrm{GeV/c}$. The three multiplicity bins are plotted from low (left) to high (right) on the same scale axis, with offsets set to their respective underlying background estimation.

6.2 Per-Trigger Yields of $h-\phi$ and $h-h$ pairs in Jets and the Underlying Event

As the main purpose of this analysis is to study the different regimes of $\phi(1020)$ production, the primary purpose of the measured per-trigger correlation function is to extract the approximate per-trigger $\phi(1020)$ yields. As a reminder of how the angular correlation space is divided into different regions, the cartoon representation from section 3.3.2 is repeated here in figure 6.10. First, the underlying event (UE) is established by averaging over the non-jet region ($-\pi/2 < \Delta\varphi < -\pi/4$, $\pi/4 < \Delta\varphi < 5\pi/8$, and $11\pi/8 < \Delta\varphi < 3\pi/2$ - corresponding to bins 1,2,7,8,9 and 16 on the $\Delta\varphi$ histograms, which have 16 bins in total). Once the UE is calculated, the jet yields are determined by integrating strictly above the UE between $-\pi/2 < \Delta\varphi < \pi/2$ for the near-side, and $\pi/2 < \Delta\varphi < 3\pi/2$ for the away-side.

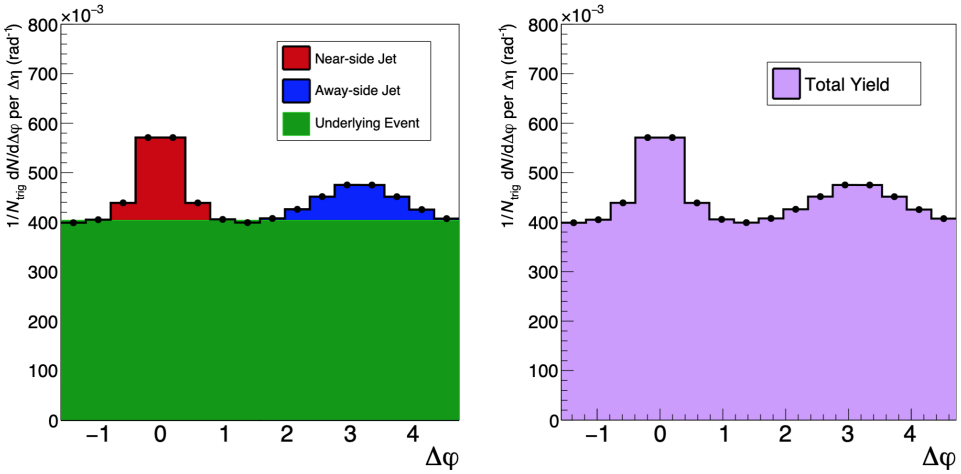

Figure 6.10: Example plot depicting the different regions of a dihadron angular correlation: the near-side jet (red), the away-side jet (blue), the underlying event (green), and the total pair yields (pink).

From the $\Delta\varphi$ correlations there appears to be a clear qualitative difference between

the structure of the $(h-h)$ correlations, where the near-side jet is both taller and more narrow than the away-side, and the $(h-\phi)$ correlations, where the near and away-side jets are closer to the same height, especially within the lower associate momentum range. To quantify that difference, the per-trigger jet yields within the near and away-side for both the $(h-\phi)$ and $(h-h)$ pairs are plotted as a function of mean charged particle multiplicity in figures 6.11 and 6.12. Due to the per-trigger scaling, these pairwise yields are good proxies for the actual $\phi(1020)$ and inclusive hadron per-trigger yields in the different event regions. The differences between the jet yields found using the flat UE value and the charged hadron v_2 estimation are depicted as shaded regions in the figures. While the effect of the v_2 on the yield grows with multiplicity, the near and away-side yields are affected by similar amounts, and therefore any comparisons between the behaviour of the near and away-side are independent of the background v_2 assumption. Percent increases of the jet yields from low to high multiplicity are presented in table 6.3 for both momentum ranges, with the increase for the yields with the charged hadron v_2 assumption quoted in parentheses.

Several features of these jet yields are of immediate interest. The dihadron near-side yields are roughly a factor of 2 higher than the away-side yields for both momentum ranges, and are roughly independent of the event multiplicity. On the other hand, the $(h-\phi)$ near and away-side yields are much closer to each other. For the higher momentum region, the $(h-\phi)$ yields in the near and away-side are nearly identical and, within statistical errors and the v_2 systematic, show no increase with event multiplicity. For the lower momentum region, however, the $(h-\phi)$ yields for the near and away-side both increase significantly with multiplicity. Moreover, the increase of the away-side yield with multiplicity is greater than the near-side yield.

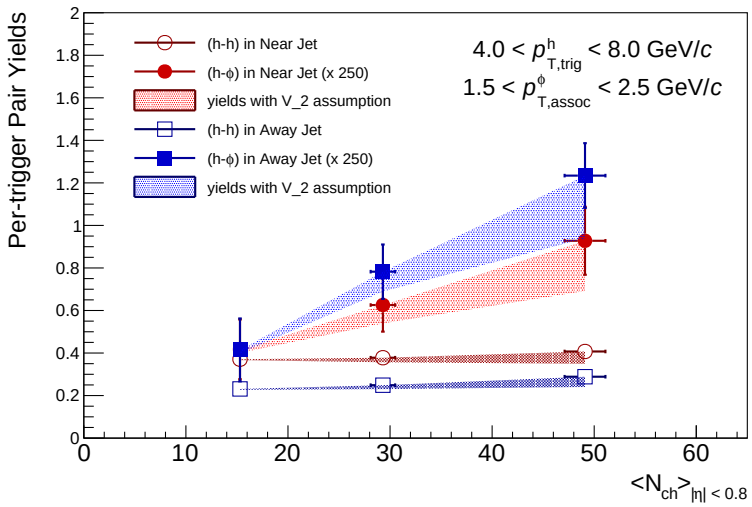

Figure 6.11: Per-trigger near-side (red) and away-side (blue) yields for the lower momentum range for both the $(h-\phi)$ (full points) and $(h-h)$ (open points). The $(h-\phi)$ yields are scaled by a factor of 250 for ease of comparison. The shaded band represents the difference between the flat UE estimation and using the charged hadron v_2 assumption.

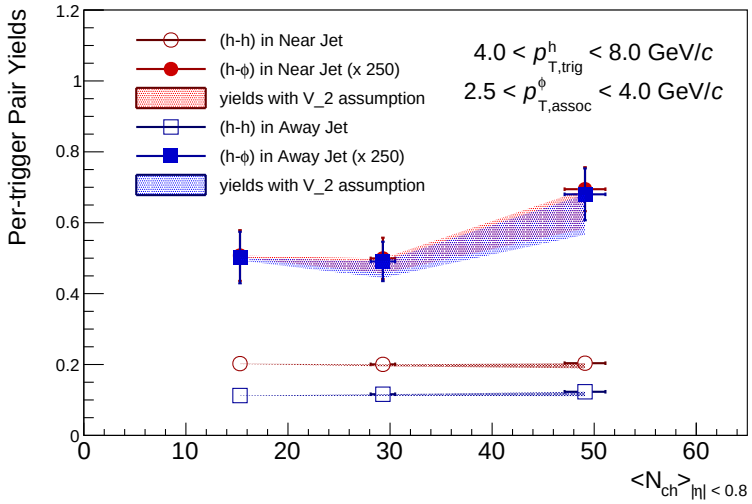

Figure 6.12: Per-trigger near-side (red) and away-side (blue) yields for the higher momentum range for both the $(h-\phi)$ (full points) and $(h-h)$ (open points). The $(h-\phi)$ yields are scaled by a factor of 250 for ease of comparison. The shaded band represents the difference between the flat UE estimation and using the charged hadron v_2 assumption.

Lower associate momentum: $1.5 < p_T < 2.5\,\mathrm{GeV/c}$

Region	% Change from Low to High Mult. (Change with v_2 Effect)
$(h-\phi)$ near-side	122.3% ± 84.08% (75.1% ± 73.13%)
$(h-\phi)$ away-side	197.7% ± 112.48% (138.9% ± 96.50%)
$(h-h)$ near-side	9.8% ± 5.67% (-6.0% ± 4.68%)
$(h-h)$ away-side	24.8% ± 6.68% (3.5% ± 5.55%)

Higher associate momentum: $2.5 < p_T < 4.0\,\mathrm{GeV/c}$

Region	% Change from Low to High Mult. (Change with v_2 Effect)
$(h-\phi)$ near-side	36.9% ± 22.86% (17.5% ± 20.85%)
$(h-\phi)$ away-side	35.5% ± 24.45% (15.7% ± 22.56%)
$(h-h)$ near-side	0.6% ± 5.21% (-6.7% ± 4.84%)
$(h-h)$ away-side	9.5% ± 5.92% (-1.6% ± 5.32%)

Table 6.3: The percent change from low to high multiplicity for the near and away-side $(h-\phi)$ and $(h-h)$ yields for the lower (top) and higher (bottom) momentum ranges. The percent changes for the yields using the charged hadron v_2 for the UE are presented in parentheses.

The observed increase in the $\phi(1020)$ jet yields is initially a surprising result. In high multiplicity heavy-ion collisions, interactions between a high p_{T} parton and a strong QGP medium act to strongly reduce the particle yields on the away-side, while the near-side yield, due to the selection criteria of a high momentum trigger hadron, remains relatively unchanged. However, as mentioned previously in section 1.5.4, jet measurements from ALICE have shown that there are no significant jet-quenching effects observed in p-Pb collisions. These studies suggest whatever interactions occur between jets and the QGP medium in small systems do not lead to either a significant jet energy loss or a decrease in particle production. However, this finding does not rule out other interactions between a jet and a QGP medium that may change the jet fragmentation or hadrochemistry, without significantly reducing its energy.

The increase of the yield on the away-side may hint at interactions occurring between high p_{T} partons and a partonic medium that change the jet fragmentation in favor of the $\phi(1020)$ meson in high multiplicity p-Pb events (i.e. radiated gluons

splitting to produce strange quark/antiquark pairs). The change in the near-side jet yield with multiplicity, while only a 1 sigma effect taking into account the v_2 systematic, also has interesting implications. Selecting a high momentum trigger is typically thought to bias the near-side jet towards unmodified jet fragmentation, and this would be expected to give particle yields that are independent of event multiplicity. However, this selection effect is most significant when jet-quenching is present, since the energy-loss is what causes the near-side to preferentially consist of those jets with a small path-length through the QGP medium. In the case without significant jet-quenching, it is possible that the same interactions acting to increase the away-side yield are also present for the near-side jet as well. The observed trend that the near-side $\phi(1020)$ yields do not increase as much as the away-side yields may point to a small path-length effect for this ϕ enhancement, or may be partly due to an energy balancing effect due to requiring the high energy trigger particle to be in the near-side jet.

In addition to the jet yields, similar yield measurements can be made for the $(h-\phi)$ and $(h-h)$ pair yields within the underlying event (see figure 6.13. However, these individual per-trigger yields contain somewhat different information on the multiplicity dependence than the jet yields do. As can be seen the $\Delta\varphi$ correlations, the majority of all associated particles are coming from the underlying event, with the jets contributing only a small amount to the total number of pairs. This means that when higher multiplicity events are selected, this necessarily selects for events with a larger underlying event. Considering that the dihadron jet yields are flat across multiplicity, the UE yield measurement for the dihadron pairs is essentially measuring multiplicity in the associate momentum range vs. multiplicity in the $p_{\mathrm{T}} > 0.2\,\mathrm{GeV/c}$. For the $(h-\phi)$ UE yields, similar behavior is seen, where the vast majority of the

$\phi(1020)$ are coming from the underlying event rather than the jets. Again we see that as multiplicity increases, the underlying event yields increase with it.

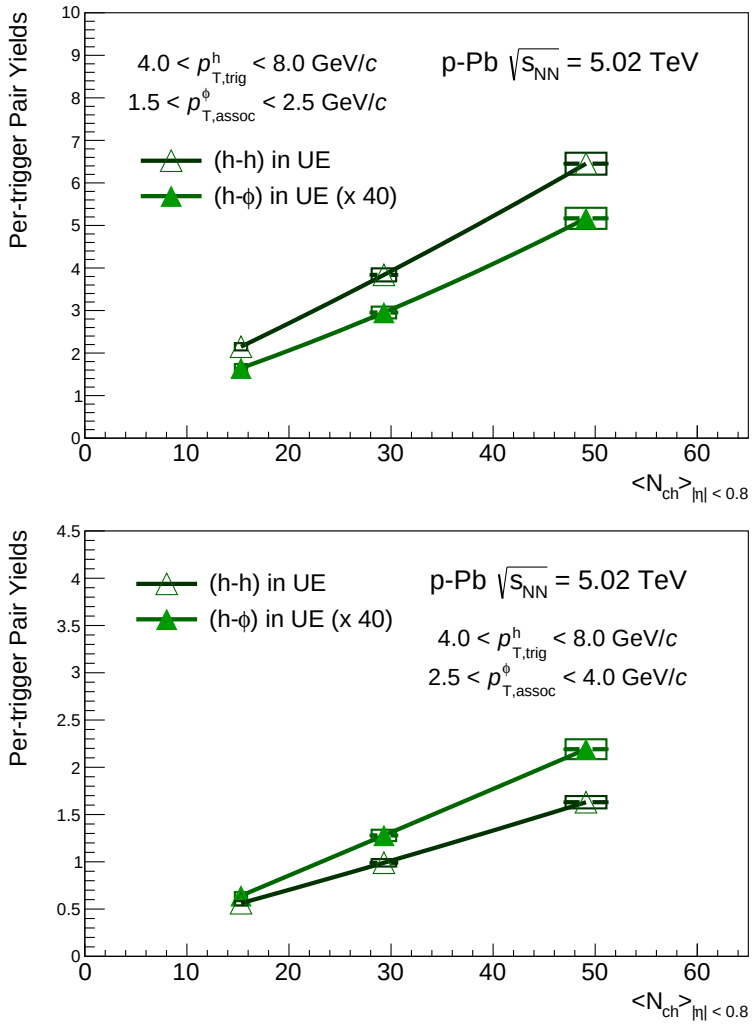

Figure 6.13: Per-trigger yields for $(h-\phi)$ and $(h-h)$ within the underlying event (UE) as a function of multiplicity for the lower (top) and higher (bottom) associate momentum region. Both the ϕ and hadron yields show a sharp increase as a function of multiplicity. This reflects the fact that the majority of the total event production is from within the UE, and thus as total multiplicity increases, yields within the UE must increase as well.

6.3 ϕ/h Production Ratios Within Jets and the Underlying Event

While changes in the per-trigger jet yields point to interesting changes to the jet fragmentation, in order to look at strangeness enhancement it is necessary to look at the strange over non-strange production ratio. For reference, previously observed enhancement of the momentum integrated ϕ/π ratio is presented here again in figure 6.14. However, the measured values of this ϕ/π ratio cannot be directly compared to the values measured by the $(h-\phi)/(h-h)$ ratio for several reasons. First, the correlation ratio measurement takes the ratio to inclusive hadrons, rather than to charged pions, and the measured ϕ/π ratios are integrated over all momentum, while the correlation measurement is for specific momentum regions. Second, the nature of the correlation measurement chooses only those events that contain a high p_{T} trigger, thereby slightly changing the event pool makeup compared to collection of minimum bias events. For these reasons, the presented ϕ/pi ratio should be taken as an illustrative example, demonstrating the overall effect of strangeness enhancement across multiplicity.

By taking the yields presented in the previous section and dividing the $(h-\phi)$ yields by their dihadron yield counterparts, the underlying ϕ/h ratio can be measured in different production regions. These ratios are presented in figures 6.15 and 6.16 as a function of event multiplicity for the lower and higher associate momentum ranges, and reported in table 6.4. The ratios are separated into the four areas of the correlation: in the near-side jet (red points), in the away-side jet (blue), in the underlying event (green), and the total ϕ/h ratio (magenta). Similar to the jet yield measurements, the systematic effect that the charged hadron v_2 has on the ratio is

depicted as the shaded grey region. Due to the fact that the v_2 has effects of similar magnitude to both the dihadron and $(h-\phi)$ background estimation, this systematic is significantly smaller for the ratio than for the individual jet yield measurements.

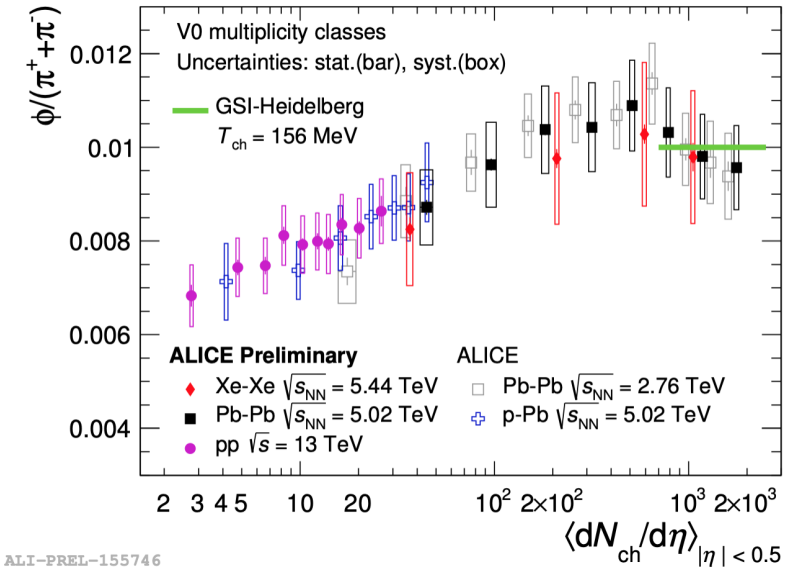

Figure 6.14: The momentum integrated ϕ/π ratio plotted as a function of event charged particle multiplicity. This ratio increases smoothly across a wide range of multiplicities, with no dependence on the specific collision system studied. Figure from ALICE.

Lower associate momentum: $1.5 < p_T < 2.5\,\mathrm{GeV/c}$

Event Region	50-80% Mult. Pctl.	20-50% Mult. Pctl.	0-20% Mult. Pctl.
ϕ/h Near-Side	0.45e-2 ± 0.15e-2 (± 0.07e-2)	0.66e-2 ± 0.13e-2 (± 0.07e-2)	0.91e-2 ± 0.16e-2 (± 0.08e-2)
ϕ/h Away-Side	0.72e-2 ± 0.26e-2 (± 0.09e-2)	1.26e-2 ± 0.21e-2 (± 0.11e-2)	1.71e-2 ± 0.21e-2 (± 0.20e-2)
ϕ/h in U.E.	1.91e-2 ± 0.03e-2 (± 0.14e-2)	1.92e-2 ± 0.01e-02 (± 0.12e-3)	2.00e-2 ± 0.01e-02 (± 0.13e-3)
ϕ/h Total	1.62e-2 ± 0.04e-2 (± 0.11e-2)	1.78e-2 ± 0.02e-2 (± 0.11e-2)	1.93e-2 ± 0.01e-2 (± 0.12e-2)

Higher associate momentum: $2.5 < p_T < 4.0\,\mathrm{GeV/c}$

Event Region	50-80% Mult. Pctl.	20-50% Mult. Pctl.	0-20% Mult. Pctl.
ϕ/h Near-Side	1.00e-2 ± 0.14e-2 (± 0.15e-2)	1.00e-2 ± 0.12e-2 (± 0.10e-2)	1.36e-2 ± 0.12e-2 (± 0.12e-2)
ϕ/h Away-Side	1.79e-2 ± 0.26e-2 (± 0.23e-2)	1.69e-2 ± 0.19e-2 (± 0.15e-2)	2.21e-2 ± 0.24e-2 (± 0.26e-2)
ϕ/h in U.E.	2.85e-2 ± 0.05e-2 (± 0.20e-2)	3.23e-2 ± 0.01e-2 (± 0.20e-2)	3.36e-2 ± 0.01e-2 (± 0.21e-2)
ϕ/h Total	2.29e-2 ± 0.06e-2 (± 0.16e-2)	2.75e-2 ± 0.03e-2 (± 0.17e-2)	3.08e-2 ± 0.02e-2 (± 0.19e-2)

Table 6.4: Pairwise ratio of (h-ϕ)/(h-h) within the near-side jet, away-side jet, underlying event, and total ratio from low multiplicity (left) to high multiplicity (right) p-Pb collisions, for lower associate p_T (top) and higher associate p_T (bottom). Systematic errors are shown in parentheses.

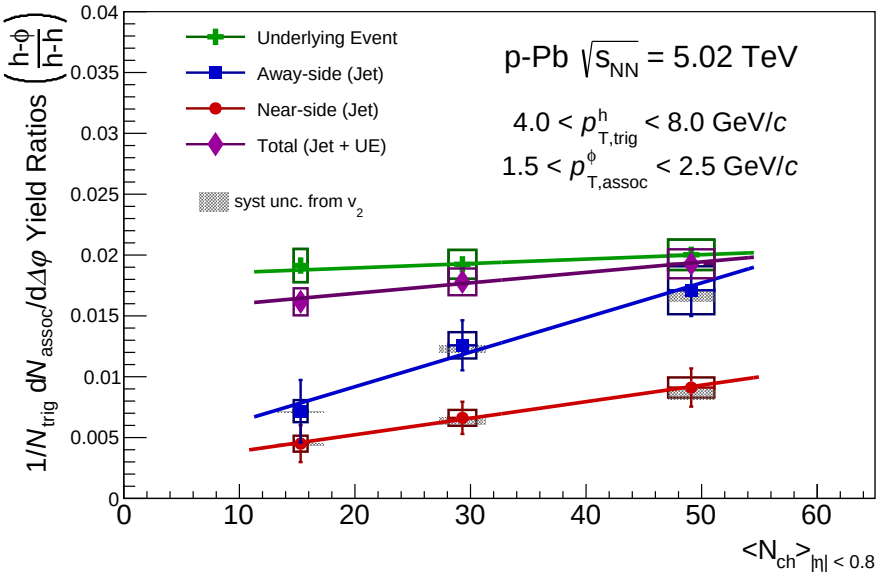

Figure 6.15: Per-trigger ϕ/h pair ratios in the near-side (red), away-side (blue), underlying event (green), and the total ratio (magenta) for the lower momentum range. The shaded grey band represents the difference between the ratio using the flat UE estimation and using the charged hadron v_2 estimate.

One of the primary observations of this differential ϕ/h ratio is in the consistent separation of the ratio within the underlying event and the ratio within the jet regions. In fact, for both momentum ranges and all multiplicities, the ϕ/h ratio in the near-side jet is the smallest, followed by the ratio in the away-side jet, while the ϕ/h ratio in the UE is significantly higher than in either jet. The total ϕ/h ratio, being essentially a weighted average between the ratio in the UE and the ratio in the jets, lies in-between the two. This persistent feature points to a clear difference in the ϕ/h production within jets and within the softer interactions in the underlying event. Somewhat surprisingly, the ϕ/h ratio within the UE is essentially independent of event multiplicity for both momentum ranges. This suggests that the mechanism that causes the enhanced ϕ/h ratio within the UE, and therefore drives the total ϕ/h ratio, is present in even low-multiplicity events. In terms of a toy QGP model, this

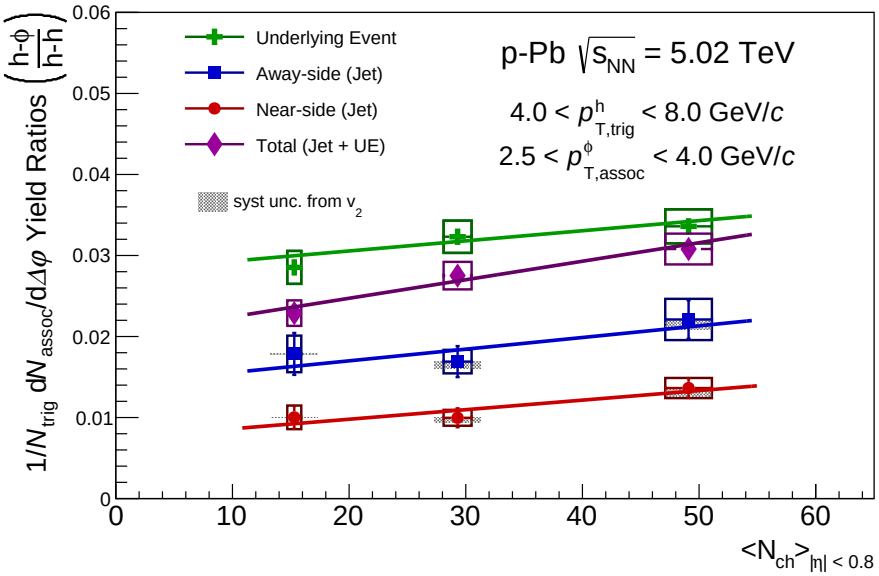

Figure 6.16: Per-trigger ϕ/h pair ratios in the near-side (red), away-side (blue), underlying event (green), and the total ratio (magenta) for the higher momentum range. The shaded grey band represents the difference between the ratio using the flat UE estimation and using the charged hadron v_2 estimate.

could be explained as a volume dependent effect: the UE yields scale with the volume of the QGP medium, while the in-medium production processes are only dependant on the existence of the medium rather than its size, leading to a ϕ/h ratio within the UE that is constant. However, this explanation relies on the existence of a QGP medium in even low multiplicity p-Pb collisions, an assumption that is still difficult to explain theoretically.

Another distinct feature of the ϕ/h ratios is the difference between the behavior in the higher and lower momentum range. This difference can be quantified by looking at a linear fit of the yields as a function of multiplicity for the higher and lower momentum ranges (see table 6.5). For the higher momentum range, the ratios within different regions show roughly the same increase as multiplicity increases. For the lower momentum range, however, we see a slight difference in the slopes of the ratio

in the underlying event region and the behavior of the ratios within the jet region. Moreover, in the lower momentum range we see an approximately 1 sigma difference between the increase within the near-side and the away-side regions, with the away-side ratio showing substantially more enhancement.

Linear fit of (h-ϕ)/(h-h) ratio vs. $\langle N_{ch} \rangle$		
Associate momentum: $1.5 < p_T < 2.5\,\mathrm{GeV/c}$		
Event Region	Fit Slope (Fit Slope with v_2)	χ^2/ndf
Near-Side	1.36e-4 ± 0.65e-4 (1.11e-4 ± 0.65e-4)	0.015
Away-side	2.84e-4 ± 0.98e-4 (2.63e-4 ± 0.98e-4)	0.225
U.E.	0.36e-4 ± 0.05e-4	1.88
Total	0.86e-4 ± 0.12e-4	1.22
Associate momentum: $2.5 < p_T < 4.0\,\mathrm{GeV/c}$		
Near-Side	1.18e-4 ± 0.54e-4 (0.88e-4 ± 0.54e-4)	1.03
Away-side	1.44e-4 ± 1.02e-4 (1.13e-4 ± 1.02e-4)	1.05
U.E.	1.25e-4 ± 0.24e-4	21.4
Total	2.29e-4 ± 0.26e-4	6.03

Table 6.5: Fit parameters for the differentiated $(h-\phi)/(h-h)$ ratios vs. $\langle N_{ch} \rangle$ in the two different associate momentum ranges. Values in parentheses represent the fits with the yield ratios calculated using the charged hadron v_2 assumption for both the $(h-\phi)$ and $(h-h)$ correlations.

The large difference in the ϕ/h ratio in the jets and UE has an interesting effect on the total ϕ/h ratio as a function of multiplicity. Plotting the percent of the total $(h-\phi)$ pairs that come from jets shows a clear trend as a function of event multiplicity (see figure 6.17). From the dihadron yields, it is seen that at low multiplicities, jet production makes up roughly 40% (20%) of produced hadrons in the higher (lower) momentum range. This fraction then falls as multiplicity increases, until at the highest multiplicity, jet production only makes up roughly 20% (10%) of the produced hadrons in the higher (lower) momentum range. Since the total of $(h-\phi)$ or $(h-h)$ pairs is simply jets plus UE, the total $(h-\phi)/(h-h)$ ratio can be written as a

weighted average:

$$\left(\frac{h-\phi}{h-h}\right)_{\text{Total}} = f * \left(\frac{h-\phi}{h-h}\right)_{\text{Jets}} + (1-f) * \left(\frac{h-\phi}{h-h}\right)_{\text{UE}} \tag{6.1}$$

where f is the fraction of $(h-h)$ pairs that come from jets (i.e. $(h-h)_{\text{Jets}}/(h-h)_{\text{Total}}$). This means that since the jet vs. non-jet makeup of the event (encapsulated in f) decreases as multiplicity increases, the total ϕ/h ratio will shift from lower (closer to the ratio in jets) at low multiplicity, to higher (closer to the ratio in the UE) at high multiplicity. This gives a new "event make-up" mechanism for the smooth increase in the total ϕ/h ratio: even if the underlying production in the jet and UE are relatively flat as a function of multiplicity, the decreasing fraction f will increase the total ϕ/h ratio as multiplicity increases.

To better understand the behavior seen within the differential ϕ/h ratios, it is useful to compare the measured p-Pb ϕ/h ratio to model predictions. For this comparison, the presented ratios in p-Pb are compared with the same ratios calculated in simulated pp events using the event generator PYTHIA. The simulated events were generated with the Monash 2013 tune[114], and were anchored to real pp collision data measured in ALICE in 2017. Briefly, PYTHIA is Monte Carlo event generator that uses wide variety of measured scattering cross sections, along with perturbative QED and QCD calculations, to simulate a number of different scattering processes. Since it primarily relies on perturbative methods, it cannot simulate the soft regions of momentum transfer where the strong coupling blows up. However, it does include many complicated phenomena, including multi-parton interactions, resonance regeneration and rescattering, and non-perturbative string fragmentation. In this way, it is a useful tool for studying regimes where high momentum transfers are expected, such as high energy pp collisions.

In the context of this analysis, PYTHIA presents a useful way to study the produc-

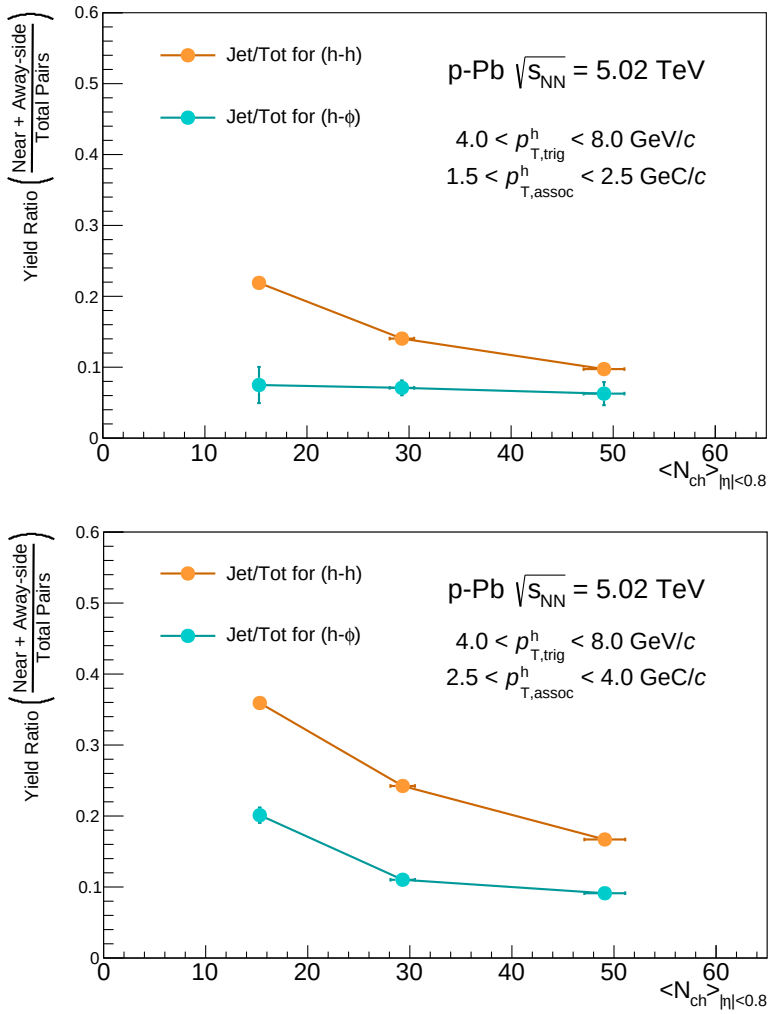

Figure 6.17: The fraction of per-trigger pairs that come from within the near and away-side jet peaks for the lower (top) and higher (bottom) associated momentum ranges. As multiplicity increases, the fraction of pairs that come from jets decreases significantly

tion ratio of ϕ/h in a system explicitly lacking a collective QGP phase in the evolution of the collision. The $(h-\phi)$ correlations in PYTHIA are measured in the same method used in the "truth" measurement of the Monte Carlo closure tests, described in section 5.1. Here the ϕ are selected directly, rather than being reconstructed from their decay children, and are then correlated with real trigger hadrons. The rest of the analysis proceeds in exactly the same way as the p-Pb analysis. In addition, the di-

rect ϕ/h ratio in PYTHIA was calculated by looking at the primary charged hadrons and the ϕ in events that contained a trigger hadron directly, without performing the per-trigger correlation. For both the lower and higher momentum associate regions, the direct ϕ/h ratio was measured to be within 1% of the total $(h-\phi)/(h-h)$ ratio, again confirming the ability of the per-trigger correlation measurement to recover the underlying ϕ/h yield ratios.

The final PYTHIA pair-wise $h-\phi/h-h$ ratio can be seen plotted against the p-Pb measurement as the open points in figures 6.18 and 6.19. While a significant multiplicity dependence was not expected, the PYTHIA events were separated into 0-20% and 20-80% multiplicity percentile bins in order to cross-check this assumption. Simple linear fits between the two multiplicity bins are plotted as dashed lines.

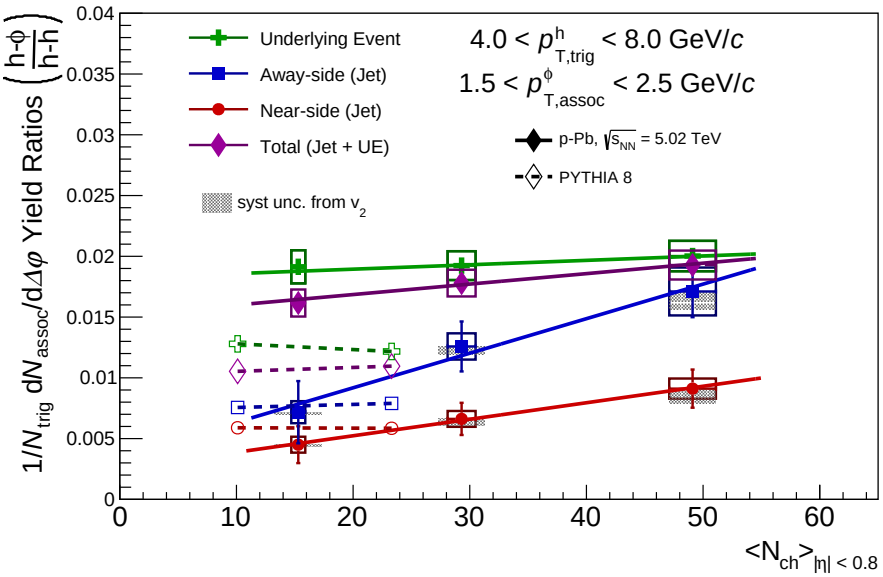

Figure 6.18: Pairwise ϕ/h ratio vs $\langle N_{ch} \rangle$ for the lower associated momentum range $1.5 < p_T < 2.5 GeV/c$. Ratios from p-Pb data are depicted with solid points, while ratios from simulated pp PYTHIA events are depicted as open points.

Comparing the ratios between model and data shows that the ratio within the near and away-side jets for low multiplicity p-Pb events is consistent with the PYTHIA

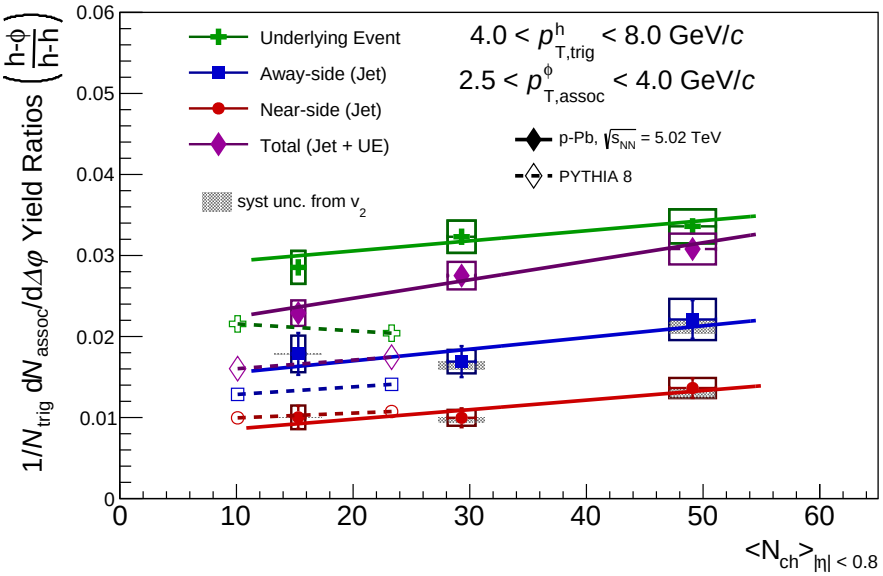

Figure 6.19: Pairwise ϕ/h ratio vs $\langle N_{ch} \rangle$ for the higher associated momentum range $2.5 < p_T < 4.0 GeV/c$. Ratios from p-Pb data are depicted with solid points, while ratios from simulated pp PYTHIA events are depicted as open points.

prediction, for both momentum ranges considered. This suggests that the jet production in low multiplicity p-Pb is well described by the perturbative, non-collective physics contained in PYTHIA. Interestingly, PYTHIA does still exhibit an ordering of ϕ/h production, where the production ratio in the jets is lower than in the non-jet event. This suggests that at least part of this ratio ordering seen in p-Pb collisions may be explained by more standard QCD physics, rather than collective phenomena.

However, the ratio in the underlying event - and therefore in the total ratio - is significantly under-predicted in PYTHIA compared to even low multiplicity p-Pb collisions. Since the observed strangeness enhancement in p-Pb collisions can be partly understood as an "event make-up" effect, the lower UE ratio in PYTHIA directly leads to the under-prediction of the total ratio. As p-Pb collisions increase in multiplicity and become more dominated by the underlying-event production, this large discrepancy in the UE ratio between data and PYTHIA means the total ratio in

p-Pb events move farther away from the PYTHIA behavior as multiplicity increases. This highlights the ability of these separated yield ratios to more stringently test model behavior.

Chapter Seven: Summary

When ordinary nuclear matter is subjected to an environment of extremely high energy density and temperature, the nucleons "melt" into a new state of matter, known as the Quark-Gluon Plasma (QGP). The properties of this partonic medium have been studied extensively using ultra-relativistic heavy-ion collisions at particle accelerators for the past several decades. Contrary to initial predictions that it would behave like an ideal gas, the QGP is instead observed to act like a strongly interacting fluid, exhibiting strong signatures of collective behavior in the distribution of final state particles. Another observed signature of the QGP is a large enhancement in the production of strange quarks, and therefore an increase in the ratio of strange hadrons to non-strange hadrons. While initially QGP formation was expected to only occur in heavy-ion collisions, collective behavior and strangeness enhancement have both been observed in smaller systems, such as high multiplicity pp and p-Pb collisions. The microscopic origin of this onset of strangeness enhancement is still an active topic of study, and new measurements are crucial to help constrain different strangeness production mechanisms within theoretical models.

Presented in this thesis are measurements of per-trigger jet-like $h - \phi$ angular correlations in p-Pb collisions, measured at different event multiplicities and associate momentum ranges. These correlations were measured with the ALICE detector at the LHC, in p-Pb collisions with center of mass energy of $\sqrt{s_{\mathrm{NN}}} = 5.02\,\mathrm{TeV}$. Also presented is a procedure for using jet-like correlations to construct separated yield ratios by comparing the identified associate $\phi(1020)$ production to inclusive hadrons using measured dihadron correlations. This procedure allows for a separation between

the near-side jet, the away-side jet, and the non-jet underlying event. The ϕ/h production can then be compared between regimes dominated by hard scattering (jets) and those dominated by softer processes (underlying event), helping to separate out different production regimes that may contribute to strangeness enhancement.

Measuring the ϕ/h yield ratios in different areas of the correlation space showed marked differences between the production in the different event regions. For all multiplicities and momentum ranges, the production ratio is significantly higher in the underlying event (UE) than in the jets, pointing to differences in strangeness production between the two regions. This high production ratio in the UE is seen to be mostly independent of multiplicity. Moreover, with increase in event multiplicity, the total pair production is increasingly made up of the underlying event, with the jet production contributing a shrinking fraction of total production. This presents an interesting "event make-up" view of strangeness enhancement, where the increasing strangeness in p-Pb collisions as multiplicity increases can be partly viewed as shifting towards events that are more dominated by the underlying event production, and therefore towards the higher ϕ/h ratio found in the underlying event.

By separating out the yields within the near and away-side jets, this analysis identified another interesting feature of the ϕ/h ratio, where a significant increase in the away-side jet ϕ/h ratio in the lower momentum range is seen. A smaller increase is seen in the near-side yields, though the amount of this change has significant statistical errors. The increase in the away-side jet ϕ/h ratio means that at the higher-multiplicity, the ratio in the away-side is similar to the ratio in the underlying event. This shift is a surprising result, and potentially points to an enhancement due to a production process that is path-length dependent, such as a high momentum parton interacting with the partonic medium to change the final jet fragmentation.

The production ratio being consistently higher in the underlying event may point to the contribution of a QGP phase in the collisions, where strangeness enhancement would be expected. However, the fact that the UE ϕ/h ratio is relatively flat with respect to multiplicity suggests that the processes responsible for the higher ϕ/h production are present even in low multiplicity p-Pb collisions, where a significant QGP phase is generally not expected.

The ϕ/h ratios in p-Pb collisions are also compared with simulated pp results using the PYTHIA event generator. Since PYTHIA does not contain a collective phase in the collision evolution, PYTHIA results are a way to compare the expected production from perturbative QCD techniques to the experimental results. The ϕ/h ratio in jets in low multiplicity p-Pb events are seen to be in good agreement with PYTHIA predictions. This gives credence to the low multiplicity jet ratios being well described by known QCD processes. However, the ratios within the underlying event are shown to be significantly higher in p-Pb collisions than in PYTHIA, across all multiplicities and momentum ranges considered in this analysis. This confirms that the softer, non-jet production region of p-Pb collisions needs additional physics to explain the larger ϕ/h production seen there.

The ability to explain the strange, collective phenomena of smaller collision systems is an ongoing effort in the heavy-ion community. Similar methods to this analysis using jet reconstructing algorithms have looked at other strange particle ratios (Λ/K_s^0) in pp and p-Pb collisions. These studies have seen similar behavior as is presented in this analysis, where the in-jet ratios are consistent with PYTHIA, while the total integrated ratios show a large discrepancy between model and data[115], [116].

By allowing access to the away-side jet production separately from the near-side,

as well as different momentum ranges inside and outside of jets, angular correlations make for a good complementary measurement to observables from reconstructed jets. A new observation of an increase in the away-side was presented in this dissertation. This increase points to interesting and not-yet understood physics occurring in small collision systems. With the increased statistics expected to be gathered during the next decade of data taking at the LHC, there is a wealth of information that can be uncovered in the strangeness sector. Extending this measurement using high multiplicity pp collisions, and performing the same measurement technique for a wider collection of strange particles, will lead to a deeper understanding of the origin of strangeness enhancement in small systems. The continued study of the onset of collective behavior in small systems is vital to explaining the behavior of nuclear matter under extreme conditions, and in so doing is vital to understanding the fundamental physics of the universe.

Appendix A: Mixed-Event Corrected Two-Dimensional $(h - KK)$ Correlations

A.1 Multiplicity Percentile 0-20%

A.1.1 Lower Assoc. Momentum $(1.5 < p_{\mathbf{T}} < 2.5\,\mathrm{GeV/c})$

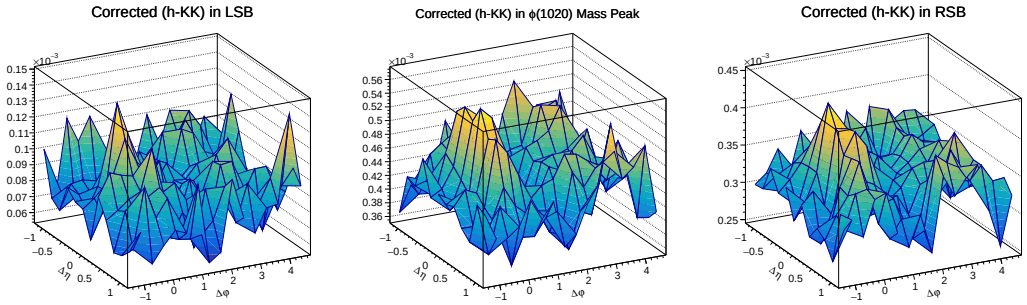

Figure A.1: Mixed-event corrected $(h - KK)$ correlations in the LSB (left), the $\phi(1020)$ mass peak (center), and the RSB (right) regions, taken in the 0-20% Multiplicity and lower associate momentum bin.

A.1.2 Higher Assoc. Momentum $(2.5 < p_{\mathbf{T}} < 4.0\,\mathrm{GeV/c})$

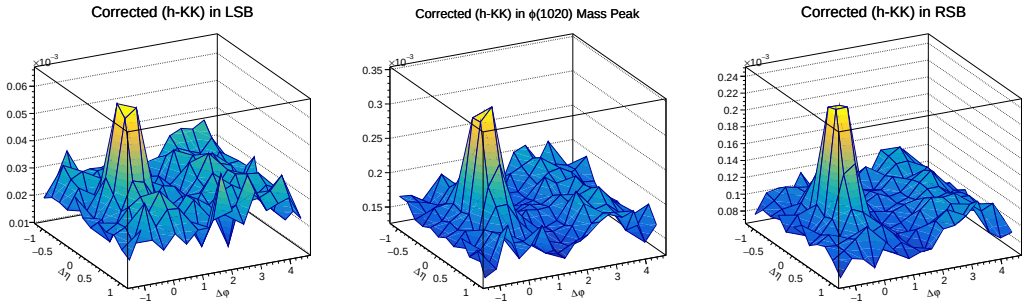

Figure A.2: Mixed-event corrected $(h - KK)$ correlations in the LSB (left), the $\phi(1020)$ mass peak (center), and the RSB (right) regions, taken in the 0-20% Multiplicity and higher associate momentum bin.

A.2 Multiplicity Percentile 20-50%

A.2.1 Lower Assoc. Momentum $(1.5 < p_{\mathbf{T}} < 2.5\,\mathrm{GeV/c})$

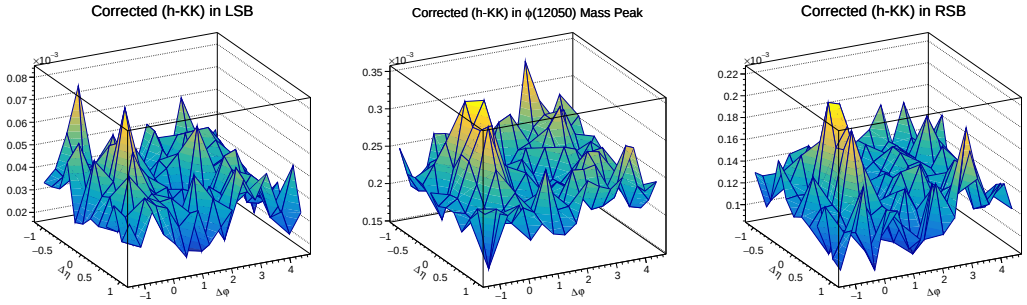

Figure A.3: Mixed-event corrected $(h - KK)$ correlations in the LSB (left), the $\phi(1020)$ mass peak (center), and the RSB (right) regions, taken in the 20-50% Multiplicity and lower associate momentum bin.

A.2.2 Higher Assoc. Momentum $(2.5 < p_{\mathbf{T}} < 4.0\,\mathrm{GeV/c})$

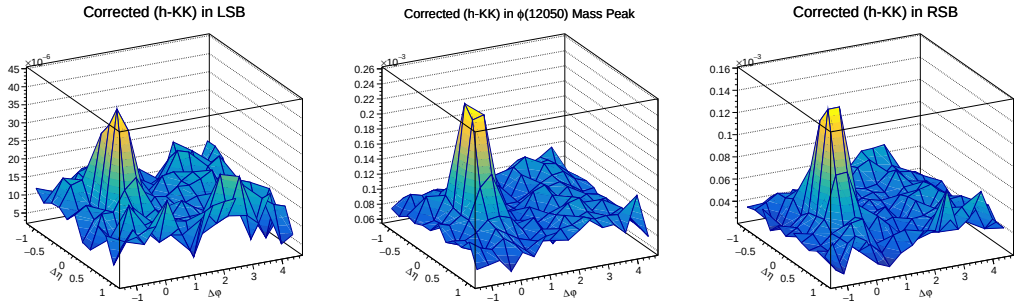

Figure A.4: Mixed-event corrected $(h - KK)$ correlations in the LSB (left), the $\phi(1020)$ mass peak (center), and the RSB (right) regions, taken in the 20-50% Multiplicity and higher associate momentum bin.

A.3 Multiplicity Percentile 50-80%

A.3.1 Lower Assoc. Momentum $(1.5 < p_{\mathbf{T}} < 2.5\,\mathrm{GeV/c})$

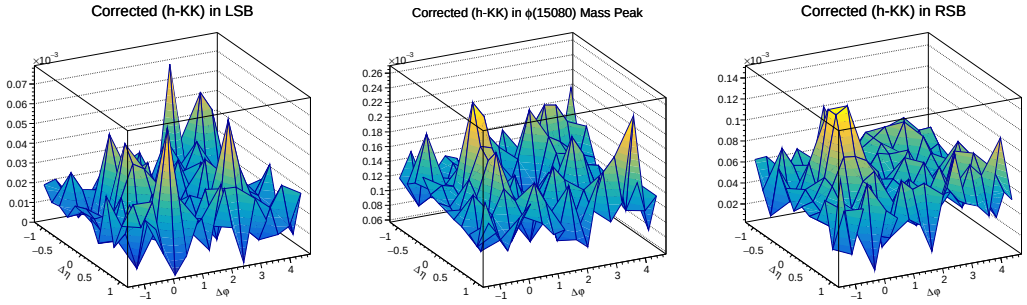

Figure A.5: Mixed-event corrected $(h - KK)$ correlations in the LSB (left), the $\phi(1020)$ mass peak (center), and the RSB (right) regions, taken in the 50-80% Multiplicity and lower associate momentum bin.

A.3.2 Higher Assoc. Momentum $(2.5 < p_{\mathbf{T}} < 4.0\,\mathrm{GeV/c})$

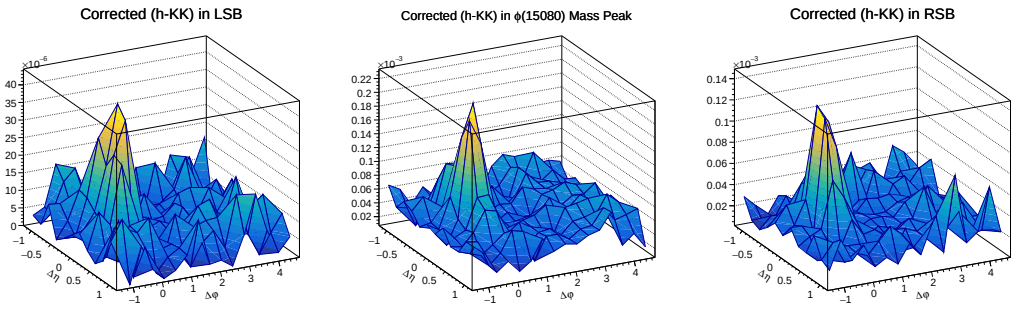

Figure A.6: Mixed-event corrected $(h - KK)$ correlations in the LSB (left), the $\phi(1020)$ mass peak (center), and the RSB (right) regions, taken in the 50-80% Multiplicity and higher associate momentum bin.

Bibliography

[1] C. M. G. LATTES, H. MUIRHEAD, G. P. S. OCCHIALINI, and C. F. POWELL, "Processes involving charged mesons," *Nature*, vol. 159, no. 4047, pp. 694–697, 1947 (cit. on p. 25).

[2] C. M. York, R. B. Leighton, and E. K. Bjørnerud, "Cloud-chamber study of charged V particles," *Phys. Rev.*, vol. 95, pp. 159–170, 1 1954. DOI: 10.1103/PhysRev.95.159. [Online]. Available: https://link.aps.org/doi/10.1103/PhysRev.95.159 (cit. on p. 26).

[3] J. A. Kadyk, G. H. Trilling, R. B. Leighton, and C. D. Anderson, "Cloud chamber investigation of anomalous θ^0 particles," *Phys. Rev.*, vol. 105, pp. 1862–1871, 6 1957. DOI: 10.1103/PhysRev.105.1862. [Online]. Available: https://link.aps.org/doi/10.1103/PhysRev.105.1862 (cit. on p. 26).

[4] A. Pais, "Some remarks on the V-particles," *Phys. Rev.*, vol. 86, pp. 663–672, 5 1952. DOI: 10.1103/PhysRev.86.663. [Online]. Available: https://link.aps.org/doi/10.1103/PhysRev.86.663 (cit. on p. 26).

[5] T. Nakano and K. Nishijima, "Charge Independence for V-particles*," *Progress of Theoretical Physics*, vol. 10, no. 5, pp. 581–582, 1953, ISSN: 0033-068X. DOI: 10.1143/PTP.10.581. eprint: https://academic.oup.com/ptp/article-pdf/10/5/581/5364926/10-5-581.pdf. [Online]. Available: https://doi.org/10.1143/PTP.10.581 (cit. on p. 26).

[6] M. Gell-Mann, "Isotopic spin and new unstable particles," *Phys. Rev.*, vol. 92, pp. 833–834, 3 1953. DOI: 10.1103/PhysRev.92.833. [Online]. Available: https://link.aps.org/doi/10.1103/PhysRev.92.833 (cit. on p. 26).

[7] M. Gell-Mann, "Symmetries of baryons and mesons," *Phys. Rev.*, vol. 125, pp. 1067–1084, 3 1962. DOI: 10.1103/PhysRev.125.1067. [Online]. Available: https://link.aps.org/doi/10.1103/PhysRev.125.1067 (cit. on p. 26).

[8] [Online]. Available: https://commons.wikimedia.org/wiki/File:Baryon_octet.png (cit. on p. 26).

[9] [Online]. Available: https://commons.wikimedia.org/wiki/File:Meson_octet.png (cit. on p. 26).

[10] G. Zweig, "An SU_3 model for strong interaction symmetry and its breaking; Version 2," 80 p, 1964, Version 1 is CERN preprint 8182/TH.401, Jan. 17, 1964. [Online]. Available: https://cds.cern.ch/record/570209 (cit. on p. 27).

[11] M. Gell-Mann, "A Schematic Model of Baryons and Mesons," *Phys. Lett.*, vol. 8, pp. 214–215, 1964. DOI: 10.1016/S0031-9163(64)92001-3 (cit. on p. 27).

[12] O. W. Greenberg, "Spin and unitary-spin independence in a paraquark model of baryons and mesons," *Phys. Rev. Lett.*, vol. 13, pp. 598–602, 20 1964. DOI: 10.1103/PhysRevLett.13.598. [Online]. Available: https://link.aps.org/doi/10.1103/PhysRevLett.13.598 (cit. on p. 27).

[13] M. Y. Han and Y. Nambu, "Three Triplet Model with Double SU(3) Symmetry," *Phys. Rev.*, vol. 139, T. Eguchi, Ed., B1006–B1010, 1965. DOI: 10.1103/PhysRev.139.B1006 (cit. on p. 27).

[14] M. Breidenbach *et al.*, "Observed behavior of highly inelastic electron-proton scattering," *Phys. Rev. Lett.*, vol. 23, pp. 935–939, 16 1969. DOI: 10.1103/PhysRevLett.23.935. [Online]. Available: https://link.aps.org/doi/10.1103/PhysRevLett.23.935 (cit. on pp. 28, 30).

[15] G. von Gehlen, "Pion production in muon-nucleon collisions," *Phys. Rev.*, vol. 118, pp. 1455–1457, 5 Jun. 1960. DOI: 10.1103/PhysRev.118.1455. [Online]. Available: https://link.aps.org/doi/10.1103/PhysRev.118.1455 (cit. on p. 28).

[16] J. D. Bjorken, "CURRENT ALGEBRA AT SMALL DISTANCES," *Conf. Proc. C*, vol. 670717, pp. 55–81, 1967 (cit. on p. 28).

[17] R. P. Feynman, *Photon-hadron interactions*. 1973 (cit. on p. 28).

[18] R. Jackiw and G. Preparata, "Probes for the constituents of the electromagnetic current and anomalous commutators," *Phys. Rev. Lett.*, vol. 22, pp. 975–977, 18 1969. DOI: 10.1103/PhysRevLett.22.975. [Online]. Available: https://link.aps.org/doi/10.1103/PhysRevLett.22.975 (cit. on p. 29).

[19] R. L. Workman *et al.*, "Review of Particle Physics," *PTEP*, vol. 2022, p. 083C01, 2022. DOI: 10.1093/ptep/ptac097 (cit. on pp. 29, 32, 80).

[20] NASA. "Dark energy, dark matter." (2022), [Online]. Available: https://science.nasa.gov/astrophysics/focus-areas/what-is-dark-energy (visited on 09/15/2022) (cit. on p. 29).

[21] A. Pich, *Quantum chromodynamics*, 1995. DOI: 10.48550/ARXIV.HEP-PH/9505231. [Online]. Available: https://arxiv.org/abs/hep-ph/9505231 (cit. on p. 30).

[22] M. H. Seymour, *Quantum chromodynamics*, 2005. DOI: 10.48550/ARXIV.HEP-PH/0505192. [Online]. Available: https://arxiv.org/abs/hep-ph/0505192 (cit. on p. 31).

[23] [Online]. Available: https://commons.wikimedia.org/wiki/File:Standard_Model_of_Elementary_Particles.svg (cit. on p. 31).

[24] K. G. Wilson, "Confinement of quarks," *Phys. Rev. D*, vol. 10, pp. 2445–2459, 8 1974. DOI: 10.1103/PhysRevD.10.2445. [Online]. Available: https://link.aps.org/doi/10.1103/PhysRevD.10.2445 (cit. on p. 33).

[25] W. Florkowski, *Phenomenology of Ultra-Relativistic Heavy-Ion Collisions*. World Scientific, 2010 (cit. on p. 33).

[26] R. Hagedorn, "Statistical thermodynamics of strong interactions at high-energies," *Nuovo Cim. Suppl.*, vol. 3, pp. 147–186, 1965 (cit. on p. 34).

[27] N. Cabibbo and G. Parisi, "Exponential hadronic spectrum and quark liberation," *Physics Letters B*, vol. 59, no. 1, pp. 67–69, 1975 (cit. on p. 34).

[28] L. Li, "Studies of dijet and trijet production in ep interactions at hera," *The European Physical Journal C - Particles and Fields*, vol. 33, no. 1, s436–s438, 2004, ISSN: 1434-6052. DOI: 10.1140/epjcd/s2004-03-1656-0. [Online]. Available: https://doi.org/10.1140/epjcd/s2004-03-1656-0 (cit. on p. 34).

[29] R. K. Ellis, W. J. Stirling, and B. R. Webber, *QCD and Collider Physics*. Cambridge University Press, 1996 (cit. on p. 35).

[30] S. Weinberg, "Non-abelian gauge theories of the strong interactions," *Phys. Rev. Lett.*, vol. 31, pp. 494–497, 7 1973. DOI: 10.1103/PhysRevLett.31.494.

[Online]. Available: https://link.aps.org/doi/10.1103/PhysRevLett.31.494 (cit. on p. 36).

[31] D. J. Gross and F. Wilczek, "Asymptotically free gauge theories. i," *Phys. Rev. D*, vol. 8, pp. 3633–3652, 10 1973. DOI: 10.1103/PhysRevD.8.3633. [Online]. Available: https://link.aps.org/doi/10.1103/PhysRevD.8.3633 (cit. on p. 36).

[32] E. Shuryak, "Quark-gluon plasma and hadronic production of leptons, photons and psions," *Physics Letters B*, vol. 78, no. 1, pp. 150–153, 1978 (cit. on p. 36).

[33] S. Weinberg, *Gravitation and Cosmology: Principles and Applications of the General Theory of Relativity*. New York: John Wiley and Sons, 1972, pp. 588–597, ISBN: 978-0-471-92567-5, 978-0-471-92567-5 (cit. on p. 36).

[34] J. C. Collins and M. J. Perry, "Superdense matter: Neutrons or asymptotically free quarks?" *Phys. Rev. Lett.*, vol. 34, pp. 1353–1356, 21 1975. DOI: 10.1103/PhysRevLett.34.1353. [Online]. Available: https://link.aps.org/doi/10.1103/PhysRevLett.34.1353 (cit. on p. 36).

[35] S. Chin, "Transition to hot quark matter in relativistic heavy-ion collision," *Physics Letters B*, vol. 78, no. 5, pp. 552–555, 1978 (cit. on p. 36).

[36] F.-M. Liu and S.-X. Liu, "Quark-gluon plasma formation time and direct photons from heavy ion collisions," *Phys. Rev. C*, vol. 89, p. 034 906, 3 2014. DOI: 10.1103/PhysRevC.89.034906. [Online]. Available: https://link.aps.org/doi/10.1103/PhysRevC.89.034906 (cit. on p. 37).

[37] D. E. Kharzeev and J. Raufeisen, "High energy nuclear interactions and qcd: An introduction," *AIP Conference Proceedings*, vol. 631, no. 1, pp. 27–69, 2002 (cit. on p. 41).

[38] R. Snellings, "Elliptic flow: A brief review," *New Journal of Physics*, vol. 13, no. 5, p. 055 008, May 2011 (cit. on p. 41).

[39] D. Kharzeev and M. Nardi, "Hadron production in nuclear collisions at rhic and high-density qcd," *Physics Letters B*, vol. 507, no. 1, pp. 121–128, 2001 (cit. on p. 41).

[40] "Centrality determination in heavy ion collisions," 2018. [Online]. Available: `https://cds.cern.ch/record/2636623` (cit. on p. 42).

[41] J. Rafelski and B. Müller, "Strangeness production in the quark-gluon plasma," *Phys. Rev. Lett.*, vol. 48, pp. 1066–1069, 16 1982. DOI: `10.1103/PhysRevLett.48.1066`. [Online]. Available: `https://link.aps.org/doi/10.1103/PhysRevLett.48.1066` (cit. on p. 43).

[42] P. Koch, B. Müller, and J. Rafelski, "Strangeness in relativistic heavy ion collisions," *Physics Reports*, vol. 142, no. 4, pp. 167–262, 1986 (cit. on p. 43).

[43] P. K. Malhotra and R. Orava, "Determination of strange quark suppression in hadronic vacuum," *Zeitschrift für Physik C Particles and Fields*, vol. 17, no. 1, pp. 85–93, 1983 (cit. on p. 44).

[44] G. Bocquet *et al.*, "A study of particle ratios and strangeness suppression in pp collisions at s=630 gev with ua1," *Physics Letters B*, vol. 366, no. 1, pp. 447–450, 1996 (cit. on p. 44).

[45] A. Wroblewski, "ON THE STRANGE QUARK SUPPRESSION FACTOR IN HIGH-ENERGY COLLISIONS," *Acta Phys. Polon. B*, vol. 16, pp. 379–392, 1985 (cit. on p. 44).

[46] C. Blume and C. Markert, "Strange hadron production in heavy ion collisions from sps to rhic," *Progress in Particle and Nuclear Physics*, vol. 66, no. 4, pp. 834–879, 2011 (cit. on p. 44).

[47] J. Sollfrank, "Chemical equilibration of strangeness," *Journal of Physics G: Nuclear and Particle Physics*, vol. 23, no. 12, p. 1903, 1997 (cit. on p. 44).

[48] F. Becattini and U. Heinz, "Thermal hadron production in pp and $p\bar{p}$ collisions," *Zeitschrift für Physik C Particles and Fields*, vol. 76, no. 2, pp. 269–286, 1997 (cit. on p. 44).

[49] A. Tounsi, A. Mischke, and K. Redlich, "Canonical aspects of strangeness enhancement," *Nuclear Physics A*, vol. 715, pp. 565c–568c, 2003 (cit. on p. 45).

[50] P. Koch, B. Müller, and J. Rafelski, "From strangeness enhancement to quark–gluon plasma discovery," *International Journal of Modern Physics A*, vol. 32, no. 31, 2017. DOI: 10.1142/s0217751x17300241. [Online]. Available: http://dx.doi.org/10.1142/S0217751X17300241 (cit. on p. 45).

[51] S. Margetis, K. Safarík, and O. Villalobos Baillie, "Strangeness production in heavy-ion collisions," *Annual Review of Nuclear and Particle Science*, vol. 50, no. 1, pp. 299–342, 2000 (cit. on p. 45).

[52] "The ALICE experiment - A journey through QCD," 2022. arXiv: 2211.04384 [nucl-ex] (cit. on pp. 46, 53).

[53] P. Braun-Munzinger, K. Redlich, and J. Stachel, "Particle production in heavy ion collisions," in *Quark–Gluon Plasma 3*, pp. 491–599. DOI: 10.1142/9789812795533_0008. eprint: https://www.worldscientific.com/doi/pdf/10.1142/9789812795533_0008. [Online]. Available: https://www.

worldscientific.com/doi/abs/10.1142/9789812795533_0008 (cit. on p. 46).

[54] J. Cleymans *et al.*, "Statistical model predictions for particle ratios at $\sqrt{s_{NN}} =$ 5.5 tev," *Phys. Rev. C*, vol. 74, p. 034 903, 3 2006. DOI: 10.1103/PhysRevC.74.034903. [Online]. Available: https://link.aps.org/doi/10.1103/PhysRevC.74.034903 (cit. on p. 46).

[55] U. A. Wiedemann, "Jet quenching in heavy ion collisions," in *Relativistic Heavy Ion Physics*, Springer Berlin Heidelberg, 2010, pp. 521–562. DOI: 10.1007/978-3-642-01539-7_17. [Online]. Available: https://doi.org/10.1007/978-3-642-01539-7_17 (cit. on p. 47).

[56] A. Collaboration. [Online]. Available: https://cds.cern.ch/images/ATLAS-PHOTO-2022-031-2 (cit. on p. 48).

[57] C. Adler *et al.*, "Disappearance of back-to-back high-p_T hadron correlations in central Au + Au collisions at $\sqrt{s_{NN}} = 200$ GeV," *Phys. Rev. Lett.*, vol. 90, p. 082 302, 8 2003. DOI: 10.1103/PhysRevLett.90.082302. [Online]. Available: https://link.aps.org/doi/10.1103/PhysRevLett.90.082302 (cit. on p. 47).

[58] U. Heinz, "The strongly coupled quark–gluon plasma created at rhic*," *Journal of Physics A: Mathematical and Theoretical*, vol. 42, no. 21, p. 214 003, May 2009 (cit. on p. 48).

[59] G. Boyd *et al.*, "Thermodynamics of su(3) lattice gauge theory," *Nuclear Physics B*, vol. 469, no. 3, pp. 419–444, 1996, ISSN: 0550-3213. DOI: https://doi.org/10.1016/0550-3213(96)00170-8. [Online]. Available: https:

//www.sciencedirect.com/science/article/pii/0550321396001708 (cit. on p. 48).

[60] V. Agotiya, L. Devi, U. Kakade, and B. K. Patra, "Strongly interacting QGP and quarkonium suppression at RHIC and LHC energies," *Int. J. Mod. Phys. A*, vol. 27, p. 1 250 009, 2012. DOI: 10.1142/S0217751X12500091 (cit. on p. 48).

[61] C. Adler *et al.*, "Elliptic flow from two and four particle correlations in Au+Au collisions at s(NN)**(1/2) = 130-GeV," *Phys. Rev. C*, vol. 66, p. 034 904, 2002. DOI: 10.1103/PhysRevC.66.034904. arXiv: nucl-ex/0206001 (cit. on p. 50).

[62] C. Shen *et al.*, "Collectivity and electromagnetic radiation in small systems," *Phys. Rev. C*, vol. 95, p. 014 906, 1 2017. DOI: 10.1103/PhysRevC.95.014906. [Online]. Available: https://link.aps.org/doi/10.1103/PhysRevC.95.014906 (cit. on p. 50).

[63] J. L. Nagle *et al.*, "Minimal conditions for collectivity in e^+e^- and $p + p$ collisions," *Phys. Rev. C*, vol. 97, p. 024 909, 2 2018. DOI: 10.1103/PhysRevC.97.024909. [Online]. Available: https://link.aps.org/doi/10.1103/PhysRevC.97.024909 (cit. on p. 51).

[64] P. Romatschke, "Do nuclear collisions create a locally equilibrated quark–gluon plasma?" *The European Physical Journal C*, vol. 77, no. 1, p. 21, 2017 (cit. on p. 51).

[65] J. Adam *et al.*, "Measurement of charged jet production cross sections and nuclear modification in p–pb collisions at snn=5.02 tev," *Physics Letters B*, vol. 749, pp. 68–81, 2015 (cit. on p. 51).

[66] R. Reed, "Jet production and structure in pp, p–pb and pb–pb collisions measured by alice," *Nuclear Physics A*, vol. 932, pp. 189–196, 2014 (cit. on p. 51).

[67] A. M. Sirunyan *et al.*, "Measurement of the inelastic proton-proton cross section at $\sqrt{s} = 13$ tev," *Journal of High Energy Physics*, vol. 2018, no. 7, p. 161, 2018, ISSN: 1029-8479. DOI: 10.1007/JHEP07(2018)161. [Online]. Available: https://doi.org/10.1007/JHEP07(2018)161 (cit. on p. 54).

[68] A. Lopes and M. L. Perrey, "FAQ-LHC The guide," 2022. [Online]. Available: https://cds.cern.ch/record/2809109 (cit. on p. 55).

[69] *Collisions*. [Online]. Available: http://lhc-machine-outreach.web.cern.ch/collisions.htm (cit. on p. 55).

[70] "Performance of the alice experiment at the cern lhc," *International Journal of Modern Physics A*, vol. 29, no. 24, 2014. DOI: DOI : 10 . 1142 / S0217751X14300440. [Online]. Available: https://www.worldscientific.com/doi/epdf/10.1142/S0217751X14300440 (cit. on pp. 55, 61).

[71] E. Botta, "ALICE ITS: Operational Experience, Performance and Lessons Learned," *PoS*, vol. Vertex2019, p. 002, 2020. DOI: 10.22323/1.373.0002 (cit. on p. 57).

[72] "The ALICE definition of primary particles," 2017, https://cds.cern.ch/record/2270008 (cit. on p. 57).

[73] J. Alme *et al.*, "The alice tpc, a large 3-dimensional tracking device with fast readout for ultra-high multiplicity events," *Nuclear Instruments and Methods in Physics Research Section A: Accelerators, Spectrometers, Detectors and Associated Equipment*, vol. 622, no. 1, pp. 316–367, 2010, ISSN: 0168-9002. DOI: https://doi.org/10.1016/j.nima.2010.04.042. [Online].

Available: https://www.sciencedirect.com/science/article/pii/S0168900210008910 (cit. on p. 58).

[74] G. Dellacasa *et al.*, "ALICE: Technical design report of the time projection chamber," 2000 (cit. on pp. 58, 59).

[75] C. Lippmann, "Performance of the alice time projection chamber," *Physics Procedia*, vol. 37, pp. 434–441, 2012, Proceedings of the 2nd International Conference on Technology and Instrumentation in Particle Physics (TIPP 2011), ISSN: 1875-3892. DOI: https://doi.org/10.1016/j.phpro.2012.02.390. [Online]. Available: https://www.sciencedirect.com/science/article/pii/S187538921201721X (cit. on p. 59).

[76] G. Dellacasa *et al.*, "ALICE technical design report of the time-of-flight system (TOF)," 2000 (cit. on p. 60).

[77] P. Cortese *et al.*, "ALICE: Addendum to the technical design report of the time of flight system (TOF)," 2002 (cit. on p. 61).

[78] T. A. collaboration, "Performance of the alice vzero system," *Journal of Instrumentation*, vol. 8, no. 10, P10016, 2013. DOI: 10.1088/1748-0221/8/10/P10016. [Online]. Available: https://dx.doi.org/10.1088/1748-0221/8/10/P10016 (cit. on p. 62).

[79] P. Cortese *et al.*, "ALICE electromagnetic calorimeter technical design report," 2008 (cit. on pp. 62, 63).

[80] J. Allen *et al.*, "ALICE DCal: An Addendum to the EMCal Technical Design Report Di-Jet and Hadron-Jet correlation measurements in ALICE," 2010 (cit. on pp. 62, 63).

[81] U. Abeysekara *et al.*, "ALICE EMCal Physics Performance Report," 2010. arXiv: 1008.0413 [physics.ins-det] (cit. on p. 63).

[82] A. G. Knospe *et al.*, "Hadronic resonance production and interaction in $p-$Pb collisions at lhc energies in epos3," *Phys. Rev. C*, vol. 104, p. 054 907, 5 2021. DOI: 10.1103/PhysRevC.104.054907. [Online]. Available: https://link.aps.org/doi/10.1103/PhysRevC.104.054907 (cit. on p. 72).

[83] A. Ilner *et al.*, "Probing hot and dense nuclear matter with $K^*, \overline{K}^*$ vector mesons," *Phys. Rev. C*, vol. 99, p. 024 914, 2 Feb. 2019. DOI: 10.1103/PhysRevC.99.024914. [Online]. Available: https://link.aps.org/doi/10.1103/PhysRevC.99.024914 (cit. on p. 72).

[84] S. Tripathy, "Hadronic resonances production with alice at the lhc," in *The XVIII International Conference on Strangeness in Quark Matter (SQM 2019)*, D. Elia, G. E. Bruno, P. Colangelo, and L. Cosmai, Eds., Cham: Springer International Publishing, 2020, pp. 329–332 (cit. on p. 72).

[85] A. K. Dash, "Multiplicity dependence of strangeness and hadronic resonance production in pp and p-pb collisions with alice at the lhc," *Nuclear Physics A*, vol. 982, pp. 467–470, 2019, The 27th International Conference on Ultra-relativistic Nucleus-Nucleus Collisions: Quark Matter 2018, ISSN: 0375-9474. DOI: https://doi.org/10.1016/j.nuclphysa.2018.11.011. [Online]. Available: https://www.sciencedirect.com/science/article/pii/S037594741830397X (cit. on p. 72).

[86] R. B. Ash, *Basic Probability Theory*. Dover Publications, 2008 (cit. on p. 74).

[87] L. Adamczyk *et al.*, "Jet-hadron correlations in $\sqrt{s_{\mathrm{NN}}} = 200$ GeV $p+p$ and central Au+Au collisions," *Phys. Rev. Lett.*, vol. 112, p. 122 301, 12 2014. DOI:

10.1103/PhysRevLett.112.122301. [Online]. Available: https://link.aps.org/doi/10.1103/PhysRevLett.112.122301 (cit. on p. 76).

[88] J. Adams *et al.*, "Hadronization geometry from net-charge angular correlations on momentum subspace (η,φ) in au–au collisions at snn=130 gev," *Physics Letters B*, vol. 634, no. 4, pp. 347–355, 2006, ISSN: 0370-2693. DOI: https://doi.org/10.1016/j.physletb.2006.01.061. [Online]. Available: https://www.sciencedirect.com/science/article/pii/S037026930600133X (cit. on p. 77).

[89] T. A. Trainor, R. J. Porter, and D. J. Prindle, "Autocorrelations from fluctuation scale dependence by inversion," *Journal of Physics G: Nuclear and Particle Physics*, vol. 31, no. 7, p. 809, 2005. DOI: 10.1088/0954-3899/31/7/023. [Online]. Available: https://dx.doi.org/10.1088/0954-3899/31/7/023 (cit. on p. 77).

[90] J. Adams *et al.*, "Minijet deformation and charge-independent angular correlations on momentum subspace (η, φ) in au-au collisions at $\sqrt{s_{NN}} = 130$ gev," *Phys. Rev. C*, vol. 73, p. 064 907, 6 2006. DOI: 10.1103/PhysRevC.73.064907. [Online]. Available: https://link.aps.org/doi/10.1103/PhysRevC.73.064907 (cit. on p. 77).

[91] S. Oh, A. Morsch, C. Loizides, and T. Schuster, "Correction methods for finite-acceptance effects in two-particle correlation analyses," *The European Physical Journal Plus*, vol. 131, no. 8, p. 278, 2016 (cit. on p. 77).

[92] A. Adare *et al.*, "Dihadron azimuthal correlations in au+au collisions at $\sqrt{s_{NN}} = 200$ gev," *Phys. Rev. C*, vol. 78, p. 014 901, 1 2008. DOI: 10.1103/

PhysRevC.78.014901. [Online]. Available: https://link.aps.org/doi/10.1103/PhysRevC.78.014901 (cit. on p. 77).

[93] S. Chatrchyan *et al.*, "Centrality dependence of dihadron correlations and azimuthal anisotropy harmonics in pbpb collisions at $\sqrt{s_{textNN}}$ = 2.76 tev," *The European Physical Journal C*, vol. 72, no. 5, p. 2012, 2012 (cit. on p. 77).

[94] ——, "Long-range and short-range dihadron angular correlations in central pbpb collisions at $\sqrt{s_{textNN}}$ = 2.76 tev," *Journal of High Energy Physics*, vol. 2011, no. 7, p. 76, 2011 (cit. on p. 77).

[95] B. Abelev *et al.*, "Long-range angular correlations on the near and away side in p–pb collisions at snn=5.02 tev," *Physics Letters B*, vol. 719, no. 1, pp. 29–41, 2013 (cit. on p. 77).

[96] S. Acharya *et al.*, "Production of $K^*(892)^0$ and $\phi(1020)$ in ppandPb−Pb collisions at $\sqrt{s_{NN}}$ = 5.02TeV," *Phys. Rev. C*, vol. 106, p. 034 907, 3 2022. DOI: 10.1103/PhysRevC.106.034907. [Online]. Available: https://link.aps.org/doi/10.1103/PhysRevC.106.034907 (cit. on p. 81).

[97] S. S. Adler *et al.*, "Dense-medium modifications to jet-induced hadron pair distributions in Au + Au collisions at $\sqrt{s_{NN}}$ = 200 GeV," *Phys. Rev. Lett.*, vol. 97, p. 052 301, 5 Aug. 2006. DOI: 10.1103/PhysRevLett.97.052301. [Online]. Available: https://link.aps.org/doi/10.1103/PhysRevLett.97.052301 (cit. on pp. 85, 112).

[98] I. Belikov, "Event reconstruction and particle identification in the alice experiment at the lhc," *EPJ Web of Conferences*, vol. 70, p. 00 029, 2014. DOI: 10.1051/epjconf/20147000029. [Online]. Available: https://doi.org/10.1051/epjconf/20147000029 (cit. on p. 88).

[99] J. Adam *et al.*, "Multiplicity and transverse momentum evolution of charge-dependent correlations in pp, p–pb, and pb–pb collisions at the lhc," *The European Physical Journal C*, vol. 76, no. 2, p. 86, 2016 (cit. on pp. 90, 131).

[100] C. Bierlich *et al.*, *A comprehensive guide to the physics and usage of pythia 8.3*, 2022. DOI: 10.48550/ARXIV.2203.11601. [Online]. Available: https://arxiv.org/abs/2203.11601 (cit. on p. 90).

[101] S. Roesler, R. Engel, and J. Ranft, "The monte carlo event generator dpmjet-iii," in *Advanced Monte Carlo for Radiation Physics, Particle Transport Simulation and Applications*, Berlin, Heidelberg: Springer Berlin Heidelberg, 2001, pp. 1033–1038, ISBN: 978-3-642-18211-2 (cit. on p. 90).

[102] R. Brun *et al.*, *GEANT 3: user's guide Geant 3.10, Geant 3.11; rev.version.* Geneva: CERN, 1987. [Online]. Available: https://cds.cern.ch/record/1119728 (cit. on p. 91).

[103] J. Adam *et al.*, "Production of k*(892)^0 and ϕ(1020) in p–pb collisions at $\sqrt{s_{\mathrm{NN}}} = 5.02\,\mathrm{TeV}$," *The European Physical Journal C*, vol. 76, no. 5, p. 245, 2016, ISSN: 1434-6052. DOI: 10.1140/epjc/s10052-016-4088-7. [Online]. Available: https://doi.org/10.1140/epjc/s10052-016-4088-7 (cit. on pp. 93, 120).

[104] S. Acharya *et al.*, "Production of charged pions, kaons, and (anti-)protons in pb-pb and inelastic *pp* collisions at $\sqrt{s_{\mathrm{NN}}} = 5.02$ tev," *Phys. Rev. C*, vol. 101, p. 044 907, 4 2020. DOI: 10.1103/PhysRevC.101.044907. [Online]. Available: https://link.aps.org/doi/10.1103/PhysRevC.101.044907 (cit. on p. 94).

[105] N. Jacazio, *Pid performance of the alice-tof detector in run 2*, 2018. DOI: 10.48550/ARXIV.1809.00574. [Online]. Available: https://arxiv.org/abs/1809.00574 (cit. on p. 98).

[106] K. Aamodt *et al.*, "Particle-yield modification in jetlike azimuthal dihadron correlations in pb-pb collisions at $\sqrt{s_{\mathrm{NN}}} = 2.76$ TeV," *Phys. Rev. Lett.*, vol. 108, p. 092 301, 9 2012. DOI: 10.1103/PhysRevLett.108.092301. [Online]. Available: https://link.aps.org/doi/10.1103/PhysRevLett.108.092301 (cit. on p. 100).

[107] *Closure testing*, 2017. [Online]. Available: https://nnpdf.mi.infn.it/research/closure-testing/ (cit. on p. 103).

[108] A. M. Poskanzer and S. A. Voloshin, "Methods for analyzing anisotropic flow in relativistic nuclear collisions," *Phys. Rev. C*, vol. 58, pp. 1671–1678, 3 1998. DOI: 10.1103/PhysRevC.58.1671. [Online]. Available: https://link.aps.org/doi/10.1103/PhysRevC.58.1671 (cit. on p. 114).

[109] J. Bielcikova *et al.*, "Elliptic flow contribution to two-particle correlations at different orientations to the reaction plane," *Phys. Rev. C*, vol. 69, p. 021 901, 2 2004. DOI: 10.1103/PhysRevC.69.021901. [Online]. Available: https://link.aps.org/doi/10.1103/PhysRevC.69.021901 (cit. on p. 114).

[110] S. Wang *et al.*, "Measurement of collective flow in heavy-ion collisions using particle-pair correlations," *Phys. Rev. C*, vol. 44, pp. 1091–1095, 3 1991. DOI: 10.1103/PhysRevC.44.1091. [Online]. Available: https://link.aps.org/doi/10.1103/PhysRevC.44.1091 (cit. on p. 114).

[111] B. Abelev *et al.*, "Long-range angular correlations of π, k and p in p–pb collisions at snn=5.02 tev," *Physics Letters B*, vol. 726, no. 1, pp. 164–177,

2013, ISSN: 0370-2693. DOI: https://doi.org/10.1016/j.physletb.2013.08.024. [Online]. Available: https://www.sciencedirect.com/science/article/pii/S0370269313006503 (cit. on pp. 115–117).

[112] K. Aamodt *et al.*, "Harmonic decomposition of two particle angular correlations in pb–pb collisions at snn=2.76 tev," *Physics Letters B*, vol. 708, no. 3, pp. 249–264, 2012 (cit. on p. 115).

[113] B. Abelev *et al.*, "Pseudorapidity density of charged particles in p+Pb collisions at $\sqrt{s_{NN}}$=5.02 TeV," *Phys. Rev. Lett.*, vol. 110, p. 032 301, 3 2013. DOI: 10.1103/PhysRevLett.110.032301. [Online]. Available: https://link.aps.org/doi/10.1103/PhysRevLett.110.032301 (cit. on p. 120).

[114] P. Skands, S. Carrazza, and J. Rojo, "Tuning pythia 8.1: The monash 2013 tune," *The European Physical Journal C*, vol. 74, no. 8, p. 3024, Aug. 2014, ISSN: 1434-6052. DOI: 10.1140/epjc/s10052-014-3024-y. [Online]. Available: https://doi.org/10.1140/epjc/s10052-014-3024-y (cit. on p. 150).

[115] V. Kučera, "Production of strange particles in charged jets in pb–pb and p–pb collisions measured with alice," *Nuclear and Particle Physics Proceedings*, vol. 276-278, pp. 181–184, 2016 (cit. on p. 157).

[116] R. Reed, "Jet production and structure in pp, p–pb and pb–pb collisions measured by alice," *Nuclear Physics A*, vol. 932, pp. 189–196, 2014 (cit. on p. 157).